STRUCTURAL RESPONSE TO INFLIGHT ACOUSTIC AND AERODYNAMIC ENVIRONMENTS

By K. L. Chandiramani, S. E. Widnall,
R. H. Lyon and P. A. Franken

N67 36060

Distribution of this report is provided in the interest of information exchange. Responsibility for the contents resides in the author or organization that prepared it.

Prepared under Contract No. NAS8-20026 by

Bolt Beranek and Newman Inc.
Cambridge, Massachusetts

for

NATIONAL AERONAUTICS AND SPACE ADMINISTRATION

TABLE OF CONTENTS

Page

LIST OF ILLUSTRATIONS.................................... vii

LIST OF SYMBOLS.. ix

PREFACE.. 1

SECTION 1 INFLIGHT ACOUSTIC AND FLUCTUATING AERODYNAMIC ENVIRONMENTS........................ 3

- 1.1 Introduction................................ 3
- 1.2 Acoustic Noise During Lift-Off.............. 3
  - 1.2.1 Introduction........................... 3
  - 1.2.2 Mechanisms of Noise Generation by Flow Fluctuations.................... 4
  - 1.2.3 Noise Sources in Turbulence......... 4
    - Turbulence in Mean Flow Fields...... 5
    - Far Field, Near Field, Geometric Field.............................. 5
  - 1.2.4 Jet Noise, Order-of-Magnitude Analysis........................... 7
    - Subsonic Jet....................... 7
    - Supersonic Jet..................... 8
  - 1.2.5 A Qualitative Description of the Exhaust Flow Noise.................. 8
  - 1.2.6 Properties of the Noise Field on a Launch Vehicle.................... 9
  - 1.2.7 Estimation of Noise Levels at the Surface of a Rocket-Powered Launch Vehicle............................ 10
    - Scaling Laws....................... 11
  - 1.2.8 An Example of Estimation of Lift-Off Noise by Dimensional Scaling........ 12
- 1.3 The Aerodynamic Noise Environment of a Typical Launch Vehicle.................... 14
  - 1.3.1 Introduction....................... 14
  - 1.3.2 The Turbulent Boundary Layer on a Rough Flat Plate and its Application to Regions of Attached Flow......... 16

TABLE OF CONTENTS (cont'd)

Page

1.3.3 Wake Impingement.................... 21

1.3.4 Subsonic Flow Separation............. 23

1.3.5 Transonic Shock Boundary-Layer Interaction.......................... 24

1.3.6 Shock Induced Separation at Interstage Flares.................... 27

1.4 Appropriate Mathematical Models for the Environments............................... 32

1.4.1 Acoustic Noise During Lift-Off....... 32

1.4.2 Fluctuating Pressure Field Associated with a Turbulent Boundary Layer under Smooth Flow Conditions............................ 32

1.4.3 Surface Pressure Fluctuations Associated with Subsonic and Supersonic Separation, Shock-Induced Separation and Wake Impingement......................... 36

1.4.4 Oscillating Shock.................. 37

SECTION 2 SOME IDEALIZED STRUCTURES.......................... 39

2.1 Introduction................................. 39

2.2 Pressure-to-Velocity Wave Admittance for Infinitely Extended Structures............. 39

2.2.1 Infinitely Long Isotropic Cylinder or Plate............................ 39

2.2.2 Infinitely Long Orthotropic Cylinder or Plate............................ 42

2.2.3 Infinitely Long Isotropic and Fluid Loaded Cylinder or Plate............. 45

2.3 Representation and Statistics of Modes and "Modal Oscillators" for Structures of Finite Extent..................................... 47

2.3.1 Modal Representation for a Cylinder and a Plate................ 47

Modal Representation for an Isotropic Cylinder.................. 47

TABLE OF CONTENTS (cont'd)

Page

Modal Representation for an Orthotropic or Fluid Loaded Cylinder.............................. 50

Modal Representation for a Flat Plate................................ 51

2.3.2 Modal Density for a Cylinder and a Plate.............................. 51

Modal Density for an Orthotropic Cylinder............................. 52

Modal Density for an Orthotropic Plate............................... 54

Modal Density for an Isotropic Cylinder............................. 54

Modal Density for a Fluid-Loaded Cylinder............................. 55

2.4 Acoustical Radiation Properties of Structural Modes...................................... 56

2.4.1 Introduction......................... 56

Definition of Radiation Resistance.... 56

Relation Between Radiation Resistance and Coupling Parameter................ 56

Classification of Modes............... 56

2.4.2 Single-Mode Radiation Resistance for a Flat Plate or a Cylinder............ 58

An Isotropic Flat Plate............... 58

An Orthotropic or Fluid-Loaded Plate.. 59

An Isotropic Cylinder................. 59

An Orthotropic or Fluid-Loaded Cylinder............................. 60

2.4.3 Average Radiation Resistance for a Flat Plate or a Cylinder.............. 60

An Isotropic Flat Plate............... 60

A Fluid-Loaded Plate.................. 62

An Orthotropic Flat Plate............. 62

An Isotropic Cylinder Above its Ring Frequency............................ 63

An Isotropic Cylinder Below its Ring Frequency............................ 64

TABLE OF CONTENTS (cont'd)

Page

A Fluid-Loaded Cylinder............... 64

An Orthotropic Cylinder Above its Ring Frequency........................ 55

Density of AF Modes Below the Ring Frequency of an Orthotropic Cylinder.. 65

Radiation Resistance of an Orthotropic Cylinder Below its Ring Frequency..... 67

Average Radiation Loss Factor......... 68

SECTION 3 STRUCTURAL VIBRATION INDUCED BY THE ACOUSTIC AND AERODYNAMIC ENVIRONMENTS........................... 69

3.1 Introduction.............................. 69

3.2 Excitation from a Turbulent Boundary Layer.. 70

3.2.1 Introduction.......................... 70

3.2.2 Response of an Isotropic Cylinder or Flat Plate of Infinite Extent to a TBL Pressure Field................... 73

3.2.3 Response of an Orthotropic Cylinder or Flat Plate of Infinite Extent to a TBL Pressure Field....................... 79

3.2.4 Response of an Isotropic, Liquid-Loaded Cylinder or Flat Plate of Infinite Extent to a TBL Pressure Field........ 80

3.2.5 Consideration of Forced Response...... 83

3.3 Excitation From a Diffuse Sound Field........ 84

3.3.1 Introduction.......................... 84

3.3.2 Structural Response to a Diffuse Sound Field.......................... 85

3.4 Excitation by an Oscillating Shock Front..... 90

3.4.1 Introduction.......................... 90

3.4.2 Response of a Cylinder to an Oscillating Shock Front............... 90

3.4.3 Response of a Rectangular Plate to an Oscillating Shock Front............... 94

3.4.4 Influence of Clamped Edges,and of Additional Membrane and Buckling Stresses on Structural Response to an Oscillating Shock Front.......................... 95

NOTES AND REFERENCES.................................... 97

FIGURES

LIST OF ILLUSTRATIONS

Figure	Title
1	Estimate of Lift-Off Noise Levels on Vehicle B, Based on Scaling of Data on Vehicle A.
2	Summary of Aerodynamic Noise Sources as a Function of Vehicle Geometry and Mach Number.
3	Turbulent Boundary Layer Development on a Flat Plate.
4	Nondimensional Spectrum of Boundary Layer Pressure Fluctuations in Third-Octave Bands.
5	Gross Features of the Flow Around a Launch Vehicle During Subsonic and Supersonic Flights .
6	Boundary of $C_{p_{rms}}$ for Wake Impingement.
7	Nondimensional Third-Octave Band Spectra for Wake Impingement and Transonic Shock-Boundary Interaction.
8	Normalized Downstream Decay of $C_{p_{rms}}$ for Subsonic Separation.
9	Magnitude of $\overline{C}_{p_{rms}}$ as a Function of Turning Angle in Subsonic Flow.
10	Sketch of Transonic Shock-Boundary Layer Interaction and Resulting Pressure Time Patterns.
11	Maximum $C_{p_{rms}}$ in Transonic Flow as a Function of θ and x/D.
12	Mach Number for Maximum $C_{p_{rms}}$ as a Function of θ and x/D.
13	Effect of Reynolds Number on the Pressure Rise for Separation at Interstage Flares.
14	Effect of Mach Number on the Pressure Rise for Separation at Interstage Flares.
15	Summary of Kistler's Experiment.
16	Sketch of $\overline{p}(x)$ and $p_{rms}(x)$ due to Shock Oscillation.
17	Loci of Constant Resonance Frequency in the Dimensionless Wavenumber Plane (r,θ), Isotropic Cylinder.

LIST OF ILLUSTRATIONS (cont'd)

Figure	Title
18	Sketch of a Corrugated Structure.
19	Loci of Constant Resonance Frequency in the Dimensionless Wavenumber Plane (r,θ), Liquid-Loaded Isotropic Cylinder, $\beta = 7.54$.
20	Idealization of Resonance Locus for an Orthotropic Cylinder Below Ring Frequency.
21	Classification of Structural Modes in k-space at Frequency ω.
22	Acoustic Wavenumber Locus (AL) and Resonance Locus (RL) for an Orthotropic Plate, $k_1 > k_3$.
23(a)	Acoustic Wavenumber Locus (AL) and Resonance Locus (RL For an Orthotropic Cylinder Below Ring Frequency, $\alpha_3 > \alpha_1$.
23(b)	Exact and Approximate Boundaries of the Region of the AF Modes for an Orthotropic Cylinder.
24	The Range of Excitation and the Classification of Modes in the Wavenumber Plane. Isotropic Cylinder.
25	Loci of Resonance and Hydrodynamic Coincidence in $\underline{k}$ Plane.
26	Loci of Resonance and Hydrodynamic Coincidence in k Plane Below Ring Frequency.
27	Schematic Representation of a Cylinder, and Variation of Pressure Field Associated with an Oscillating Shock.
28	Dimensionless Spectra for the Exciting Modal Forces. Excitation from an Oscillating Shock.

LIST OF SYMBOLS

a	radius of cylindrical shell
AF	acoustically fast
AL	acceleration level
AS	acoustically slow
$A(\omega)$	acceleration spectrum
c	sound speed
c_3^2	$c_\ell^2\alpha_3$
c_f	local skin-friction coefficient
c_ℓ	velocity of longitudinal waves in cylinder material
c_{mn}	normalizing constants
$c_{p_{rms}}$	root-mean-square pressure coefficient
C_D	drag coefficient
C_p	pressure coefficient
d	nozzle diameter
d_{eff}	effective nozzle diameter
E	Young's modulus
f	frequency
f_h	hydrodynamic critical frequency
$F_{mn}(t)$	modal force exciting mode (m,n)
h	inertial thickness of cylindrical shell
h_1	extensional thickness of cylindrical shell in axial direction
h_3	extensional thickness of cylindrical shell in circumferential direction
H	form parameter δ^*/θ
$H(\underline{k},\omega)$	pressure-to-velocity wave admittance
$H_{mn}(\omega)$	modal admittance

LIST OF SYMBOLS (cont'd)

HC	hydrocynamically critical
HF	hydrodynamically fast
HS	hydrodynamically slow
k	magnitude $\lvert \underline{k} \rvert$ of wavenumber vector
$\underline{k}$	wavenumber vector (k_1, k_3)
k_a	acoustic wavenumber
k_c, k_p	magnitude of HC resonant wavenumber
k_s	equivalent roughness height
ℓ_1	length of cylindrical shell
ℓ_3	circumference of cylinder
ℓ_1, ℓ_3	edge lengths of plate
m, n	positive integers
M	mach number (also structural mass)
$n(\omega)$	average value of modal density over a frequency band
$N(\omega)$	approximate number of modes with natural frequencies less than ω
p	pressure
p_o	pressure before shock
p_1	pressure after shock
p_h^2	over-all value of mean squared pressure fluctuations in TBL
p_p	plateau pressure
p_{rms}	root-mean-square pressure
$p(\underline{x}, t)$	fluctuating pressure field on surface of structure
Δ_p	jump in static pressure across shock front
PWL	power input level
q	dynamic pressure

LIST OF SYMBOLS (cont'd)

r	magnitude of dimensionless wavenumber
(r_b, θ_b)	dimensionless wavenumber for vibration controlled by bending stresses
(r_m, θ_m)	dimensionless wavenumber for vibration controlled by membrane stresses
R	Reynolds number
R_{rad}	radiation resistance
R_x	Reynolds number based on distance from leading edge
R_{δ_o}	Reynolds number based on δ_o
S	Strouhal number
S_ϵ	Strouhal numbers based on wake momentum thickness
$S(\omega)$	stress-level spectrum
SL	stress level
SPL	sound-pressure level
t	time (also thickness)
TBL	turbulent boundary layer
U	flight speed of vehicle or free-stream velocity
U_c	convection velocity in direction x_1 of flow
U_∞	free-stream velocity
$v(\underline{x}, t)$	velocity of cylinder surface in outward radial direction
$v_{mn}(t)$	modal velocity
$V(\omega)$	velocity spectrum
VL	velocity level
x	distance from leading edge
x_1	direction of the flow (also axial direction on cylindrical shell)
x_3	direction transverse to the flow (also circumferential direction on cylindrical shell)

LIST OF SYMBOLS (cont'd)

$y(t)$	displacement of shock front from its mean position
α_1	h_1/h
α_3	h_3/h
β	dimensionless fluid-loading parameter
δ	boundary-layer thickness
δ^*	boundary-layer displacement thickness
η	dissipation constant
η_s	total cylinder loss factor
θ	boundary-layer momentum thickness
θ_c, θ_p	direction of HC resonant wavenumber
κ	bending thickness or geometric mean radius of gyration
κ_1	radius of gyration for axial direction
κ_3	radius of gyration for circumferential direction
λ_c	acoustic wavelength at critical frequency
$\mu(\omega)$	η_{rad}/η_s averaged over resonant modes
ν	kinematic viscosity (also dimensionless frequency)
ν_3	dimensionless frequency for orthotropic structure
$\Pi(\omega)$	frequency spectrum of power input per unit area
$\Pi_b(\omega)$	power input spectrum for vibration controlled by bending stresses
$\Pi_m(\omega)$	power input spectrum for vibration controlled by membrane stresses
ρ_o	density of liquid
ρ_m	material density
ρ_s	surface mass density

LIST OF SYMBOLS (cont'd)

σ	root-mean-square displacement of shock front
σ_{rad}	modal radiation efficiency
τ_w	viscous shear at the wall
$\Phi_1(k_1),\Phi_3(k_3)$	components of wavenumber spectrum $\Phi_{13}(\underline{k})$
$\Phi_{13}(\underline{k})$	normalized wavenumber spectrum for TBL pressure fluctuations
$\Phi_f(\omega)$	normalized fixed-microphone spectrum for TBL pressure fluctuations
$\Phi_m(\omega)$	temporal spectrum for TBL pressure fluctuations
$\Phi_p(\underline{k},\omega)$	combined wavenumber and frequency spectrum for TBL pressure fluctuations
$\Phi_p(\omega)$	power density spectrum for free-field acoustic pressure
$\psi_{mn}(\underline{x})$	orthogonal mode shape for mode (m,n)
ω	frequency of vibration
ω_c	acoustic critical frequency
ω_h	hydrodynamic critical frequency
ω_{mn}	natural frequency of mode (m,n)
ω_r	ring frequency
ω_{osc}	shock-oscillation frequency

STRUCTURAL RESPONSE TO INFLIGHT ACOUSTIC AND AERODYNAMIC ENVIRONMENTS

By K. L. Chandiramani, S. E. Widnall, R. H. Lyon,
and P. A. Franken

PREFACE

This report presents procedures for estimating some important classes of inflight acoustic and fluctuating aerodynamic environments and resulting surface vibration levels at high frequencies experienced by major skin segments of a typical launch vehicle. This task is divided into three broad steps:

1) study of the environments
2) study of structural components
3) study of the interaction between the two.

Step 1: Inflight environments are classified and studied in Section 1. Procedures are presented for adequate representation and estimation of those aspects of the environments which enter directly into the interactions with the structural components. The approach here is partly theoretical, partly empirical. Extensive use is made of recent laboratory and inflight data. The types of environment treated are: acoustic noise from engines during lift-off; surface pressure fluctuations under turbulent boundary layers during subsonic, transonic, and supersonic flight regimes; smooth flow versus separated flow; shock-induced separation; wake impingement, and oscillating shocks.

Step 2: In Section 2, various dynamical properties of two idealized structures, a cylinder and a flat plate, are presented. In order to handle most situations of interest, the presentation is made general enough to apply to an orthotropic and fluid-loaded structure. The dynamical properties discussed are: pressure-to-velocity wave admittance, modes and representation of "modal oscillators," resonance frequencies of modes, modal density, radiation resistance of modes and resulting radiation loss factor.

Step 3: Interactions between the fluctuating environments and structures are studied in Section 3. The approach is statistical. The final goal of each calculation is an estimate of average (mean-squared) values of surface acceleration and stress level in frequency bands. This response estimate, in most cases, pertains to high-frequency (multimodal)resonant and "coincident" vibration. However, in one case (oscillating shock) it has been necessary to pay individual attention to the first few modes, which contribute most of the response.

The work presented in this report was developed with the following two objectives in mind:

1) The final estimates developed should be in more or less closed form, so that the effect of various input parameters can be easily appraised, and so that detailed calculations (such as numerical integration or numerical solution of a differential equation) are not necessary for the final predictions.

2) The input parameters themselves should be as few as possible and easily related to trajectory and geometric parameters.

Some examples of the choices dictated by the above criteria are: selection of a fairly simple (but still realistic) correlation model for the pressure fluctuations under a turbulent boundary layer, use of thin shell theory, and ignoring of flutter-type interaction between the vibrating structure and the turbulent boundary layer. The present results, therefore, should be looked upon as a basic system of simple solutions, which are comprehensive enough to set some preliminary design specifications and are intelligible enough so that an intuitive understanding of the results can be gained.

SECTION 1

INFLIGHT ACOUSTIC AND FLUCTUATING AERODYNAMIC ENVIRONMENTS

1.1 Introduction

In this section we classify and review some important acoustic and aerodynamic noise environments experienced by a typical launch vehicle. Our aim is to study those aspects of the environments which enter directly into interactions with the structural components of the vehicle. Some of these centrally important aspects are: the range of trajectory and geometric parameters over which a particular type of environment is manifest, the over-all mean-squared value of the associated pressure fluctuations experienced by different sections of the vehicle surface, and the frequency distribution of this over-all level. To estimate such parameters, we have made extensive use of recent laboratory and flight data.

The noise environments can be broadly classified as the acoustic noise (associated with rocket jet exhaust stream), which dominates during or shortly after vehicle lift-off, and the aerodynamic noise which dominates during the rest of the trajectory. Sections 1.2 and 1.3 describe these noise sources. In Section 1.4 mathematical models for appropriate representation of these noise sources are described. These models will be used later for response analyses.

1.2 Acoustic Noise During Lift-Off

1.2.1 Introduction . - The time history of noise measurement on a rocket-propelled launch vehicle generally shows a maximum value during or shortly after vehicle lift-off. The source of this noise is the rocket jet exhaust stream.

It has not been possible to predict this noise level by analyzing the fluid dynamics and the thermodynamics of the exhaust stream flow. Therefore, in this section, we shall give a very brief and qualitative description of the exhaust flow characteristics and the mechanisms by which flow fluctuations generate noise. For the purpose of estimating the noise levels during lift-off, we shall describe some well-established scaling laws.

1.2.2 Mechanisms of Noise Generation by Flow Fluctuations. - Suppose that a volume element in a fluid medium suffers alternate expansion and compression. If the frequency of this volume change is high enough, compression and expansion waves will be induced in the surrounding fluid medium, these waves will travel away from the source, and thus sound will be radiated. Such a volume change can be caused by local addition and subtraction of mass or heat in the fluid. Such a source of sound is called a monopole.

A dipole source is formed by two monopole sources which lie side by side, and are of opposite phase. The primary motion transmitted to the surrounding fluid medium by a dipole source is translation or acceleration. This type of source can be generated by a net force oscillating across a small closed surface in the fluid medium. A dipole is a much less efficient radiator of sound than a monopole. The sound field generated by a dipole at large distances results from the residual compression and expansion of the fluid surrounding the dipole.

A quadrupole source, in turn, is formed by two dipole sources which lie side by side and which are completely out of phase. The primary motion transmitted to the fluid is distortion. A quadrupole is generated by net stress fluctuations. The residual compression and expansion of the fluid medium is even smaller than in the case of a dipole. Thus a quadrupole is a less efficient generator of sound than a dipole or a monopole.

1.2.3 Noise Sources in Turbulence. - Lighthill [1, 2] was the first to show that turbulence behaves as a distribution of quadrupole sources of sound. From the basic equations describing the fluid dynamics and the thermodynamics of the turbulent flow, he showed that the total stress tensor T_{ij} 1/ for the flow gives rise to quadrupole sources of sound.

Turbulence in Mean Flow Fields. - In many cases of practical interest, turbulence is generated within the average flow field. Very often, the mean flow field has a sharp velocity gradient, as in the case of boundary layer flow or jet flow. The mean flow gradient tends to enhance the quadrupole radiation and to bias the quadrupole source term, and the resulting radiation is highly directional 2/.

If a rigid body (or wall) is present in the turbulent flow, the local pressure fluctuations on the solid surface can constitute dipole sources of sound 3/. Dipole sources are also obtained by reflection and diffraction of sound generated by quadrupole sources far away from the rigid surface.

Far Field, Near Field, Geometric Field. - For turbulence in a mean flow field, if ℓ is a typical length scale (say, the dimension indicating the extent of the shear layer) and V_o is a typical velocity (free-stream velocity), then, aside from numerical factors, the mean-squared pressures for monopole, dipole and quadrupole sources are given by:

$$\overline{p^2}/q^2 \sim (\ell/r)^2, \quad \text{Monopole} \tag{1}$$

$$\overline{p^2}/q^2 \sim (\ell/r)^4 + (\ell/r)^2 M_o^2, \quad \text{Dipole} \tag{2}$$

$$\overline{p^2}/q^2 \sim (\ell/r)^6 + (\ell/r)^4 M_o^2 + (\ell/r)^2 M_o^4, \quad \text{Quadrupole} \tag{3}$$

where

$q = \rho V_o^2/2$ is the dynamic pressure
ρ is the fluid density
r is the distance from source to observation point
M_o is the Mach number corresponding to V_o, $M_o = V_o/c$
and c is the sound speed.

Therefore, for all these sources, at large distance r, the mean-squared pressure varies as $1/r^2$. This is the "far field" or the "radiation field"; the pressure propagates as sound, and the compressibility effects in the fluid medium become important. Closer to the source, mean-squared pressure decreases more sharply with increase in distance (as $1/r^4$ or $1/r^6$). This, then, is the "near field" or "induction field." In this range, compressibility effects lose significance.

In case of noise from a jet, at large distances from the jet all the noise sources in the jet stream appear to be concentrated within a narrow solid angle. The cumulative effect of these sources becomes that of a point source, and the mean-squared pressure varies as $1/r^2$. At smaller distances, however, even though the contribution to the mean-squared pressure from each individual source varies inversely as the square of the distance from the source, the total pressure does not follow the same law. This is because the spatial distribution of the sources in the jet stream becomes significant in this range. The noise field in this range is called the "geometric field." In classical optics, this region is known as the Fresnel zone.

The noise field on a typical launch vehicle during lift-off is a "geometric field" induced by sources in the rocket jet exhaust stream. During flight, the noise field on the vehicle due to turbulent boundary layer or other flow conditions, is a "near field." Before we can estimate vibration response of vehicle components, we must estimate, as far as possible, statistical properties of these noise (that is, pressure) fields on the vehicle surface under different environmental conditions.

1.2.4 Jet Noise, Order-of-Magnitude Analysis

Subsonic Jet. - Consider a jet with pressure ratio less than the critical. The exhaust velocity V_o is then subsonic. We shall postpone the description of the actual flow characteristics. Here we simply comment on some important dimensional relations.

The mean-squared pressure in the far radiation field of the jet, due to the quadrupole sources in the jet stream, is given by relation (3).

$$\overline{p^2} \sim q^2(A/r^2)\ M_o{}^4, \tag{4}$$

where A, the jet exit area, is taken to be proportional to ℓ^2. Since the total acoustic power radiated Π_{rad} is proportional to $\overline{p^2}\ r^2/\rho c$, and since the mechanical power Π_{mech} is $\rho A\ V_o{}^3/2$, we have

$$\Pi_{rad}/\Pi_{mech} \sim M_o{}^5 \tag{5}$$

This result leads to the famous 8th-power law dependence, which we may now write as

$$\Pi_{rad} \approx 6 \times 10^{-5}(\rho A/2)(V_o{}^8/c^5), \tag{6}$$

the numerical constant being determined by measurement.

For the jet impinging on a rigid surface, dipole sources dominate. For that case, we can show similarly that the radiated power varies as the sixth power of the impingement velocity.

Supersonic Jet. - Relations (5) and (6) are valid only for pressure ratios less than the critical. For higher pressure ratios, the jet is supersonic relative to the sound velocity in the gas efflux. Use of relation (5) in these cases would give erroneous results, since it predicts that all the power in the jet goes into sound. It turns out that, for high-pressure-ratio jets, the radiated power becomes a constant fraction, roughly 0.25%, of the mechanical power. Consequently, the M_o^5 dependence in relation (5) disappears, and Π_{rad} turns out to be

$$\Pi_{rad} \approx 0.0025 \, (\rho A/2) \, V_o^3 \tag{7}$$

1.2.5 A Qualitative Description of the Exhaust Flow Stream [4/]

- Present-day rocket engines for launch vehicles are usually designed with pressure ratios higher than the critical value. Consequently, the jet exhaust stream is supersonic relative to the sound velocity in the gas efflux. The associated Mach number lies in the range of 5 to 8. The detailed picture of the flow conditions in the exhaust stream is very complicated indeed. In the region of the exhaust stream close to the rocket exhaust nozzle, the flow is supersonic, characterized by extreme velocity gradients and slowly expanding turbulent shear layer. Also, there are temperature inhomogeneities due to rough burning and mixing, and a complicated pattern of shock waves. The supersonic flow is rapidly decelerated, so that, 10 to 30 nozzle diameters downstream, the flow becomes subsonic. This subsonic flow is characterized by moderate velocity gradients and intense turbulence [4].

One source of noise from this complex flow field is the highly directional, intense, Mach wave emission generated by supersonically convected turbulent eddies. However, for a vehicle standing on a launch pad with its engine firing, a second major source of the noise field on the vehicle surface is likely to be the sound generated by highly turbulent (and usually subsonic) flow impinging on the launch pad. Such sound, being dipole-induced, probably competes effectively with the quadrupole sound. It has a directional maximum normal to the surface on which the flow is impinging, but will rapidly disappear as the vehicle leaves the launch pad. As discussed before, the power (and the mean-squared pressure) radiated would be proportional to the sixth power of the impingement velocity. Since the turbulent scales range from the very large values associated with the low-speed part of the flow moving away from the impingement area, to the small values characteristic of the supersonic shear-layer thickness, the associated acoustic spectrum must exhibit a wide frequency range [4].

1.2.6 Properties of the Noise Field on a Launch Vehicle. - Measurement of correlation functions for the noise field on the surface of a vehicle during launch or static firing show that, for a narrow-frequency bandwidth around frequency ω, the correlation in the axial (or vertical) direction is approximately sinusoidal, with a wavelength corresponding to the acoustic wavelength $\lambda_a = 2\pi c/\omega = 2\pi/k_a$ [5]. This, then, is the empirical evidence that the noise field is indeed a sound field which tends to propagate along the length of the vehicle. Similar correlation measurements along the circumference of the vehicle indicate that the spatial extent of the correlation in the circumferential direction is somewhat larger than that in the axial direction [5], a fact which further indicates the directionality of the acoustic noise field. This effect is more pronounced at lower frequencies, a fact which can be interpreted to mean that the lower-frequency sources, being associated with relatively larger mixing or shear lengths, are farther downstream than the high-frequency sources. As a result, low-frequency sound appears to emanate from well-correlated "point" sources.

As we shall restate in section 1.4, for estimation of structural response, we shall idealize this sound field to be diffuse, with identical correlation in all directions on the vehicle surface. Since our chief concern is with high-frequency vibration induced on the vehicle surface, this approximation is not too unreasonable. Also, at high frequencies, the wavelengths associated with the acoustic noise field are generally smaller than the circumference of the vehicle. We shall therefore assume that, as far as the reflection and diffraction of the noise field from the vehicle surface is concerned, the noise field does not sense the curvature of the vehicle surface. In other words, the vehicle presents essentially a large flat surface to the noise field.

1.2.7 Estimation of Noise Levels at the Surface of a Rocket-Powered Launch Vehicle.

- As we mentioned before, estimation of noise levels from the detailed analysis of the physics of the flow field is an almost impossible task. We must, therefore, obtain our estimates by extrapolating existing data with the aid of well-established similarity arguments, or scaling laws [6, 7].

Although present-day liquid-fuel engines vary markedly from solid-fuel engines in their design and operation, both types of engines produce exhaust streams of high-velocity hot gases. A typical exhaust velocity is of the order of 7500 ft/sec for both kinds of engines. Because the sound pressures are associated with the exhaust flow, we expect that the noise field of the two types of engines will not be markedly different, if similar firing configurations are involved. For example, a common arrangement, utilized in many static firing tests and surface launches of large rocket-powered vehicles, involves an exhaust deflector turning the stream into one or more horizontal paths.

Since the lift-off noise levels for different vehicles do not differ greatly, we can estimate, with a certain degree of confidence, noise levels for a new vehicle from the measured data on an existing vehicle. In choosing a system from which to scale measured data, we must generally seek to satisfy two requirements. First, the existing system should provide sufficient measurements to describe the new situation of interest. Second, the scaling factors should be as small as possible. That is, we must choose a system which comes as close as possible to the dimensions of the new system of interest.

Scaling Laws. - For dynamically similar systems it may be shown[7,8] that the sound pressure spectra measured at similar positions are the same when given in constant-percentage frequency bands and when frequency is scaled in inverse proportion to a characteristic length. This result has been verified in experiments [9] and gives rise to the use of a nondimensional frequency parameter. This parameter is the so-called Strouhal number, defined by frequency multiplied by a characteristic dimension of the system (such as engine nozzle diameter) and divided by a characteristic velocity (such as expanded exhaust velocity). Under the assumption that the characteristic velocity of all rocket systems considered is approximately constant, the frequency parameter may be reduced to "frequency times nozzle diameter."

The inclusion of multiple-nozzle systems requires the definition of an effective nozzle diameter d_{eff} to be used in obtaining the frequency parameter. For a system consisting of n equal nozzles spaced one nozzle diameter d or less apart, the effective nozzle diameter d_{eff} is found from experiments to be

$$d_{eff} = d(n)^{1/2} \tag{8}$$

This relation reflects the fact that jet streams from closely spaced nozzles coalesce rapidly. Limited data indicate that d_{eff} is the same as d if the nozzle separation distance greatly exceeds d.

In scaling acoustic data from one system to another, we must also adjust for changes in thrust levels between the two systems. This correction factor, however, in most cases will be less than the ratio between the thrusts. This is because, if the vehicle trajectory is to remain more or less the same, a larger thrust generally corresponds to a heavier and larger vehicle. Furthermore, the exhaust velocities do not vary a great deal, and even though noise level increases with thrust, the observation point at a "similar" station on a larger vehicle would be farther away from the noise source.

1.2.8 An Example of Estimation of Lift-Off Noise by Dimensional Scaling. - Fig. 1 shows the noise level spectrum SPL_A in third-octave bands of frequency, as measured at location x_A on vehicle A. The location x_A is halfway between the base and the nose of the vehicle. The length of the vehicle A is L_A, the overall diameter is D_A, and the total thrust is T_A. During launch, the vehicle is powered by a single, liquid-fuel rocket engine with a nozzle diameter of d_A.

We wish to estimate the lift-off noise level spectrum SPL_B at location x_B , halfway between the nose and the base of a vehicle B. The length L_B, the over-all diameter D_B and the total thrust T_B for vehicle B are

$$L_B = 2L_A$$

$$D_B = 2D_A$$

$$T_B = 4T_A$$

The total thrust T_B is provided by four closely clustered liquid-fuel engines, each with a nozzle diameter $d_B = d_A$. The exhaust-deflector systems for vehicles A and B are similar.

We assume the same velocity in the exhaust streams of the two vehicles. In that case the noise level spectrum SPL_B at frequency f_B is approximately equal to the noise level spectrum SPL_A at frequency f_A, where the frequencies f_B and f_A are related as

$$f_B \, d_{eff_B} = f_A \, d_{eff_A} \ ,$$

d_{eff_B} and d_{eff_A} being the effective nozzle diameters for the two vehicles. Consequently, we have

$$f_B = f_A d_A/(d_A 4^{1/2}) = f_A/2 \ .$$

Thus the noise level spectrum for vehicle B is obtained by shifting the spectrum SPL_A one octave to the left on the frequency scale. The spectrum SPL_B thus obtained is shown in Fig. 1.

For the present example, note that the vehicle thrust is proportional to the total nozzle area, and the overall vehicle dimensions are proportional to the effective nozzle diameter. In other words,

$$T_B/T_A = 4d_B^2/d_A^2$$

$$L_B/L_A = D_B/D_A = d_{eff_B}/d_{eff_A}$$

Thus, aside from the fact that vehicle B is expected to take off more slowly than vehicle A, the dynamic and geometric similarity between the two vehicles during launch is quite complete. Therefore it is not necessary to modify the estimated spectrum SPL_B for changes in thrust.

1.3 The Aerodynamic Noise Environment of a Typical Launch Vehicle

1.3.1 Introduction. - The aerodynamic noise input to a launch vehicle is caused by the unsteady pressure fluctuations in the turbulent boundary layer which envelopes the vehicle throughout its flight in the atmosphere.

Measurements 10, 25/ of the rms pressure fluctuations on a smooth flat plate in incompressible flow show a generally accepted level $p_{rms} = 0.006q$, where q is free-stream dynamic pressure. When referred to the wall shear stress, $p_{rms} \approx 2.7\tau_w$, where τ_w is the viscous shear at the wall. The second relation more adequately reflects the physical mechanism which generates the fluctuations in the turbulent boundary layer. Similar measurements on flat plates in compressible flow have been done by Kistler 10/ and Speaker and Ailman 25/. The two experiments show opposite trends for the behavior of p_{rms}/τ_w with Mach number.

The results of Ref. 10 indicate that p_{rms}/τ_w increases slowly, reaching a value of about 4.5 at a Mach number of 2. The results of Ref. 25 suggest that p_{rms}/τ_w decreases with Mach number, reaching a value of 1.5 at a Mach number of 2. This discrepancy has not been resolved.

A launch vehicle differs from an ideal flat plate in two important respects. First, it is not smooth. The exterior skin is covered with structural discontinuities, stringers, brackets, and protuberances of all sorts. If we are justified in assigning an average roughness height to these elements, we may treat the boundary layer as a turbulent boundary layer over a rough flat plate [11].

The second difference is that a launch vehicle is not flat. There are strong pressure gradients over the vehicle at various corners and flares. The most intense noise comes not simply from the turbulent boundary layer but rather from its interaction with severe adverse pressure gradients causing regions of separated flow. If these pressure gradients are due to compressive shock waves, the resulting unsteady shock boundary layer interaction can cause a particularly intense pressure fluctuation.

An additional source of turbulence-induced pressure fluctuations for a manned launch vehicle is the impingement of the turbulent wake of the escape tower upon the payload capsule.

Figure 2 is a brief summary of the important noise sources on a typical launch vehicle as a function of flight Mach number. Most of the pressure fluctuations due to these phenomena have a root-mean-square level proportional to the dynamic pressure q. An estimate of the root-mean-square pressure coefficient, $C_{p_{rms}} = p_{rms}/q$, to be expected for each type of flow is also indicated in the sketch.

For reference, Fig. 2 also shows q versus Mach number M, for a typical flight trajectory. To aid in converting to noise level, the dynamic pressure is plotted in decibels relative to 0.0002 μbar. Since q is about 180 to 185 dB throughout the range of interest, a region of flow separation which has $p_{rms} = 0.1q$ will have an aerodynamic noise level of 160 to 165 dB.

We now discuss some of these problems in more detail. An analytic prediction of the level, spectra, and space-time correlation for separated flows, shock boundary-layer interaction, and turbulent boundary layers over rough surfaces is of course impossible. The best that we can do is to correlate flight and wind-tunnel test data and to apply suitable scaling and semiempirical theories in an attempt to predict these phenomena for new configurations.

We shall consider the following problems:

- 1.3.2 The Turbulent Boundary Layer on a Rough Flat Plate and its Application to Regions of Attached Flow
- 1.3.3 Wake Impingement
- 1.3.4 Subsonic Flow Separation
- 1.3.5 Transonic Shock Boundary-Layer Interaction
- 1.3.6 Shock-Induced Separation at Interstage Flares

1.3.2 The Turbulent Boundary Layer on a Rough Flat Plate and its Application to Regions of Attached Flow. - There exist regions on launch vehicles for which the dominant aerodynamic noise source will be an attached turbulent boundary layer in a uniform static pressure field. For example, long cylindrical stages should be essentially free of strong pressure gradients from about one body diameter downstream of the interstage flare. We model the turbulent boundary layer in these regions as a turbulent boundary layer on a flat plate.

Experiments [10] on smooth flat plates show that p_{rms}/τ_w is a slowly varying function of Mach number M, varying from $\sim 2.$[illegible] at $M = 0$ to ~ 5 at $M = 5$. For a smooth flat plate with a fully developed turbulent boundary layer from the leading edge, the local skin-friction coefficient, $c_f \equiv \tau_w/q$, drops off slowly with Reynolds number based on the distance from the leading edge:

$$R_x = U_x/\nu; \quad c_f = 0.0296 \; (R_x)^{-1/5} \quad . \tag{9}$$

For Reynolds numbers in the range $R_x \approx 10^7$, the corresponding value of skin friction coefficient c_f is about 0.0022. This gives a value for p_{rms} equal to about 0.006 q. This is often taken as a typical value for turbulent-boundary-layer noise in incompressible flow.

For a launch vehicle to be hydraulically smooth, the roughness elements must be small enough to be buried in the laminar sublayer 11/. For typical Reynolds numbers on such vehicles at max q, $R_x \approx 10^9$, the height of these roughness elements would have to be only 10^{-7} of their distance from the leading edge. Although the exterior skin of the vehicle is covered with roughness elements of various sorts, we will idealize the problem by making the following assumption: We assume that the "equivalent" roughness height k_s of these elements is 0.01% of their distance from the leading edge. At 3000 in. from the nose of the vehicle, this gives an equivalent roughness height of 0.3 in., which seems reasonable for a typical vehicle. With a roughness scale of $k_s/x = 0.0001$, the vehicle will be hydraulically rough above a Reynolds number of 10^6 11/. In this hydraulically rough flow regime, the skin-friction coefficient c_f is about 0.0035 for incompressible flow. This value is independent of Reynolds number and represents essentially the form drag on the roughness elements. For a compressible fluid, the skin-friction coefficient is slightly reduced owing to a decrease in density with increasing temperature near the wall.

An approximate expression for the growth of the boundary-layer displacement thickness δ^* along the vehicle can be found from the integral-momentum theorem relating boundary-layer growth to shear stress at the wall:

$$d\theta/dx = c_f/2, \tag{10}$$

where θ is the boundary-layer momentum thickness. For a fully developed turbulent boundary layer, the form parameter, $H = \delta^*/\theta$, is used to relate the displacement and momentum thicknesses. In Ref. 12, Clauser discusses the dependence of H on the skin-friction coefficient. Experimental results on smooth and rough plates in incompressible flow give a value for H of ~ 1.5 for a skin-friction coefficient of 0.0035. In compressible flow, the form parameter H increases owing to a rapid increase in δ^*. At a Mach number of 2, H is about 3.

The growth of δ^* with x is then

$$\delta^* = c_f Hx/2 \tag{11}$$

or, for the suggested values of c_f and H,

$$\delta^* \approx 0.0026\ x\quad . \tag{12}$$

Figure 3 shows δ^* as a function of x for a flat plate. Also shown are two commonly used formulas 11/ for δ^* for a smooth flat plate for U = 1600 ft/sec. The value of the kinematic viscocity ν for these curves has been taken as $\nu \approx 0.8 \times 10^{-4} \text{ft}^2/\text{sec}$, the value for air at -67°F, which is the ambient temperature above an altitude of 40,000 ft. The δ^* values for a smooth plate are, of course, less than those for a rough plate.

Either the boundary-layer displacement thickness or momentum thickness may be used to nondimensionalize the spectrum of the boundary-layer pressure fluctuations. δ^* has been used most often for this purpose, although the experiments of Ref. 25 suggest that θ would be a better scaling parameter for the full range of Mach numbers, since the momentum thickness is less sensitive to compressibility effects.

The level of the pressure fluctuations should reflect the increased value of skin friction due to roughness. For this value of c_f, the root-mean-square levels are predicted to be $p_{rms} \approx 0.01\ q$ in incompressible flow. Willmarth [13] noted that the values on a rough plate are actually slightly higher than predicted by $p_{rms} = 2.7\ \tau_w$.

For low supersonic Mach numbers, less than about 2, a value p_{rms}/τ_w of 4.5 would be more realistic [20]. In addition, the skin-friction coefficient for a smooth flat plate decreases somewhat; the ratio of skin-friction coefficient c_f to its value in incompressible flow c_{f_i} is about 0.85 for this Mach number regime. If this ratio holds also for a rough plate, the root-mean-square level of pressure fluctuations would be $p_{rms} \approx 0.015\ q$.

This discussion is not intended to be a derivation of the expected noise levels due to turbulent boundary layers on launch vehicles. Its purpose is merely to show how reasonable values for equivalent roughness can predict an increased level of pressure fluctuations for an attached turbulent boundary layer, plus an increase in boundary-layer displacement thickness and momentum thickness. These levels are quite typical of flight data on launch vehicles. Flight data from airplanes show much lower levels ($p_{rms} = 0.006q$) consistent with the observation that airplanes usually have the ribs and stringers inside the skin.

The prediction of actual boundary-layer thickness along a launch vehicle would require lengthy and complex calculations involving effects of pressure gradients and flow separation. Such calculations would be approximate at best. On the smooth portions of the vehicle where the boundary layer is attached, we take a value for δ^* equal to that for a rough flat plate at the same distance from the leading edge. The actual value of δ^* does not affect the level of the pressure fluctuations at a point, but rather the peak frequency of the spectrum. The maximum of a constant-percentage frequency-band spectrum occurs at a frequency $f\delta^*/U \approx 0.16$ [14], or $\omega\delta^*/U \approx 1$. If the momentum thickness θ is used as a scaling parameter, then $f\theta/U \approx 0.12$. The spectrum is quite flat about this frequency, with considerable energy for several octaves on either side of the center frequency. A composite spectrum is shown in Fig. 4. This represents a comparison of the wind-tunnel measurements of many investigators and represents a best fit to their data. This curve is taken from Ref. 14.

For the calculated value of δ^*, flight at $U \approx 1600$ ft/sec has a spectrum that peaks at a frequency given by $fx \approx 10^5$, where x is the distance from the leading edge in feet. In Fig. 3, the peak frequency is plotted as a function of x. A sketch of a typical launch vehicle is also shown in Fig. 3. The distortion is, of course, due to the logarithmic scale. Peak frequencies in a range from 800 to 300 Hz are predicted for the long cylindrical stages. These values compare well with available flight data at appropriate locations.

To estimate the effective mean convection velocity U_c of the fluctuating pressure field on the surface of the vehicle, the results that Kistler and Chen [10] obtained in a supersonic wind tunnel can be used. According to this study, the ratio of convection velocity U_c to free-stream velocity U is 0.75 for $M \leqslant 1.7$, 0.7 for $M = 2$, and 0.6 for $M \geqslant 3$.

1.3.3 Wake Impingement. - Throughout the high-q portion of the flight of a manned launch vehicle, the turbulent wake from the escape tower will cause an increase in the pressure fluctuation on the vehicle. An important source of aerodynamic noise will be the increased intensity of turbulence due to wake impingement on the nose of the vehicle and, to a lesser extent, on the downstream sections. In supersonic flow, an additional cource would be the unsteady shock-wake interaction. Available experiments show the level increasing in the supersonic range, possibly as a result of this effect.

Turbulent wakes in all Mach number regimes, from low subsonic to hypersonic, show many of the same characteristics. The dominant feature of these wakes is the large eddy structure. The most thoroughly investigated wake is that behind a circular cylinder. Below the critical Reynolds number of about 4×10^6, the eddies are periodically shed at a nondimensional frequency or Strouhal number $S = fD/U \approx 0.2$. Two-dimensional wakes for general bodies can be compared, on the basis of wake momentum thickness, to those of a cylinder, since the far wake should be a function only of the drag on the body.

Similarly, the experiments of Goldburg et al. 15, 16/, for both incompressible and hypersonic flow, have suggested that a Reynolds number and Strouhal number based on wake momentum thickness characterize wakes from a wide class of axisymmetric bodies. The momentum thickness for an axisymmetric body is

$$\theta = (C_D A/2\pi)^{1/2} , \qquad (13)$$

where C_D is the drag coefficient and A is the frontal area. For Reynolds numbers above 90, the large eddy structure dominates the wake.

The experiments on spheres show a wake eddy structure having a Strouhal number, based on sphere diameter, of 0.19 for incompressible flow and 0.33 for hypersonic flow ($M = 14$).

The hypersonic results for both cones and spheres correlate well with a Strouhal number based on wake momentum thickness, $S_\theta \approx 0.12$. The corresponding incompressible-flow results were made in a Reynolds number range for which both the drag coefficient and the Strouhal number were varying quite rapidly, $R < 1000$. For $10^3 < R < 10^5$, the experiments of Ref. 17 show that $fd/U \approx 0.2$ for a sphere. The experiments are quite sensitive to the presence of boundary layer transition or shear layer transition. Some of the experimental results also indicate a branch for which $S = fd/U$ increases with Reynolds number to a value of 1.4 at $R = 8 \times 10^3$, suddenly falling to $S = 0.2$ and thereafter remaining constant. The Reynolds number of interest for launch-vehicle escape towers are well above this very sensitive range, and a dominant frequency $fd/U \approx 0.2$, based on tower-base diameter, is expected.

Experimental results for the pressure fluctuations on the nose of launch vehicles with various escape-tower configurations are reported in Refs. 18 and 19. The location of the pressure transducers on the forward cone in these experiments is indicated in Fig. 5. Transducer 1 was present in both tests, transducer 2 in the tests of Ref. 19 only.

The actual level of $C_{p_{rms}}$ is dependent upon details of the tower configuration and angle of attack of the vehicle. Figure 6 presents a boundary of maximum level to be expected as a function of Mach number for these two transducer locations. The level at transducer 2 is higher, possibly because this location is more apt to interact with the region of greatest shear in the turbulent wake.

The individual results for various tower configurations and for a range of angles of attack between + 6° and - 6° form a thicket of curves below these boundaries. The individual curves show some differing trends with Mach number, dependent upon the details of the configuration and the angle of attack.

The available spectra for these experiments peak at a Strouhal frequency of about 0.2, based on tower-base diameter. A nondimensional power spectrum $C_p(fd/U)/C_{p_{rms}}$ in third-octave bands is shown in Fig. 7.

The convection velocity for the motion of these large wake eddies should be taken as $U_c/U_\infty \approx 0.5$, a value more characteristic of wake flow, rather than $U_c/U_\infty \approx 0.8$, the value for a fully developed turbulent boundary layer.

1.3.4 Subsonic Flow Separation. - In subsonic flight, the turbulent boundary layer will experience a strong pressure gradient at cone-cylinder junctions. Regardless of whether the turbulent boundary layer actually separates, the level of pressure fluctuations will increase owing to an increase in the rate of momentum entrainment necessary to overcome the pressure gradient. The level of fluctuation increases with the turning angle and decreases with distance downstream as the boundary layer approaches an equilibrium state.

A few experimental results on cone-cylinder subsonic separation are reported in Refs. 18, 19, and 20, although the main emphasis in these reports is on transonic buffeting which takes place on the same area of the vehicle at slightly higher Mach numbers. Since the levels are much higher for this portion of the vehicle in the transonic flow, the details of subsonic separation have not been thoroughly investigated. The data available on this flow phenomenon is, therefore, not sufficient to predict the complete pattern of level and spectra.

Some preliminary estimates for the level of pressure fluctuations and the downstream decay have been made using the available experimental results. The downstream decay in the level of pressure fluctuations is shown in Fig. 8. This result , for a turning angle of 33° at a Mach number of 0.7, has been taken from Ref. 19. The data has been normalized to the value of $C_{p_{rms}}$ at an x/D of about 0.2. It seems reasonable to use this general decay law for all turning angles, especially since nothing else is available. Figure 9 shows the value for $C_{p_{rms}}$ as a function of turning angle, θ, for transducers located between $x/D = 0.12$ and 0.2. Because of the approximate nature of this summary, no attempt has been made to apply the downstream decay factor to these levels. These two figures should give an estimate of the levels to be expected aft of cone-cylinder junctions. These levels will eventually decay to those associated with a turbulent boundary layer in a uniform pressure field.

Experiments are not available to define adequately the spectra and convection speeds for subsonic boundary layers in adverse pressure gradients. A few general statements can, however, be made based on the available experimental evidence.

The spectra for subsonic separation show a shift to lower frequencies, which seems to be an efficient way for the boundary layer to gain momentum.

The convection speeds, if such a quantity can be defined for a separated region, are lower than those for a turbulent boundary layer in a uniform pressure field.

1.3.5 Transonic Shock Boundary-Layer Interaction. - One of the most serious problems in aerodynamic excitation of launch vehicle structures is transonic buffeting. As a result, this phenomenon has been extensively studied, and, although many questions remain open, it seems possible to predict, at least, the root-mean-square level of pressure fluctuation to be expected.

At high subsonic Mach numbers, local supersonic flow regions appear on the vehicle as the flow is accelerated by expansive turning which takes place on launch vehicles aft of cone-cylinder junctions.

These supersonic regions are terminated by shocks that cause the boundary layer to separate, resulting in an unsteady shock-boundary interaction quite typical of the transonic flow regime. A sketch of the flow aft of a cone-cylinder junction at transonic speeds is shown in Fig. 10.

The complete flow pattern of shocks, separation, reverse flow, and boundary-layer reattachment oscillates in the streamwise direction at fairly low frequencies. The result of this oscillation on the unsteady pressure fluctuations on the vehicle surface is also shown in Fig. 10. In this sketch, point 2 is always in the separated flow region, while points 1 and 3 are alternately in the attached and separated flow regions. The unsteady pressure fluctuation at points 1 and 3 owing to shock oscillation has the form of a random rectangular wave as these points are alternately ahead of and behind the shock.

A comprehensive summary and correlation of much of the available wind-tunnel data on this phenomenon is given by Wiley and Siedl [20]. The time-pressure waveforms in Fig. 10 have been taken from their report.

The correlation of data from this report shows that the level of pressure fluctuation increases with increasing turning angle θ and decreases with nondimensional distance downstream of the corner, x/D. From experiments on different vehicles, Wiley and Seidl have evolved a series of design charts to predict the maximum level to be expected as a function of θ and the downstream decay as a function of x/D. Figures 11 and 12 of this report reproduce this summary of available data. Figure 11 shows the maximum value of $C_{p_{rms}}$ expected as a function of θ and x/D. Figure 12 shows the Mach number at which this maximum occurs, for a given turning angle and x/D. As the Mach number increases, the shock region moves downstream and the intensity of the pressure fluctuation decreases.

The spectrum of the resulting pressure fluctuation is difficult to predict. The data of Refs. 20 and 21 suggests that the peak frequency for shock oscillations decreases with increasing distance downstream. This might be expected on physical grounds, since the greater the shock distance from the corner, the larger the region of separation and reverse flow can be, with resulting lower characteristic frequencies associated with larger eddies.

From the data of Refs. 20 and 21, a few calculations have been made which indicate a scaling based on distance from the corner. The Strouhal number based on x, fx/U, was about 0.045 for a surprising number of tests. This seems to be valid until $x/D \approx 0.5$. After this point, the sequence of spectra with Mach number indicate that the low-frequency shock boundary-layer interaction is not as dominant, and the energy shifts to the higher frequencies more characteristic of a turbulent boundary layer. A nondimensional spectrum based on this assumed scaling, $fx/U \approx 0.045$, is shown in Fig. 7. This spectrum has been taken from the tests of Ref. 20 as representative for transonic shock boundary-layer interactions.

A reasonable fit to this spectrum shape can be made by calculating the spectrum of a random rectangular wave that oscillates between two values that differ by a magnitude a. If $\overline{t}_k$ is the average time spent at the high pressure and $\overline{t}_i$ the average time spent at the low pressure, the spectrum is given by 20/

$$S(f) = 4a^2[(2\pi f)^2 + \{((\overline{t}_i+\overline{t}_k)/ \overline{t}_i\overline{t}_k)\}^2]^{-1}(\overline{t}_i+\overline{t}_k)^{-1} \ . \qquad (14)$$

In Ref. 20, the experimental results from which the shock oscillation spectrum given in Fig. 7 was obtained was also analyzed to determine average values for $\overline{t}_k$ and $\overline{t}_i$. The spectrum as derived from Eq. (14) with these values of $\overline{t}_i$ and $\overline{t}_k$ is shown as a dashed curve. The agreement is rather good, although the peak frequency predicted is high.

No information is available at this time on the spatial amplitude of shock travel. Consistent with the scaling ideas proposed here, this could be taken as some fraction of the distance to the corner.

1.3.6 Shock-Induced Separation at Interstage Flares. - During the supersonic portion of the flight trajectory of a launch vehicle, the turbulent boundary layer will be subject to a strong pressure rise near the interstage flare owing to an oblique shock that compressively turns the flow. If this pressure rise is sufficiently strong, shock-induced boundary-layer separation will occur. The oblique shock and the resulting separation point will move upstream of the flare and the flow will become unsteady.

Owing to shock oscillation, the region near the separation point has a high level of root-mean-square pressure fluctuations. Most of the energy of this disturbance is at low frequencies. Also, the separated region behind the shock will have very high pressure-fluctuation levels with a spectrum more characteristic of an intense turbulent boundary layer with an increase in displacement thickness.

To determine when and if the turbulent boundary layer will separate at the flare, we examine the experiments of Kuene [22,23]. These experiments were carried out on both two-dimensional flares and three-dimensional flared bodies of revolution. The object of these investigations was to determine what pressure rise would be allowed as a function of Mach number and Reynolds number before the turbulent boundary layer would separate. The range of Mach numbers M_o that were tested was 1.5 to 3.5. The range of Reynolds numbers R_{δ_o}, based on boundary-layer thickness δ_o obtained in these tests, was about 10^4 to 10^5; whereas, on a typical launch vehicle, the Reynolds number based on δ_o is more apt to be in the range of 10^6 to 10^7. The results of these experiments are presented in Fig. 13, which shows the pressure rise that will be tolerated for different Mach numbers as a function of Reynolds number R_{δ_o}. These experiments were performed on both two- 22/ and three-dimensional 23/ compression corners. The results indicate that, in the high-Reynolds-number, low-Mach-number range, the values of (p_1/p_o) for incipient separation versus R_δ are the same in both two and three dimensions. The results in Fig. 13 show that separation is more likely to occur for a given static pressure rise as the Reynolds number R_δ is increased and as the Mach number M_o is decreased.

The curves of Fig. 13 were extrapolated in a reasonable but probably risky way to a Reynolds number of 10^6. The results of this extrapolation are shown in Fig. 14. The experimental results for $R_{\delta_o} \approx 10^4$ and $R_{\delta_o} \approx 10^5$ are also shown in Fig. 14. These curves should give an estimate of when shock-induced separation will occur on launch vehicles for a known flare angle θ.

When boundary layers separate at steps or flares, there is a characteristic pressure rise that seems to be a function of Mach number. Experimentally determined values of this plateau 10, 22, 23, 25/ pressure p_p from several sources are also shown in Fig. 14. If the boundary layer separates, the strength of the first shock that occurs at the separation point is determined by this plateau pressure ratio.

Limited experimental data is available at this time concerning the pressure fluctuations in a separated supersonic flow. Experiments on flares have recently been carried out by Coe at Ames Research Center, but this data is not yet available. We must therefore examine data on related configurations.

Kistler has measured both static and fluctuating pressure before a step at M = 3. His results are summarized in Figs. 15 and 16. The fluctuating pressures in the region of separated flow are of two distinct types.

Near the separation point, an intense local low-frequency disturbance exists. This is owing to the oscillation of the shock. Behind the shock, the level of pressure fluctuations is an order of magnitude above the level of the turbulent boundary layer in front of the shock. The spectrum of these fluctuations is broad and more characteristic of a turbulent boundary layer with an increased displacement thickness.

Significant in this experiment is the time waveform at station 2, near the separation point as shown in Fig. 15. This square-wave shape indicates that the smooth static pressure distribution is just the time average of the abrupt pressure jump due to the oscillating shock similar to that observed in transonic flow. Kistler [10/] shows that the root-mean-square levels due to shock oscillation may be obtained from the static or time-average pressure distribution. He defines a parameter $\epsilon(x)$ as the fraction of time the pressure at x is equal to the higher pressure p_2. If the shock is assumed to be a discontinuous jump from p_1 to p_2, $\epsilon(x)$ can be found from the static pressure distribution, since

$$\overline{p}(x) = \epsilon(x)p_2 + [1-\epsilon(x)]p_1 \ . \qquad (15)$$

The mean-squared pressure fluctuations would then be given by

$$\langle[p(x,t) - \overline{p}(x)]^2\rangle_{\text{low freq. due to shock}} = \epsilon(1-\epsilon)(p_1-p_2)^2, \qquad (16)$$

$$\langle[p-\overline{p}(x)]^2\rangle_{\text{due to turbulent fluctuation}} = \overline{\epsilon p_2'^2} + (1-\epsilon)\,\overline{p_1'^2}, \qquad (17)$$

where $\overline{p_1'^2}$ and $\overline{p_2'^2}$ are the levels due to turbulent boundary layer fluctuations before and after the shock (see Fig. 16). The agreement between the calculations of the root-mean-square levels and Kistler's experiment is quite good. The same assumptions should also be valid for separation in front of interstage flares.

For shock-induced separation, the pressure rise through the shock is determined by the characteristic plateau pressure (see Fig. 14). If p_o is the pressure before the shock, and p_p the plateau pressure in the separated region, the maximum root-mean-square level due to the oscillation shock occurs for $\epsilon(x) = 1/2$. At this point,

$$\sqrt{\overline{p^2}} = (p_p - p_o)/2 = p_o[(p_p/p_o)-1]/2 = (p_o/2)(\Delta p/p_o) \quad . \tag{18}$$

The expression $\Delta p/p_o$ can be found from Fig. 14 as a function of Mach number.

The root-mean-square fluctuations $(\overline{p_2'^2})$ due to increased turbulence intensity behind the shock cannot be calculated analytically, and a definitive set of experiments on separated supersonic flows has not been made. We must, therefore, resort to empirical reasoning to predict approximately the noise levels to be expected. The physical assumption that underlies the reasoning is that pressure fluctuations in the turbulent boundary layer should be proportional to the rate of momentum entrained by mixing. In other words, in order to overcome an adverse pressure gradient and wall shear forces, the turbulent boundary layer must entrain momentum from the free stream by mixing. This vigorous mixing is seen as the cause of the pressure fluctuations.

The pressure fluctuations in a turbulent boundary layer are proportional to the rate of momentum entrained. For a boundary layer in zero pressure gradient, this momentum is used to overcome the wall shear. For a boundary layer in an adverse pressure gradient, almost all of the momentum is used to overcome the pressure rise. The rate of momentum gain by a separated layer can be estimated by examining the discussion of Williams [25]. He postulates (a) that the upstream position of the shock in front of the flare must be sufficient to enable the separated layer to gain the momentum necessary to overcome the second pressure rise at the flare (see the sketch in Fig. 14), (b) that the rate of momentum gain per unit length is proportional to $\rho_p u_p^2$, and (c) that the force due to the pressure rise to be overcome by the gain in momentum is $(p_1 - p_p)\delta$. The experimental data for separated layers at flares correlate fairly well with this parameter. A straight line drawn through the data presented in his note indicates that

$$L/\delta \approx 25(p_1 - p_p)/p_p M^2 \; . \qquad (19)$$

If we calculate the rate of momentum entrainment per unit length c_m, relative to $\rho_p u_p^2/2$ outside the boundary layer, we obtain

$$c_m = (p_1 - p_p)(\delta/L)(\lambda p_p M_p^2/2)^{-1} = (\Delta p \delta)(L p_p u_p^2/2)^{-1}$$

$$\approx 0.05 \text{ to } 0.06 \qquad . \qquad (20)$$

In reality the mixing takes place about a distance L up the flare, so the rate of momentum entrained need be only half that indicated by this equation, or $c_m \approx 0.025$ to 0.030. If we assume that this momentum gain is proportional to the root-mean-square pressure fluctuations in the same way as for a boundary layer in a zero pressure gradient, we obtain a maximum root-mean-square level of

$$c_{p_{rms}} = p_{rms}/q_p \approx 2.7\ c_m \approx 0.068 \text{ to } 0.08 \quad . \tag{21}$$

To the accuracy of these assumptions, q could be taken as free-stream dynamic pressure. Consistent with the scaling postulated for shock oscillation in Section 1.3.5, the frequency should be a function of the size of the separated region. Very little data is available to confirm this. The results of Ref. 25, when scaled on this basis, have a Strouhal number $fx/U = 0.06$ for the flow separation before a step at $M = 3.45$.

1.4 Appropriate Mathematical Models for the Environments

In order to facilitate analyses for estimation of structural response, we must endow the environmental noise sources discussed above with some degree of idealization. We devote this subsection to this task.

1.4.1 Acoustic Noise During Lift-Off. - We assume the acoustic noise field to be diffuse. In other words, in any frequency band, the sound field consists of a multitude of uncorrelated plane waves of equal intensity traveling in all possible directions with a uniform density.

1.4.2 Fluctuating Pressure Field Associated with a Turbulent Boundary Layer under Smooth Flow Conditions. - Experiments 13, 14/ indicate that in the fluctuating pressure field under a turbulent boundary layer, the properties characterizing the decay and convection of pressure "eddies" depend on the free-stream velocity and eddy size. Pressure fluctuations having progressively smaller spatial range are carried forward by the flow at progressively smaller convection velocities; in other words, smaller eddies, being closer to the wall, suffer less convection than larger eddies. Also, smaller eddies remain coherent for shorter spans of time than do larger eddies. The extent of this eddy decay in time also depends on eddy-convection velocity.

The mathematical model we have chosen for the turbulent-boundary-layer (TBL) pressure fluctuation field, however, ignores the above subtleties. We first give a brief account of this simple model and then provide an intuitive justification for our choice.

We assume that the fluctuating pressure field $p(\underline{x},t)$ on the surface of a structure is statistically homogeneous and stationary in time t and space $\underline{x} = (x_1,x_3)$*. Here, x_1 is the direction of the flow and x_3 is transverse to the flow.

The distribution of eddy size in the fluctuating pressure field can be expressed mathematically in the form of the normalized wavenumber spectrum $\Phi_{13}(\underline{k})$. We assume that this wavenumber spectrum can be factored into components $\Phi_1(k_1)$ and $\Phi_3(k_3)$. We also assume that the fluctuating pressure field is convected with a velocity U_c in the direction x_1 of the flow, and that this convection velocity is independent of the wavenumber $\underline{k}$. Lastly, we assume that the temporal decay of all the pressure eddies (or the wavenumber components) is characterized by a single

---

* Vector notation will be used wherever possible. Thus $\underline{x} = (x_1,x_3)$, $\underline{k} = (k_1,k_3)$, $d\underline{k} = dk_1\, dk_3$, etc.

"temporal" or "moving-axis" spectrum $\Phi_m(\omega)$. The above assumptions then enable us to express the combined wavenumber and frequency spectrum for the fluctuating pressure field [27]:

$$\Phi_p(\underline{k},\omega) = p_h^2 \, \Phi_1(k_1) \, \Phi_3(k_3) \, \Phi_m(\omega - k_1 U_c) \ . \tag{22}$$

Here, $\underline{k}$ is the wavenumber vector (k_1, k_3), ω is the radian frequency, p_h^2 is the over-all value of the mean-squared pressure fluctuations, and Φ_1, Φ_3, and Φ_m are the normalized "spatial" and "temporal" spectra. The familiar frequency spectrum, obtained by filtering the data measured by a "fixed" microphone, is then given by *

$$p_h^2 \, \Phi_f(\omega) = \iint \Phi_p(\underline{k},\omega) \, d\underline{k} \ , \tag{23}$$

or

$$\Phi_f(\omega) = \int \Phi_1(k_1) \, \Phi_m(\omega - k_1 U_c) \, dk_1 \ . \tag{24}$$

Here, $\Phi_f(\omega)$ is the normalized "fixed-microphone" spectrum.

As we shall see in Section 3, for common situations of interest in launch-vehicle dynamics, the structural vibration at "resonance and coincidence" dominates the response. For such a case, the pressure spectra that enter directly into the response estimates are the fixed-microphone spectrum $p_h^2 \, \Phi_f(\omega)$ and the wavenumber spectrum $\Phi_3(k_3)$ in the transverse direction. Thus

---

* In this report, unless otherwise stated, all the integrals are definite, with the range of integration from $-\infty$ to $+\infty$.

we bypass the necessity of specifying the detailed shape of the wavenumber spectrum $\Phi_1(k_1)$ or the temporal spectrum $\Phi_m(\omega)$. This economy in input information is due to the experimentally established fact that the temporal spectrum $\Phi_m(\omega)$ is relatively "sharp," with significant values only at low frequencies. In such a case, the temporal spectrum is influential only to the extent to which it distinguishes between relation (24) for the normalized fixed-microphone spectrum $\Phi_f(\omega)$, and the following relation (the "Taylor hypothesis"):

$$\Phi_f(\omega) = \Phi_1(k_1 = \omega/U_c)/U_c \ . \tag{25}$$

The discussion in Section 1.3 enables us to estimate the fixed-microphone spectrum $p_h^2 \ \Phi_f(\omega)$ in terms of trajectory and geometric parameters. For the wavenumber spectrum $\Phi_3(k_3)$, we assume the following form:

$$\Phi_3(k_3) = (2\delta^*/\pi)[(2k_3\delta^*)^2 + 1]^{-1} . \tag{26}$$

This corresponds to an exponentially decaying correlation in the x_3 direction, with a "correlation length" of $2\delta^*$ 26, 27 /

Justification for the Simple Model. - As we noted above, our present interest is in estimation of structural response at "resonance and coincidence." Even though the extent of eddy decay may vary for different wavenumbers, the temporal spectra $\Phi_m(\omega)$ appropriate for different wavenumbers would still be "sharp" in the sense described above. In that case, response formulas at "coincidence" from a more sophisticated model will also contain explicitly only the fixed-microphone spectrum $p_h^2\Phi_f(\omega)$ and a multiplying factor which, for the simple model described above, turns out to be $\Phi_3(k_3)$. The details of the eddy decay will not appear explicitly at "coincidence"; this information will be "contained" in the fixed-microphone spectrum. Furthermore, experiments [13/] suggest that the convection velocity varies roughly from 0.8 U_∞ at low wavenumbers (or at low frequencies filtered through a fixed microphone) to 0.6 U_∞ at high wavenumbers, U_∞ being the free-stream velocity. Such a variation can easily be introduced in relation (22) (in favor of a mean convection velocity of, say, 0.7 U_∞), but this will only shift the final response spectra on the frequency scale by a fraction of a third-octave band, at most.

In contrast to the above situation, for frequencies above the hydrodynamic critical frequency f_h for a structure (see Section 3), the resonant and "noncoincident" vibration becomes important. Such vibration is controlled by the temporal decay of the pressure eddies. The temporal spectrum $\Phi_m(\omega)$ is found to appear explicitly in the final response estimates. Hence the details of variation of convection velocity and temporal decay with wavenumber assume significance in such a case [27/]. These situations arise in low-velocity flows -- for example, in sonar and other underwater applications.

1.4.3 Surface Pressure Fluctuations Associated with Subsonic and Supersonic Separation, Shock-Induced Separation, and Wake Impingement.

- Detailed knowledge regarding the fluctuating pressure fields associated with the above phenomena, unfortunately, does not exist to date. Future experiments, we hope, will provide us with information such as the relative importance of the spatial and temporal fluctuations in the associated pressure fields, the shape of the correlation functions, and the variation of mean convection velocity with Mach number. The best that we can do at the present stage is to assume that the lacking details for the above flow phenomena bear a qualitative similarity with those of the fluctuating pressure field associated with a turbulent boundary layer under smooth-flow conditions. Therefore, for estimating structural response from environmental excitation under the conditions of subsonic and supersonic separation, shock-induced separation, and wake impingement, we shall use the mathematical model described in the previous subsection for a smooth-flow TBL pressure field. We shall, of course, assume appropriate numerical values (discussed in Section 1.3) for the magnitude of the boundary layer displacement thickness, the over-all mean-squared value of the pressure fluctuations, and the shape of the fixed-microphone spectrum.

1.4.4 Oscillating Shock. - We shall assume the following static pressure field to be associated with a shock front. The pressure in front of and behind the shock front has constant values. There is a discrete jump Δp in pressure across the shock front. If the shock front (and the associated static pressure field) oscillates in the direction x_1 parallel to the main flow, we assume that the shock front always remains straight in the transverse direction x_3. That is, there is no relative motion between different positions of the shock front in the x_3 direction. We also assume that the displacement $y(t)$ of the shock front from its mean position is essentially oscillatory, but with a certain degree of randomness. We assume this random motion $y(t)$ to be temporally homogeneous, with an associated spectrum $\Phi_y(\omega)$, which is narrow band, and has a sharp peak at the shock-oscillation frequency ω_{osc}. Further details regarding excitation from an oscillating shock are provided in Section 3.4. Note that the fluctuating pressure field that we have assumed to be associated with an oscillating shock front is statistically homogeneous in time but not in space.

SECTION 2
SOME IDEALIZED STRUCTURES

2.1 Introduction

In this section we present various dynamical properties of two simple structural elements, a flat plate and a cylinder. In order to handle most situations of interest, we study these structures in their finite as well as their infinite form, and in their orthotropic as well as their isotropic form. Also, we shall consider the case where a liquid (inside the cylinder, or on one side of the plate) forms an integral part of the structure.

2.2 Pressure-to-Velocity Wave Admittance for Infinitely Extended Structures

When the exciting pressure field is statistically homogeneous over the surface of the responding structure and when the discontinuities due to the structure boundaries do not play a significant role, it is worthwhile to exploit these simplifications by using an infinitely extended model of the structure.

2.2.1 Infinitely Long Isotropic Cylinder or Plate. - Consider an infinitely long, isotropic, cylindrical shell of radius a, thickness h, and material density ρ_m. Let the axial and circumferential directions on its surface be denoted by x_1 and x_3, respectively. Consider a pressure wave $p(\underline{x},t)$, given by relation (26), to propagate along the cylinder surface. The velocity $v(\underline{x},t)$ of the cylinder surface in the outward radial direction is then proportional to $p(\underline{x},t)$, and the factor of proportionality $H(\underline{k},\omega)$ is a function of the wavenumber $\underline{k}$, the frequency ω, and the properties of the cylinder.

$$p(\underline{x},t) = P \exp[i\, \underline{k} \cdot \underline{x} - \omega t] \ , \tag{26}$$

$$v(\underline{x},t) = p(\underline{x},t)\ H(\underline{k},\omega)\ , \tag{27}$$

$$H(\underline{k},\omega) = (i\nu a/\rho_s c_\ell)\,[\,r^4 + \cos^4\theta - \nu^2\,]^{-1} \tag{28}$$

Here, ρ_s is the surface mass density, c_ℓ is the velocity of the longitudinal waves in the cylinder material, r and ν are the dimensionless wavenumber and frequency,

$$\rho_s = \rho_m h\ , \tag{29}$$

$$\nu = \omega a/c_\ell \tag{30}$$

$$\underline{k} = (k_1,k_3)\ , \tag{31}$$

$$k = |\underline{k}|\ , \tag{32}$$

$$k_1 = k\cos\theta\ , \tag{33}$$

$$k_3 = k\sin\theta\ , \tag{34}$$

$$r = k(\kappa a)^{1/2}\ , \tag{35}$$

$$\kappa = h/(12)^{1/2}\ . \tag{36}$$

The function $H(\underline{k},\omega)$ [relation (28)] is the desired pressure-to-velocity wave admittance. It can be obtained from the differential equations of motion for a thin cylindrical shell vibrating in its axial, circumferential, and radial directions. In deriving relation (28), the influence of bending and membrane stresses is accounted for in the simplest possible way; the influences of shear deformations and of axial and tangential inertias are neglected. In spite of these approximations, the final result [relation (28)] has been found to be exceedingly accurate; especially for thin cylinders with thickness-to-diameter ratio of the order of 10^{-2} or less [28,29].

If we think of the admittance in relation (28) in terms of energy functions, the kinetic energy of the system is proportional to ν^2, the contribution to the potential energy from the bending stresses is proportional to r^4, and the contribution to the potential energy from the membrane stresses is proportional to $\cos^4\theta$.The corresponding result for an infinite flat plate can be obtained by omitting the term $\cos^4\theta$ in relation (28),since the effect of curvature and resulting membrane stresses is absent in a flat plate.

We obtain the resonance condition from relation (28) by equating the potential and kinetic energies,

$$\nu^2 = r^4 + \cos^4\theta \quad . \tag{37}$$

The loci of constant resonance frequency ν in the (r,θ) plane are shown in Fig. 17. In the "membrane region" of the (r,θ) plane, $\cos^4\theta$ is larger than r^4; thus membrane stresses dominate and the resonance condition becomes approximately

$$\nu = \cos^2\theta \quad . \tag{38}$$

The constant-resonance-frequency loci in the "membrane region" are thus radial straight lines. In the "bending region" of the (r,θ) plane, r^4 is larger than $\cos^4\theta$; therefore, bending stresses dominate, the structure responds like a flat plate, and the resonance condition becomes approximately

$$\nu = r^2 \quad . \tag{39}$$

The constant-resonance-frequency loci in the "bending region" are therefore circles. The "boundary" between the membrane and the bending regions consists of two circles,

$$\nu^2 = \cos^2\theta \quad . \tag{40}$$

In Fig. 17, only the positive quadrant of the (r,θ) plane is shown. The extension to the other three quadrants is straight forward.

2.2.2 Infinitely Long Orthotropic Cylinder or Plate. -

For the isotropic cylinder considered above, the wall thickness h entered directly in the determination of the kinetic energy and the two components of the potential energy of vibration. For the corresponding orthotropic structure, three "thicknesses" or length scales must be used: "inertial" thickness, which enters into the kinetic energy; "extensional" or "membrane" thickness, which enters into the potential energy of the membrane stresses; and "bending" thickness, which enters into the potential energy of the bending stresses. The last two lengths can have different values in the axial and circumferential directions of the cylinder. These thicknesses are defined as follows:

$$\text{Inertial thickness } h = \frac{\text{Average surface mass density } \rho_s}{\text{material density } \rho_m} \tag{41}$$

Extensional thickness h_1

$$= \frac{\text{Average extensional rigidity in the axial direction}}{\text{Young's modulus } E} \tag{42}$$

Bending thickness or radius of gyration κ_1

$$= \left(\frac{\text{Average bending rigidity in the axial direction}}{Eh}\right)^{1/2} \tag{43}$$

Thickness h_3 and κ_3 for the circumferential direction are similarly defined. The effective thicknesses thus defined would of course be valid only for vibration with wavelengths larger than the spatial extent over which the structural properties are averaged.

As an example of these concepts, consider the corrugated structure in Fig. 18. For longitudinal vibration in the x_1 direction with wavelengths larger than the wavelength λ of the corrugation, the inertial thickness h will be larger than the thickness t, and the extensional thickness h_1 will be smaller than t. Also, the deformations and restoring forces involved would be of the in-plane or membrane variety even though, in detail, these would be caused by the bending of the individual corrugations.30/.

Reverting to the orthotropic cylinder, we further define

$$\alpha_1 = h_1/h \ , \alpha_3 = h_3/h \ , \tag{44}$$

$$c_3^2 = c_\ell^2 \alpha_3 \; , \tag{45}$$

$$r_m \cos\theta_m = k_1 a \alpha_1^{1/2} \; , \tag{46}$$

$$r_m \sin\theta_m = k_3 a \alpha_3^{1/2} , \tag{47}$$

$$r_b \cos\theta_b = k_1 (a\kappa_1)^{1/2} \tag{48}$$

$$r_b \sin\theta_b = k_3 (a\kappa_3)^{1/2} , \tag{49}$$

$$\nu_3 = \omega a / c_3 \quad . \tag{50}$$

Here, (k_1, k_3) is once again the wavenumber of vibration on the cylinder surface; (r_m, θ_m) and (r_b, θ_b) are the dimensionless wavenumbers that describe the membrane and the bending-controlled vibration. Finally, in place of relation (28) for $H(\underline{k},\omega)$, we have for the orthotropic cylinder $\underline{29/}$

$$H(\underline{k},\omega) = (i\nu_3 a/\rho_s c_3)[(r_b^4/\alpha_3) + \cos^4\theta_m - \nu_3^2]^{-1} \quad . \tag{51}$$

Discussion in terms of energies of vibration and resonance loci is analogous to that for the isotropic case, except that, in the present case, the "bending" and "membrane" regions of the wavenumber plane (k_1, k_3) are best described by two separate transformations.

2.2.3 *Infinitely Long, Isotropic and Fluid Loaded Cylinder or Plate.* - Consider an infinitely long, isotropic cylindrical shell filled with a liquid. We restrict our consideration to the case where the phase velocity of vibration on the cylinder surface is less than the sound velocity in the liquid, since this is the only situation encountered for the liquid-bearing components of a typical launch vehicle in which the liquids are mainly oxidizers and fuels. For such a case, detailed calculations show that, for a prescribed vibratory motion (in the radial direction) on the cylinder surface, the pressure exerted by the liquid on the cylinder surface is always out of phase with the velocity of the cylinder surface so that no net energy is exchanged (in the steady state) between the cylinder and the liquid. Also, the impedance offered by the liquid pressure to the cylinder vibration is inertial, the mass loading effect m_f per unit surface area owing to the fluid being approximately given by

$$m_f = \rho_o \left(k^2 - \omega^2 c_o^2\right)^{-1/2} \approx \rho_o / k \qquad (52)$$

Here, ρ_o and c_o are the density and the sound velocity for the liquid, ω is the frequency of vibration, and k is the magnitude of the wavenumber of vibration on the cylinder surface [see relations (31) and (32)]. As long as the vibration on the cylinder surface is acoustically slow* with respect to c_o, relation (52) for the mass loading effect is accurate, even though the nature of the detailed pressure field inside the liquid depends on whether the axial trace velocity of vibration on the cylinder surface is more than, equal to, or less than c_o [31]. Relation (52), of course, is valid also for a fluid-loaded, infinite flat plate.

---

* See Section 2.4.1 for definition of acoustically slow vibration.

With the help of relation (52), the (external) pressure-to-velocity wave admittance $H(\underline{k},\omega)$ can easily be written as an extension of relation (28):

$$H(\underline{k},\omega) = (i\nu a/\rho_s c_\ell)[\, r^4 + \cos^4\theta - \nu^2(1 + \beta/r)\,]^{-1} , \tag{53}$$

where the dimensionless fluid-loading parameter β is given by

$$\beta = \rho_o(\kappa a)^{1/2}/\rho_s , \tag{54}$$

and the rest of the nomenclature is that of Section 2.2.1.

The resonance condition now becomes

$$\nu^2(1 + \beta/r) = r^4 + \cos^4\theta . \tag{55}$$

Once again the boundary between the membrane and the bending regions of the (r,θ) plane is given by relation (40). However, there are some differences. The frequency below which membrane effects dominate (that is, $\cos\theta \geqslant r$) is lower with fluid loading. Also, except at very low frequencies, the loci of constant resonance frequencies in the membrane region of the (r,θ) plane are no longer radial straight lines; in fact, the loci tend rather to be the extensions of the circular resonance loci in the bending region. This is illustrated in Fig. 19, where resonance loci are shown for the case where the dimensionless fluid-loading parameter β is 7.54. This corresponds to liquid oxygen in an aluminum container 33 ft in diameter and 180 mil thick.

The simpler resonance conditions which hold approximately in the membrane or the bending region of the (r,θ) plane can easily be obtained from relation (55) by neglecting one or the other of the two terms on the right-hand side of relation (55)

2.3 Representation and Statistics of Modes and "Modal Oscillators" for Structures of Finite Extent

When the excitation field is not satistically homogeneous over the surface of the responding structure, or when the discontinuities such as the structure boundaries are expected to play a significant role, it is advantageous to consider the modal representation of the finite structure. Often, the analyses performed on highly idealized structures with simple boundary conditions yield concepts (and answers) powerful enough to find application in more general situations.

2.3.1 Modal Representation for a Cylinder and a Plate.- For the sake of brevity, we shall specialize and restrict our discussion to the two structures of interest, a flat plate and a cylinder [32].

Modal Representation for an Isotropic Cylinder. - Suppose that the isotropic cylindrical shell, which was discussed in Section 2.2.1, has a finite length ℓ_1 in the axial direction. If this cylinder is simply supported along the circumferential edges at its two ends, the velocity $v(\underline{x},t)$ of the cylinder surface in the outward radial direction can be expressed as a doubly infinite sum of its modal components $v_{mn}(t)$ as follows:

$$v(\underline{x},t) = \sum_{m}\sum_{n} v_{mn}(t)\; c_{mn}\; \psi_{mn}(\underline{x}) \; . \tag{56}$$

There are two orthogonal modal shapes $\psi_{mn}(\underline{x})$ for each pair of integers (m,n). These modal shapes are given by

$$\psi_{mn}(\underline{x}) = \sin(m\pi x_1/\ell_1)\, \cos(2n\pi x_3/\ell_3) \ ,$$

$$\psi_{mn}(\underline{x}) = \sin(m\pi x_1/\ell_1)\, \sin(2n\pi x_3/\ell_3) \ . \tag{57}$$

Here, m and n are positive integers and ℓ_3 is the circumference of the cylinder.

The normalizing constants c_{mn} can be found from the condition

$$\iint\limits_{\substack{\text{cylinder}\\ \text{surface}}} \rho_s\, c_{mn}{}^2\, \psi_{mn}{}^2(\underline{x})d\underline{x} = M, \tag{58}$$

where M is the total mass of the cylinder.

The wavenumber $\underline{k}$ is associated with the vibration of the mode (m,n) is given by

$$\underline{k} = (k_1,k_3) = (m\pi/\ell_1 \ , \ 2n\pi/\ell_3) \ . \tag{59}$$

Since all the modes are defined by the set of positive integers (m,n), the positive quadrant of the wavenumber plane (k_1,k_3) is sufficient for representing all the associated wavenumbers.

For a pressure field $p(\underline{x},t)$ exciting the cylinder surface, the "modal force" $F_{mn}(t)$ exciting the mode (m,n) is given by

$$F_{mn}(t) = \iint\limits_{\substack{\text{cylinder}\\ \text{surface}}} p(\underline{x},t)\ c_{mn}\ \psi_{mn}(\underline{x})\ dx \ . \tag{60}$$

Detailed consideration of the dynamics of the isotropic cylinder shows that, if the modal force $F_{mn}(t)$ is given by relation (61), the modal velocity $v_{mn}(t)$ is proportional to $F_{mn}(t)$, and the factor of proportionality or the modal admittance $H_{mn}(\omega)$ is given by relations (63) and (64) .

$$F_{mn}(t) = F\ e^{-i\omega t} \ , \tag{61}$$

$$v_{mn}(t) = H_{mn}(\omega)\ F_{mn}(t) \ , \tag{62}$$

$$H_{mn}(\omega) = (i\omega/M)[\omega_{mn}^{2} - \omega^{2}]^{-1} \ , \tag{63}$$

$$\nu_{mn}^{2} = (\omega_{mn} a/c_{\ell})^{2} = r^{4} + \cos^{4}\theta \ . \tag{64}$$

Here, ν_{mn} is the dimensionless frequency [relation (30)], and (r,θ) is the dimensionless wavenumber corresponding to the wavenumber $\underline{k}$ associated with the mode (m,n) [relations (59) and (31) to (36)].

Seeking dynamical analogy with a simple harmonic oscillator, we conceive of the mode (m,n) as a "modal oscillator" of mass M and natural frequency ω_{mn}. Furthermore, owing to the orthogonality of the mode shapes $\psi_{mn}(\underline{x})$, the total potential and kinetic energies of vibration of the whole cylinder are equal to the sum of the respective energies of the modal oscillators.

We note that, for this particular configuration of a cylinder simply supported along its circumferential edges, the natural frequencies ω_{mn} can be found from the resonance condition (37) for the corresponding infinitely extended cylinder. In fact, the modal force per unit area and the modal velocity are the spatial

Fourier transforms of the total pressure and velocity fields. Hence, we have

$$H_{mn}(\omega) = H(\underline{k},\omega)/A \ . \tag{65}$$

Here, A is the cylinder surface area, $H(\underline{k},\omega)$ is defined in relation (28), and $\underline{k}$ is the wavenumber associated with the mode (m,n). This equivalence between the dynamical properties of infinite and finite structures is, of course, destroyed for the clamped boundary conditions. In that case, there is some increase in the natural frequencies of the lower modes.

Modal Representation for an Orthotropic or Fluid-Loaded Cylinder. - For an orthotropic or a fluid-loaded cylinder simply supported at its circumferential edges, the geometry of the structure and the boundary conditions remain the same as those for the isotropic cylinder discussed above. Therefore, the modal shapes and the associated wavenumbers remain the same. As a result, we can immediately obtain the complete representation of the modal oscillators for the orthotropic or the fluid-loaded cylinder from relation (65), by using the appropriate pressure-to-velocity admittance $H(\underline{k},\omega)$ for the corresponding infinitely extended system. Nothing more need be said about the orthotropic case. For the case of fluid loading, we note that the effective modal mass M_f now incorporates the mass-loading effect of the fluid:

$$M_f = M(1 + \beta/r) \ . \tag{66}$$

Here, β is the fluid-loading parameter defined in relation (54). Note that the liquid loading on a finite structure would tend to couple the structural modes. We have ignored this consideration for the sake of simplicity and have considered the modes to remain uncoupled.

Modal Representation for a Flat Plate. - The modal description for a flat rectangular plate simply supported along its edges can be developed along exactly the same lines. The only modification necessary is due to the change in the orthogonal modal shapes $\psi_{mn}(\underline{x})$. For a flat plate, the modal shapes $\psi_{mn}(\underline{x})$ are given by

$$\psi_{mn}(\underline{x}) = \sin(m\pi x_1/\ell_1)\,\sin(n\pi x_3/\ell_3) \quad , \tag{67}$$

Here, ℓ_1 and ℓ_3 are the edge lengths of the plate. In contrast to a cylinder, odd numbers of wavelengths in the x_3 direction are now possible, but there is only one mode shape $\psi_{mn}(\underline{x})$ for each pair of integers (m,n). Owing to the change in $\psi_{mn}(\underline{x})$, the normalizing constants c_{mn} and the wavenumbers $\underline{k}$ associated with the modes change. Also, the admittance $H(\underline{k},\omega)$ for the corresponding infinite plate would have no contribution from the membrane stresses. Hence, with the exception of relations (57), (59), and (64), the modal description for a flat rectangular plate (isotropic, orthotropic, or fluid-loaded) is the same as that developed above for a cylinder.

2.3.2 Modal Density for a Cylinder and a Plate

- Modal density $n(\omega)$ is defined as the number of modes whose natural frequencies lie in a unit radian frequency band around ω. We shall calculate the modal density for an othotropic cylinder and a fluid-loaded isotropic cylinder. The modal densities for the remaining structures can be derived from these.

Modal Density for An Orthotropic Cylinder. - For an orthotropic cylinder, the natural frequencies of the modes are given by the resonance condition obtained from relation (51):

$$\nu_3^{\,2} = r_b^{\,4}/\alpha_3 + \cos^4\theta_m \ . \qquad (68)$$

We define the ring frequency ω_r by the relation

$$\omega_r = c_3/a \ . \qquad (69)$$

For a sufficiently long cylinder, the resonance locus at a frequency below the ring frequency passes approximately through the origin of the wavenumber plane. Figure 20 shows two shematic representations of such a locus in the dimensionless wavenumber plane (r_b, θ_b). The locus in solid line is determined by the resonance condition (68); the idealized locus is a combination of the approximate "membrane locus" and "bending locus" derived from relation (68). These approximate loci are:

$$\nu_3 = \cos^2\theta_m,$$

or

$$\tan^2\theta_b = \alpha_1\kappa_3(1-\nu_3)/\alpha_3\kappa_1\nu_3 \ , \qquad (70)$$

and

$$r_b^2 = \nu_3 \alpha_3^{1/2} . \tag{71}$$

The shaded area in the (r_b, θ_b) plane under the idealized locus is easily seen to be $[(\pi/2) - \theta_b] r_b^2/2$. Also, the area attributed to each pair of modes situated at the same location in the (r_b, θ_b) plane is $2\pi^2 a(\kappa_1 \kappa_3)^{1/2}/A$. This immediately gives the approximate number $N(\omega)$ of modes with natural frequencies less than ω:

$$N(\omega) = (A\omega/2\pi^2 \kappa c_\ell)[(\pi/2) - \theta_b] \qquad \text{for } \omega \leqslant \omega_r , \tag{72}$$

where θ_b is given by relation (70), A is the total surface area of the cylinder, and $\kappa = (\kappa_1 \kappa_3)^{1/2}$ is the (geometric) mean radius of gyration.

Approximating the resonance condition (68) by relation (71), one can similarly establish that, for frequencies higher than the ring frequency,

$$N(\omega) = A\omega/4\pi\kappa c_\ell \qquad \text{for } \omega \geqslant \omega_r , \tag{73}$$

The average value of modal density over a frequency band is

$$n(\omega) = [N(\omega_2) - N(\omega_1)]/(\omega_2 - \omega_1) , \tag{74}$$

where ω_2 and ω_1 are the upper and lower frequency limits of the band. Since the modal density is found from the *difference* between the cumulative modal counts $N(\omega)$ at two frequencies, the positive error introduced in relation (72) owing to the idealization of the resonance condition (68) (see Fig. 20) is largely removed. The resulting estimates for the modal density are found to agree very well with the more detailed calculations[33]

Modal Density for An Orthotropic Plate. - For an orthotropic rectangular plate, the membrane effects are absent and the odd-numbered modes are possible in the x_3 direction [compare relations (57) and (67)]. However, there is only one independent mode for each pair of integers (m,n). Therefore, the cumulative modal count $N(\omega)$ at all frequencies is the same as that given in relation (73).

Modal Density for An Isotropic Cylinder. - It is easy to specialize the above results for isotropic structures. For example, for an isotropic cylinder relations (72) and (73) simplify to

$$\begin{aligned} N(\omega) &= (\ell_1 \nu/\pi\kappa)\,\sin^{-1}(\nu) \qquad \text{for } \nu \leqslant 1 \\ &= \ell_1 \nu/2\kappa \qquad \text{for } \nu \geqslant 1\,. \end{aligned} \tag{75}$$

Here, ℓ_1 is the axial length of the cylinder, and ν and κ are given by relations (30) and (36). Calculation of the modal density $n(\omega)$ from relations (75) and (74) shows that, below the ring frequency $\omega_r = c_\ell/a$ the modal density increases with frequency. It attains its peak value at the ring frequency and maintains a constant value, roughly two-thirds of the peak value, above the ring frequency. This concentration of modes around the ring frequency is due solely to the fact that the ring frequency separates the two essentially different types of loci of constant resonance frequency in the (r,θ) plane (see Fig. 28).

Modal Density for a Fluid-Loaded Cylinder. - For a fluid-loaded cylinder, the transition in the nature of the resonance loci occurs at a frequency lower than the ring frequency c_ℓ/a [see Fig. 19 and the remarks after relation (55)]. For most practical situations of interest, the numerical values are such that the frequency range below this transition frequency (usually 30 H_z or lower for large launch vehicles) is of little interest. For the more interesting higher-frequency region, we estimate the modal density by considering the "bending-controlled" approximation of the resonance condition (55); that is,

$$\nu^2(1 + \beta/r) = r^4 \ . \tag{76}$$

This fifth-order equation in r can be solved in terms of ν by suitable approximations in different frequency ranges. For example, in the low-frequency range, β/r is greater than 1; in the intermediate-frequency range, β/r is roughly equal to 1; and in the high-frequency range, β/r is negligible compared with 1. These frequency ranges and approximate solutions for r can be found easily and are not detailed here. The cumulative modal count $N(\omega)$ in terms of r is given by

$$N(\omega) = \ell_1 r^2/2\kappa \ . \tag{77}$$

Finally, the modal density $n(\omega)$ can be found from relation (74).

2.4 Acoustical Radiation Properties of Structural Modes

2.4.1 Introduction. - In this section, we discuss the radiation damping of individual modes and the resulting structural radiation-loss factor in frequency bands.

Definition of Radiation Resistance. - Consider the vibration at frequency ω of the mode (m,n) of a finite structure. The air surrounding the structure would tend to impede this motion. Some of the vibratory energy of the mode will be converted into sound waves and propagate away from the structure into the surrounding space. Seeking analogy with a simple oscillator, we associate this power loss with a dissipating mechanism -- namely, radiation resistance R_{rad} -- which is characteristic of the shape of the mode (m,n) and the frequency of vibration ω [34]. Thus we define the modal radiation resistance $R_{rad}(\omega)$ as the ratio of the average power radiated due to the vibration of the mode at frequency ω to the mean-squared modal velocity at the same frequency.

Relation Between Radiation Resistance and Coupling Parameter. - Now consider the same structure to be surrounded by a diffuse sound field. If the pressure at the surface of the structure is $p(\underline{x},t)$, the modal force $F_{mn}(t)$ exciting the mode (m,n) will be given by relation (60). Let $p(\underline{x},\omega)$ and $F_{mn}(\omega)$ be the components of the pressure field and the modal force at frequency ω. $F_{mn}(\omega)$, which determines the vibration at frequency ω of the mode (m,n), depends on the extent of "coupling" or "spatial match" between $p(\underline{x},\omega)$ and the modal shape $\psi_{mn}(\underline{x})$. It has been shown, from the reciprocity principle, that the modal radiation resistance R_{rad} defined above is directly related to the magnitude of this coupling [35].

Classification of Modes. - At a particular frequency ω we can classify various modes as acoustically fast modes or as strip or corner acoustically slow modes, depending on the nature of this coupling. The component of the diffuse sound field exciting any mode at frequency ω would consist of a multitude of uncorrelated plane waves propagating in all possible directions. The wavenumber k_a associated with each wave would, of course, be given by

$$k_a = \omega/c \,, \tag{78}$$

where c is the speed of sound. The projection of this ω component of the diffuse field on the structure surface would consist of plane waves (propagating in different directions on the structure surface) with wavenumbers ranging from zero to k_a. If the magnitude of the wavenumber $\underline{k}$ associated with a mode is less than k_a(as with mode A in Fig. 21), a perfect spatial match would exist between the mode shape and some component of the projected excitation field. Such a mode is then called an acoustically fast mode, since the associated phase velocity $\omega/|\underline{k}|$ is higher than the sound speed c. An acoustically fast mode radiates and accepts acoustical energy over the entire surface of the structure. It is, therefore, called a "surface" mode also. Modes B, C, D, and E, in Fig. 21, are called acoustically slow modes, since for these modes the magnitude of the associated phase velocity of vibration is less than the sound speed c. All acoustically slow modes are characterized by, at best, a partial spatial match with the projected acoustic pressure field. The interaction between an acoustically slow mode and the sound field is restricted to a narrow strip of the structure surface near some portion of the structure boundary [32, 36]. An acoustically slow mode is classified in accordance with the portion of the structure boundary near which the mode interacts with the sound field. For example, in Fig. 21, mode B is called an "acoustically slow edge-1 mode" because it interacts with the sound field near the structure edges parallel to the x_1 direction. Note that, for an acoustically slow edge-1 mode, $k_3 > k_a$ but $k_1 < k_a$. The names given to acoustically slow modes C,D, and E, in Fig. 21, have similar interpretations.

2.4.2 Single-Mode Radiation Resistance for a Flat Plate or a Cylinder. - Here, essentially, we quote some of the results derived elsewhere 36, 37/. These results are presented in terms of the modal radiation efficiency σ_{rad}, which is related to the modal radiation resistance by the relation

$$\sigma_{rad} = R_{rad}/\rho c A \ . \qquad (79)$$

Here, ρc is the characteristic acoustic impedance, and A is the surface area of the structure.

An Isotropic Flat Plate. - At any frequency ω, the radiation efficiency of an acoustically fast (AF) mode of an isotropic, rectangular flat plate of size (ℓ_1, ℓ_3) is given by 36/

$$\sigma_{rad} = (1 - k^2/k_a{}^2)^{-1/2} \ .$$

Here, k is the magnitude of the wavenumber vector (k_1, k_3) associated with the mode and k_a is the acoustic wavenumber [relation (78)].

In deriving the above relation, the effects of fluid loading by the air have been neglected. When such loading is considered, the radiation efficiency for an AF mode can be approximated by

$$\sigma_{rad} = 1 \quad . \tag{80}$$

The radiation efficiency for an acoustically slow (AS) edge-3 mode (see Fig. 21) is given by

$$\sigma_{rad_3} = (k_a/k_1\ell_1)\ (k_1{}^2 + k^2 - k_a{}^2)/(k^2 - k_a{}^2)^{3/2} \quad . \tag{81}$$

The radiation efficiency σ_{rad_1}, for an AS edge-1 mode, is obtained from relation (81) by replacing ℓ_1 by ℓ_3 and k_1 by k_3. The radiation efficiency for AS corner modes is generally quite small and is ignored in this report.

An Orthotropic or Fluid-Loaded Plate. - One can look upon the modal radiation efficiency (for vibration at any frequency ω) as a spatial or geometric property of the modal shape $\psi_{mn}(x)$. Since, for a mode with an associated wavenumber (k_1, k_3), the modal shape does not change if the plate is orthotropic or fluid-loaded, the modal radiation efficiency (for vibration at the same frequency ω) for these cases also is given by relations (80) and (81).

An Isotropic Cylinder. - Exact derivation of the modal radiation efficiencies for a cylinder is quite cumbersome. However, a direct and elegant method has been evolved to solve the problem [36, 37]. First, the radiation efficiency of a mode for a flat plate is shown to be determined by a process of volume-velocity cancellation between adjoining "cells" of the vibration pattern of the mode [36]. Second, by studying similar volume-velocity-cancellation effects for the modes on a cylinder, it has been shown that the radiation efficiencies for the AF and the AS edge-3 modes of a cylinder are approximately given by relations (80) and (81), if one interprets the cylinder as an "equivalent plate" of dimensions ($\ell_1, \ell_3 = 2\pi a$). Here, ℓ_1 is the axial length of the cylinder and a is its radius. The difference between the geometry of a cylinder and a plate, however, shows up in the radiation efficiency for the AS edge-1 modes. For a cylinder, there really is no "edge" parallel to the axial direction, hence the AS edge-1 modes are acoustically "short-circuited" and their radiation efficiency is negligible [37].

An Orthotropic or Fluid-Loaded Cylinder. - The "equivalent plate" analogy described above also applies when an orthotropic or fluid-loaded cylinder is compared with an "equivalent" orthotropic or fluid loaded plate.

2.4.3 Average Radiation Resistance for a Flat Plate or a Cylinder.

- For many situations of interest, most of the vibration of a structure in any narrow frequency bandwidth consists of the vibration of the structural modes with their resonance frequencies in the same bandwidth. This will happen when the typical "modal bandwidth" is small and when there are resonant modes in each frequency band of investigation. For such multimodal resonant vibration, we define the structural radiation resistance in a frequency bandwidth as the average of the radiation resistance of the resonant modes in the same bandwidth, evaluated at their common resonance frequency. As we shall see in Section 3, the average radiation resistance thus found enters directly into the estimate for the structural response to a diffuse sound field.

An Isotropic Flat Plate. - Calculations for the average radiation resistance for an isotropic flat rectangular plate have already been performed [36]. The resonance condition for the plate is obtained by specializing relation (37). This condition is

$$\omega = \kappa c_{\ell} k^2 \ . \tag{82}$$

For a mode to be acoustically fast at its own natural frequency, it must resonate above the acoustic critical frequency ω_c. This, in fact, is how we define ω_c. From relations (78) and (82), it follows that

$$\omega_c = c^2/\kappa c_{\ell} \ . \tag{83}$$

The average radiation efficiency $\langle\sigma_{rad}\rangle$ for a flat plate can be expressed in terms of the acoustic critical frequency [36]. If

$$\alpha = (\omega/\omega_c)^{1/2}, \tag{84}$$

then,

$$\langle\sigma_{rad}\rangle = 1 \qquad \text{for } \alpha \geqslant 1 \tag{85}$$

$$= (P_r \lambda_c / A) g_2(\alpha) \qquad \text{for } \alpha < 1 \ , \tag{86}$$

$$g_2(\alpha) = (2\pi)^{-2}[(1-\alpha^2)\ \ell n\{(1+\alpha)/(1-\alpha)\} + 2\alpha](1-\alpha^2)^{-3/2} \ . \tag{87}$$

Here, $\lambda_c = 2\pi c/\omega_c$ is the acoustic wavelength at the critical frequency and $P_r = 2(\ell_1 + \ell_3)$ is the plate perimeter. Relation (85) is clearly the average of the radiation efficiency of AF modes [relation (80)] lying along the resonance locus which is a quarter of a circle in the wavenumber plane (k_1, k_3). Relation (86) is a similar average for the AS edge-1 and AS edge-3 modes. The small contribution from the corner modes is neglected here. The "edge effect" is seen to show up in the appearance of the perimeter P_r.

A Fluid-Loaded Plate. - If the flat rectangular plate discussed above is loaded by a liquid on one side, the resonance condition changes to the one given by relation (76). As discussed before, the single-mode radiation efficiencies remain the same. Also, the geometry of the situation in the wavenumber plane remains the same, since the resonance loci are still circles. Thus we can obtain $\langle\sigma_{rad}\rangle$ for the case of fluid loading by using relations (85) to (87) if we express relation (84) in terms of the wavenumbers involved; that is,

$$\alpha = k_a/k \ . \tag{88}$$

In fact, for the isotropic (not liquid-loaded) case, relation (84) was obtained from relation (88) by using relations (78), (82), and (83). In the present case, similar elimination of the wavenumbers must be accomplished by using relations (78) and (76). Approximate methods of solving the resonance equation (76) are briefly explained in the discussion following relation (76). The acoustic critical frequency ω_c is defined by the condition $k = k_a$, or $\alpha = 1$.

An Orthotropic Flat Plate. - For an orthotropic flat plate, the resonance loci become ellipses in the wavenumber plane (k_1, k_3). The resonance condition, obtained from relation (51) , is

$$\omega^2 = (\kappa_1 c_\ell k_1^2 + \kappa_3 c_\ell k_3^2)^2 \quad . \tag{89}$$

For the case $\kappa_1 > \kappa_3$, Fig. 22 schematically shows the acoustic wavenumber locus $k = |\underline{k}| = k_a = \omega/c$, and the resonance locus in the wavenumber plane for five different frequencies.* The higher critical frequency ω_{c3}, above which all the modes are acoustically fast, and the lower critical frequency ω_{c1}, below which all the modes are acoustically slow, are defined by

$$\omega_{c3} = c^2/\kappa_3 c_\ell \ , \tag{90}$$

$$\omega_{c1} = c^2/\kappa_1 c_\ell \ . \tag{91}$$

For $\omega > \omega_{c3}$, $<\sigma_{rad}>$ is clearly 1. For $\omega < \omega_{c3}$, the integrations required in averaging the modal radiation efficiency are unfortunately quite involved. The task must therefore be delegated to the computer. The calculation must average the radiation efficiency of each class of modes by taking a few representative points along the appropriate part of the resonance locus.

The situation for the case $\kappa_3 > \kappa_1$ can easily be described along similar lines.

An Isotropic Cylinder Above Its Ring Frequency. - Now consider an isotropic cylinder. Above the ring frequency $\omega_r = c_\ell/a$, the membrane effects are negligible, and the resonance condition for the cylinder becomes the same as that for an isotropic flat plate [see relations (37) - (39) and the related discussion]. Thus the "equivalent" plate analogy (described in connection with the single-mode radiation efficiency for a cylinder) becomes complete and we can use relations (82) to (87) for the cylinder as well. There is, however, one point of departure. For the cylinder, the perimeter P_r in relation (86) is to be taken as

---

* In connection with Fig. 22 and similar situations elsewhere, note that, when we discuss a resonance locus at a particular frequency ω or modes resonating at the same frequency, we imply a finite bandwidth of frequency and corresponding resonance "strips" in the wavenumber plane. It is simpler to use the pure-tone frequency variable and the resonance "lines" in the wavenumber plane. The calculations based on this procedure, however, are applicable only to finite bandwidths of frequency.

$$P_r = 2\ell_3 = 4\pi a \quad . \tag{92}$$

Here, a is the radius of the cylinder. The contribution to the perimeter from the "axial" sides of length ℓ_1 is omitted, since, as mentioned above, the axial strip modes (or AS edge-1 modes) are acoustically short-circuited, and their radiation efficiency is negligible [33].

An Isotropic Cylinder Below Its Ring Frequency. - The flat plate equivalence described above is restricted to frequencies above the ring frequency. Below the ring frequency, membrane stresses give rise to some AF modes. The quantitative estimate of the radiation efficiency for this frequency range can be obtained as a special case of the similar estimate for the orthotropic cylinder discussed below.

A Fluid-Loaded Cylinder. - For an isotropic cylinder filled with a liquid, a similar "equivalent plate" analogy exists with the corresponding flat plate loaded with the same liquid. Hence, we can use relations (76), (85) - (88), and (92) for estimation of $\langle\sigma_{rad}\rangle$. For the case of liquid loading, however, the plate analogy remains approximately valid well below the frequency c_ℓ/a. As discussed in Section 2.2.3, for the frequency range of usual interest, the membrane effects are almost totally suppressed by the fluid loading, and the resonance loci in the wavenumber plane become more or less circular. Thus, for a liquid-filled cylinder, membrane effects fail to give rise to any AF modes.

An Orthotropic Cylinder Above Its Ring Frequency. - For an orthotropic cylinder, above the ring frequency ω_r [defined by relation (69)], the same kind of plate analogy exists with the corresponding orthotropic plate. Thus relations (89) - (91) are equally valid for the cylinder. Below the higher critical frequency, the average radiation efficiency $\langle\sigma_{rad}\rangle$ must once again be evaluated by a computer; however, in this case, the contribution to the radiation efficiency from the corner modes as well as axial strip modes is neglected.

Density of AF Modes Below the Ring Frequency of An Orthotropic Cylinder. - Below the ring frequency $\omega_r = c_3/a$, the membrane stresses induced by the curvature of the cylinder increase the potential energy of vibration and, hence, also the frequency and the phase velocity of free vibration at a particular wavenumber (see Sections 2.2.1 and 2.2.2). In terms of the geometry of the resonance loci in the wavenumber plane, the resonance loci in the "membrane region" of the wavenumber plane are radial straight lines (Fig.17). Therefore, below the ring frequency, there will always be some acoustically fast modes -- that is, resonant modes with wavenumber magnitude less than the acoustic wavenumber k_a at the same (resonance) frequency.

For most cases of interest, the acoustical critical frequencies ω_{c1} and ω_{c3} are considerably higher than the ring frequency ω_r. With such a situation, for frequencies below the ring frequency, the acoustic wavenumber locus $k_a = \omega/c$ will intersect the resonance locus only in the membrane region of the wavenumber plane. Figure 23(a) shows the acoustic wavenumber locus and the resonance locus in the dimensionless wavenumber plane (r_m, θ_m) for such a case. The resonance locus is approximately given (see Section 2.2.2) by

$$\nu_3{}^2 = \cos^4\theta_m . \qquad (93)$$

Owing to the transformation of the coordinates, the acoustic wavenumber locus becomes an ellipse:

$$r_m{}^2[(\cos^2\theta_m/\alpha_1) + (\sin^2\theta_m/\alpha_3)] = (c_3\nu_3/c)^2 . \qquad (94)$$

The coordinates of the point of intersection P in Fig. 23(a) can be easily obtained by solving relations (93) and (94) simultaneously. Along straight line OP, then, lie the AF modes resonating at the dimensionless frequency ν_3. The boundary in the (r_m,θ_m) plane, which encloses the region of all such AF modes below the ring frequency (that is, $0 \leqslant \nu_3 \leqslant 1$), is shown by the solid curve in Fig. 23(b). This is the locus of point P as ν_3 varies between 0 and 1. To simplify the calculations, this region of AF modes is approximated by an outer bound; this is the locus of the approximate point of intersection P' obtained by neglecting the term $(\sin^2\theta_m)/\alpha_3$ in relation (94). This approximation is not too unreasonable for $0 \leqslant \theta_m \leqslant \pi/4$, the region in which most (roughly 80%) of the AF modes lie. The approximate locus is a circle:

$$r_m = (c_3\alpha_1{}^{1/2}/c) \cos\theta_m \quad . \qquad (95)$$

The number $N_{AF}(\omega)$ of AF modes resonating below frequency ω is then approximately given by the ratio of the shaded area in Fig. 23(b) to the area attributed to a pair of modes situated at the same location in the (r_m,θ_m) plane.

$$N_{AF}(\omega) = (\ell_1/2\pi a)(c_3/c)^2(\alpha_1/\alpha_3)^{1/2} \tag{96}$$

$$[\pi/2 - \cos^{-1}(\nu_3^{1/2}) - \{\nu_3(1 - \nu_3)\}^{1/2}] .$$

Here, ℓ_1 and a are the axial length and the radius of the cylinder, and the rest of the symbols are defined in Section 2.2.2.

The density $n_{AF}(\omega)$ of the acoustically fast modes below the ring frequency, based on a narrow frequency band, is then given by

$$n_{AF}(\omega) = [N_{AF}(\omega_2) - N_{AF}(\omega_1)]/(\omega_2 - \omega_1) \quad . \tag{97}$$

Here, ω_2 and ω_1 are the upper and lower frequencies of the band. In finding the difference between the cumulative modal counts, most of the error introduced in the range $\pi/4 \leqslant \theta_m \leqslant \pi/2$ due to the approximation of the locus of point P is removed. The resulting estimate for the modal density of the AF modes below the ring frequency is found to agree very well with the more detailed calculations [33].

Radiation Resistance of An Orthotropic Cylinder Below Its Ring Frequency. - Continuing with the orthotropic cylinder, at any frequency below the ring frequency, most of the AS modes are of the edge-1 type with negligible radiation efficiency. Therefore, an approximate estimate of the average radiation efficiency for an orthotropic cylinder below its ring frequency is given by

$$<\sigma_{rad}> = n_{AF}(\omega)/n(\omega) \quad , \tag{98}$$

where the modal densities $n_{AF}(\omega)$ and $n(\omega)$ are given by relations (97) and (74). Specialization of these results for an isotropic cylinder is straight forward.

The Average Radiation Loss Factor. - Finally, the average radiation loss factor $<\eta_{rad}(\omega)>$ at any frequency ω is defined by

$$<\eta_{rad}(\omega)> = R_{rad}/\omega M = \rho c A <\sigma_{rad}>/\omega M \quad . \tag{99}$$

Here ρc is the characeristic acoustic impedance of the acoustic medium, A is the surface area of the structure, and M is the typical modal mass for the modes resonating near frequency ω.

SECTION 3

STRUCTURAL VIBRATION INDUCED BY THE ACOUSTIC AND AERODYNAMIC ENVIRONMENTS

3.1 Introduction

In this section, we obtain quantitative estimates for the vibration levels set up in the structural elements studied in Section 2, when exposed to one or more of the environments studied in Section 1. Most of the discussion in this section is restricted to resonant vibration. As pointed out before, if there are enough resonant modes in any frequency band of interest, and if the dissipation losses (which may be due to internal damping in the structure material, losses at the structural joints, and losses due to the power flow into the surrounding medium and the neighboring structural elements) are small compared with the total energy of vibration, the resonant response will dominate the forced response.

Also, structural or modal vibration at resonance is controlled by resistive or dissipative mechanisms associated with the vibration. Since the exciting force and response velocity are in phase for resonant vibration, such vibration is accompanied by real power input from the environment into the structure. The vibration attains a steady state when the power input from the exciting force is equal to the power dissipated in the resistive force. This description provides us with a simple way of estimating structural response. We first calculate and sum up the power input to resonant modes in different frequency bands and then obtain the velocity response for the whole structure by equating the dissipated power and the input power in different frequency bands.

Now, in some instances, a fraction of the resonant modes in a frequency band would find the best possible "spatial match" or "coincidence" with the excitation field from the environment.

The power input from the excitation field to these coincident and resonant modes would dominate the power input to the rest of the resonant modes. For example, in Fig. 22(c) where the locus of modes resonating between two critical frequencies for an orthotropic plate are shown the acoustically critical modes in a small segment of the resonance locus about the intersection point P find the maximal coincidence with the acoustic field. However, owing to the fluid-loading effects and the fact that the strength of the acoustic excitation for the remaining AF modes does not drop too sharply, the power input to the acoustically critical modes does not dominate the power input to the rest of the resonant modes. The situation, as we shall see, changes somewhat for the excitation from a turbulent boundary layer (TBL).

3.2 Excitation from a Turbulent Boundary Layer

3.2.1 Introduction. - Consider a fully developed, spatially homogeneous turbulent boundary layer over an isotropic cylinder. We assume that the associated pressure fluctuations are convected along the generators of the cylinder at a constant speed U_c. A sufficiently valid and compact description of the statistical properties of these pressure fluctuations is given by the combined wavenumber and frequency spectrum $\Phi_p(\underline{k},\omega)$ [relation (22)]. At any frequency ω, most of the excitation from the TBL is concentrated in a narrow strip in the wavenumber plane (k_1,k_3). The width of this strip in the k_3 direction depends on the eddy decay time or the temporal spectrum $\Phi_m(\omega)$. As shown in Fig. 24, this "excitation strip" divides the wavenumber plane into regions of hydrodynamically fast (HF), hydrodynamically critical (HC), and hydrodynamically slow (HS) modes. These modes are determined by whether the trace in the axial direction of the phase velocity of vibration at frequency ω for a particular mode is higher than, equal to, or less than the convection velocity U_c.

The frequency range is divided by two critical frequencies, the ring frequency ω_r and the hydrodynamic critical frequency ω_h. The latter is given by

$$\omega_h = U_c^2/\kappa c_\ell \quad . \tag{100}$$

Almost invariably, the hydrodynamic critical frequency is higher than the ring frequency for structures of current interest. For $\omega < \omega_h$, the strip of excitation in the wavenumber plane (shown in Fig. 24) intersects the resonance locus; for $\omega > \omega_h$ it does not. For $\omega > \omega_r$, the bending stresses are dominant and the cylinder behaves like a flat plate; for $\omega < \omega_r$, the membrane stresses also become important. Finally, in the wavenumber plane (k_1, k_3), the resonance locus at any frequency ω determines the regions of the nonresonant, mass-controlled and stiffness-controlled modes and the resonant, resistance-controlled modes. The situations arising in the different frequency ranges, and the classification of modes in the wavenumber plane, are shown in Fog. 24. Note that, below the ring frequency ω_r, the HC resonant modes are obtained in the "membrane region" as well as the "bending region" of the wavenumber plane. Only the former of these is shown in Fig. 24(b).

Since, in the wavenumber plane, the domain of excitation at any frequency is quite narrow and sharply defined, the HC modes find by far the best spatial match or coincidence with the excitation field. The excitation of the HS and HF modes arises from relatively secondary effects. The first of these effects is due to the extension of the excitation field beyond the narrow strip defining the coincident region in the wavenumber plane. These "tails" of the excitation field [see the variation of $\Phi_p(\underline{k},\omega)$ in Fig. 24(a)] are clearly governed by the temporal fluctuations [that is, the spectrum $\Phi_m(\omega)$] of the pressure field in the TBL, discussed in Section 1. The second effect is due to the finite extent of any real structure. If the structure has many edges and discontinuities (i.e., a small mean free path), the edge effects will contribute to some coupling with the excitation field. The situation in some sense will be analogous to that for the acoustically slow modes B, C, D, and E, in Fig. 21. On the average, coupling due to edge effects will be higher for the HS modes than for the HF modes. The excitation of HF and HS modes from these secondary effects is, in general, found to be quite small compared with the excitation of HC modes. Thus, most of the multimodal resonant response is the result of power flow from the TBL pressure field into HC resonant modes. This can easily be found from an analysis of a corresponding structure of infinite extent [38].

In estimating the structural excitation from the TBL pressure field, we have disregarded the detailed variation of the associated radiation resistance. (This will be important chiefly for resulting sound radiation.) In this respect, note that, if the convection velocity U_c is subsonic, all the HC resonant modes will be acoustically slow [see Figs. 24(a) and 24(b)]. For supersonic convection velocities, the HC resonant modes which are also acoustically fast will lie only in the frequency rante $\omega_h < \omega < \omega_c$, where ω_h and ω_c are the hydrodynamic and the acoustic critical frequencies.

The above qualitative description and the response estimates that follow are valid for any fluctuating pressure field that has similar convective and decaying properties. As we saw in Section 1, the fluctuating pressure fields associated with the conditions of separated flow or wake impingement can be described approximately by such properties. Therefore, the estimates of structural response for these types of excitation can easily be found from the formulas developed below for the TBL excitation.

3.2.2 Response of an Isotropic Cylinder or Flat Plate of Infinite Extent to a TBL Pressure Field.

- The location of the HC resonant wavenumbers in the dimensionless wavenumber plane (r,θ) [see Section 2.2.1] is clearly given by the intersection of the resonance locus [relation (37)] with the center line of the excitation strip. The latter is represented by

$$\omega = k_1 U_c \tag{101}$$

or

$$\nu = r\,\lambda\,\cos\theta \;, \tag{102}$$

where

$$\lambda = (U_c/c_\ell)(a/\kappa)^{1/2} \tag{103}$$

Thus the locus of the HC resonant wavenumber is given by

$$r^2\lambda^2\cos^2\theta = r^4 + \cos^4\theta \;. \tag{104}$$

The two "concidence loci" that are valid, respectively, in the "bending region" and the "membrane region" of the (r,θ) plane are obtained approximately by ignoring one or the other of the two terms on the right-hand side of relation (104). The resulting coincidence loci are circles:

$$r = \lambda \cos\theta \tag{105}$$

for the bending or the flat plate behavior; and

$$r = \cos\theta/\lambda \tag{106}$$

for the membrane behavior.

These simple approximations for the coincidence loci, of course, hold only for the case when the dimensionless parameter $\lambda > 1$. This covers a surprisingly large number of situations in launch-vehicle response estimation. Figures 25 and 26 show the two coincidence loci and the corresponding resonance loci in the wavenumber plane (k_1, k_3). The subscripts p and c are introduced to indicate that, in Fig. 25, the magnitude k_p of the HC resonant wavenumber is determined by the condition of resonance and its direction θ_c is determined by the condition of coincidence; whereas, in Fig. 26, the direction θ_p is determined by resonance, and the magnitude k_c by coincidence.

Note that, in the present analysis for infinitely extended structures, the wavenumber components k_1, k_3 and the frequency ω have the full range of $-\infty$ to $+\infty$. Thus, for negative frequencies ω, there will be similar coincidence loci in the lower half of the wavenumber plane. Also note that, although the circumference of a cylinder is always finite and the resulting wavenumbers k_3 always discrete, we shall assume k_3 to vary continuously. This essentially amounts to replacing every summation over the variable k_3 by the corresponding integral, and does not greatly influence the response estimates.

The radial velocity field $v(\underline{x},t)$ on the cylinder surface is related to the exciting pressure field by the relation,

$$v(\underline{x},t) = \iiint p(\underline{x}',t')\ h(\underline{x} - \underline{x}',t - t')\ dx'\ dt' \ . \qquad (107)$$

Here, $h(\underline{x},t)$ is the Green's function, or the Fourier transform, of $H(\underline{k},\omega)$ [relation (28)]. Multiplying each side of relation (107) by $-p(\underline{x},t)$ gives $\Pi(\underline{x},t)$, the instantaneous power input per unit area to the cylinder at time t and location $\underline{x}$. The combined wavenumber and frequency spectrum $\Phi_\pi(\underline{k},\omega)$ for this power input can easily be derived $\underline{40/}$:

$$\Phi_\pi(\underline{k},\omega) = H(\underline{k},\omega)\ \Phi_p(\underline{k},\omega) \ . \qquad (108)$$

Finally, the spectrum $\Pi(\omega)$ for power input per unit area at any frequency ω can be found by integrating relation (108) over the wavenumber variable $\underline{k}$. The integration over the singularity of the wave admittance $H(\underline{k},\omega)$ gives essentially the contribution from the resonant or free wavenumber. The integration over the singularity(or the peak) of the pressure spectrum $\Phi_p(\underline{k},\omega)$ further restricts the location of the chief contribution of the integral to be near the coincidence locus in the wavenumber space. Even though the real part of this power input is more or less independent of the magnitude of the dissipation, a suitably defined dissipation constant η must be introduced in $H(\underline{k},\omega)$ in the formal process of integration over the singularity. Thus the term ν^2 in relation (28) is replaced by the term $\nu^2(1+i\eta)$ $\underline{40/}$.

The power input to the cylinder per unit area thus obtained consists of two parts, $\Pi_b(\omega)$ and $\Pi_m(\omega)$, corresponding, to the coincidence loci in the"bending region" and the "membrane region", respectively, of the wavenumber plane. The final expressions for these are

$$\Pi_b(\omega) = (\pi p_h{}^2/\rho_s U_c)\Phi_f(\omega)\Phi_3(k_p \sin\theta_c)/\sin(2\theta_c)$$

$$\text{for } \omega \leqslant \omega_h \ , \tag{109}$$

$$\Pi_m(\omega) = (\pi p_h{}^2/\rho_s U_c)\Phi_f(\omega)\Phi_3(k_c \sin\theta_p)/\sin(2\theta_p)$$

$$\text{for } \omega \leqslant \omega_r \ . \tag{110}$$

Here, (k_p,θ_c) or (k_c,θ_p) is the appropriate HC resonant wavenumber at frequency ω. The rest of the nomenclature is that of Sections 1 and 2. The total power input per unit area is then given by

$$\Pi(\omega) = \Pi_b(\omega) + \Pi_m(\omega) \qquad \text{for } \omega \leqslant \omega_r \tag{111}$$

$$= \Pi_b(\omega) \qquad \text{for } \omega_r < \omega \leqslant \omega_h \ . \tag{112}$$

We can use the same procedure for obtaining an expression for power input for resonant vibration above the hydrodynamic critical frequency ω_h [Fig. 24(c)]. The controlling process in this regime will be the temporal fluctuations of the exciting pressure field [40]. For the situations of interest in launch-vehicle dynamics, this aspect of the problem is found to be unimportant as compared with that of the hydrodynamic coincidence.

For resonant vibration, the power input from the excitation is equal to the power dissipated. Equating the two, one obtains the velocity spectrum $V(\omega)$, where

$$V(\omega) = \Pi(\omega)/\rho_s \eta_s \omega \quad . \tag{113}$$

Here, η_s is the total cylinder-loss factor. The acceleration spectrum $A(\omega)$ is related to the velocity spectrum by the relation

$$A(\omega) = \omega^2 V(\omega) \quad . \tag{114}$$

A rough estimate of the maximum stress level at the surface of the cylinder is obtained: (a) by assuming a linear variation of stress, over the thickness h of the cylinder, for flexural vibration controlled by the bending stresses; (b) and by assuming a constant value of stress over h for in-plane or longitudinal vibration controlled by the membrane stresses. Balancing the potential and kinetic energies for the resonant vibration, the stress-level spectrum $S(\omega)$ is then related to the velocity spectrum [46] by

$$S_m(\omega) = 4 \; c_\ell^2 \; \rho_m^2 \; V_m(\omega) \; , \tag{115}$$

$$S_b(\omega) = 12 \; c_\ell^2 \; \rho_m^2 \; V_b(\omega) \quad . \tag{116}$$

Here, as usual, the subscripts b and m refer to the components of the velocity and the stress spectra controlled by the bending or the membrane stresses. The density for the cylinder material is ρ_m. The above estimates ignore any stress concentrations due to the presence of the boundaries or the occurrence of "hot spots."

All the results and the related discussion in this subsection hold also for an isotropic flat plate, except that in this case the membrane stresses(and all the quantities with subscript m) are to be ignored.

Note that all the spectra [relations (109) to (116)] here are two-sided, with the range of frequency ω from $-\infty$ to $+\infty$. Assuming that all the quantities above are in units of feet, pounds (weight), and seconds, their conversion to third-octave-band levels on the Hertz frequency basis is performed as follows:

$$\text{SPL dB } \underline{\text{re}} \text{ } 0.0002 \text{ } \mu\text{bar} = 132 + 10 \log f + 10 \log \langle p_h{}^2 \Phi_f(\omega) \rangle , \quad (117)$$

$$\text{PWL dB } \underline{\text{re}} \text{ } 10^{-12}\text{W} = 126 + 10 \log f + 10 \log \langle \Pi(\omega) \rangle , \quad (118)$$

$$\text{VL dB } \underline{\text{re}} \text{ 1 cm/sec} = 34 + 10 \log f + 10 \log \langle V(\omega) \rangle , \quad (119)$$

$$\text{AL dB } \underline{\text{re}} \text{ 1 g} = -25.5 + 10 \log f + 10 \log \langle A(\omega) \rangle , \quad (120)$$

$$\text{SL dB } \underline{\text{re}} \text{ Young's modulus E} = 4.5 + 10 \log f + 10 \log \langle S(\omega)/E^2 \rangle \text{ .} \quad (121)$$

Here, SPL is the excitation pressure level, PWL the power input level, VL the velocity level, AL the acceleration level, and SL the stress level in a third-octave band around frequency f Hz. These levels are in decibels, with respect to the standard units specified above. The brackets around the corresponding two-sided spectrum on the right-hand side of each relation indicates the average value of this spectrum over a third-octave band (in radian frequency) centered around the frequency $\omega = 2\pi f$. In this connection, note that the singularities in relations (109) and (110) at their respective critical frequencies ω_h and ω_r integrate out by the process of averaging over frequency bands.

3.2.3 Response of an Orthotropic Cylinder or Flat Plate of Infinite Extent to a TBL Pressure Field.

- The coincidence loci in this case are determined by the intersection point in the wavenumber plane of the "excitation locus" [relation(101)] and the resonance locus [relation(68)]. The two coincidence loci, which are controlled by the bending or the membrane behavior of the cylinder, are best described in their respective dimensionless wavenumber planes, the (r_b, θ_b) plane or the (r_m, θ_m) plane. The coincidence loci are:

$$r_b = \lambda_b \cos\theta_b$$

$$\lambda_b = (U_c/c_\ell)(a/\kappa_1)^{1/2} \qquad (122)$$

for the bending behavior,

$$r_m = \cos\theta_m/\lambda_m$$

$$\lambda_m = U_c/c_3\alpha_1^{1/2} \qquad (123)$$

for the membrane behavior.

The procedure for determining the two components, $\Pi_m(\omega)$ and $\Pi_b(\omega)$, of the power input per unit area is exactly the same as for the isotropic case, except that in this case the integration of relation (108) over the wavenumber variables is performed in the dimensionless wavenumber plane appropriate to the power input component. The final results are:

$$\Pi_b(\omega) = (\pi\, p_h^2/\rho_s U_c)(\kappa_1/\kappa_3)^{1/2}\Phi_f(\omega)\Phi_3[r_{bp}\sin(\theta_{bc})/(a\kappa_3)^{1/2}]/\sin(2\theta_{bc})$$

$$\text{for } \omega \ll \omega_h, \tag{124}$$

$$\Pi_m(\omega) = (\pi\, p_h^2/\rho_s U_c)(\alpha_1/\alpha_3)^{1/2}\Phi_f(\omega)\Phi_3[r_{mc}\sin(\theta_{mp})/a\alpha_3^{1/2}]/\sin(2\theta_{mp})$$

$$\text{for } \omega \ll \omega_r, \tag{125}$$

$$\omega_h = U_c^2/\kappa_1 c_\ell\ , \tag{126}$$

$$\omega_r = c_3/a\ . \tag{127}$$

Here, (r_{bp},θ_{bc}) and (r_{mc},θ_{mp}) are the appropriate dimensionless HC resonant wavenumbers. The subscript b or m refers to the bending or the membrane region of the wavenumber plane. The interpretation for the subscripts p and c is the same as in the remarks after relation (106) and in Figs. 25 and 26.

Relations (111) to (121) and the related discussion for the isotropic structure in Section 3.2.2 apply equally well for the orthotropic structure.

3.2.4 Response of an Isotropic, Liquid-Loaded Cylinder or Flat Plate of Infinite Extent to a TBL Pressure Field. - As discussed in section 2.2.3, for most situations of interest, the presence of a liquid inside an infinitely long cylinder has essentially a mass-loading effect. For a finite structure, the liquid tends to couple the modes due to the edge effects. Our justification for ignoring this complication has been this: The simple analysis presented below for an infinite cylinder shows that the mass-loading effect of the liquid alone is responsible for reducing the vibration levels (from the corresponding levels for the empty cylinder) by roughly 5 to 7 dB. Any refinement in the analysis to account for the modal coupling and other edge effects would thus be a refinement in the estimate of response levels which are, in any case, less critical than those for the corresponding empty structure.

The development of the analysis for the simplified case of the infinitely long, fluid-loaded cylinder proceeds along the lines of the previous two subsections. The coincidence loci in the dimensionless wavenumber plane (r,θ) are determined by the intersection of the "excitation locus" [relations (102), (103)] and the resonance locus [relation (55)]. Therefore, the loci are given approximately by

$$r = [\lambda^2(1 + \beta/r)]^{1/2} \cos\theta \quad \text{for the bending behavior i.e. } r^4 \gg \cos^4\theta \, , \qquad (128)$$

and

$$r = [\lambda^2(1 + \beta/r)]^{-1/2} \cos\theta \quad \text{for the membrane behavior i.e. } \cos^4\theta \gg r^4 \, , \qquad (129)$$

where λ is the dimensionless variable given by relation (103).

The coincidence loci are no longer circles. Note that the largest frequency ω_f for which coincidence is possible in the membrane region of the (r,θ) plane is no longer the same as the ring frequency $\omega_r = c_\ell/a$. To estimate ω_f, we assume that $\beta/r \gg 1$, since, for vibration at relatively low frequencies, the associated wavenumber r is also generally small. This assumption amounts to ignoring the mass loading due to the cylinder material, since it is negligible in comparison with the mass loading due to fluid in the cylinder. Under this simplification, relations (102) and (129) immediately yield

$$\omega_f = (c_\ell/a)^2\rho_s/\rho_o U_c \ . \tag{130}$$

For an aluminum cylinder 33 ft in diameter and 180 mil thick, filled with liquid oxygen, and for a convection velocity U_c of 1000 ft/sec, ω_f works out to be 35 rad/sec, or roughly 6 H_z, a very low frequency indeed. Thus, for most situations and frequency ranges of interest, a liquid-filled cylinder responds like a liquid-loaded plate. The discussion here supplements the discussions in connection with Fig. 19 and relations (55) and (76).

Simpler formulas for the coincidence loci and the hydrodynamic critical frequency ω_h can be obtained similarly by approximations described in connection with relation (76).

The power input formulas are approximately given by

$$\Pi_b(\omega) = [\pi\, p_h{}^2/(\rho_s+\rho_o/k_p)U_c]\Phi_f(\omega)\Phi_3(k_p\sin\theta_c)/\sin(2\theta_c) \qquad \text{for } \omega \leqslant \omega_h, \tag{131}$$

$$\Pi_m(\omega) = [\pi\, p_h{}^2/(\rho_s+\rho_o/k_c)U_c]\Phi_f(\omega)\Phi_3(k_c\sin\theta_p)/\sin(2\theta_p) \qquad \text{for } \omega \leqslant \omega_f. \tag{132}$$

Here, (k_p,θ_c) or (k_c,θ_p) is once again the HC resonant wavenumber. In addition to all the implicit effects of the liquid loading, such as changes in the resonance frequencies and the suppression of the membrane effects, the additional mass-loading effect of the fluid is seen to appear explicitly in the term ρ_o/k_p or ρ_o/k_c.

The remaining spectra (for velocity, acceleration, or stress level) can be related to the power input spectrum by the relations given in Section 3.2.2. In connection with relation (113), note that the quantity $\rho_s\eta_s$ will still have the same numerical value, since (at least in the formal analysis) no power was assumed to be dissipated in the liquid. Hence, if the surface mass density ρ_s in relation (113) is to be changed to the effective surface mass density $(\rho_s + \rho_o/k)$, the loss factor η_s must also be simultaneously changed to keep the product invariant.

3.2.5 Consideration of Forced Response. - With reference to Figs. 24(a) and 24(b), note that the strength of the wavenumber spectrum $\Phi_3(k_3)$ [see relation (25)], and, hence, of the exciting pressure spectrum $\Phi_p(\underline{k},\omega)$, decreases as the wavenumber k_3 increases. Therefore, the magnitude of the exciting forces for the HC mass-controlled modes in Fig. 24(a) and for the HC stiffness-controlled modes in Fig. 24(b) is higher than that for the corresponding HC resonant modes. The approximate response calculation for the forced vibration in these and other similar situations can be performed by taking the suitable asymptotic form (mass-controlled or stiffness-controlled) of the appropriate pressure-to-velocity wave admittance $H(\underline{k},\omega)$. Note that for forced vibration there is no significant power exchange between the structure and the exciting environment.

For an isotropic cylinder, the contributions $V_{mass}(\omega)$ and $V_{stiffness}(\omega)$ to the surface velocity spectrum owing to the forced vibration of HC mass-law-controlled modes in Fig. 24(a) and HC stiffness-controlled modes in Fig. 24(b), are approximately given by

$$V_{mass}(\omega) \approx p_h{}^2\Phi_f(\omega)/\rho_s{}^2\omega^2,$$

$$V_{stiffness}(\omega) \approx \nu^4 p_h{}^2\Phi_f(\omega)/\rho_s{}^2\omega^2 \;,$$

where $\nu = \omega a/c_\ell$ is the dimensionless frequency. Despite the higher magnitude of the exciting forces for this forced vibration, when the numerical values typical for launch-vehicle situations are substituted in the above estimates, the contribution to velocity response from the forced vibration is found to be 10 - 20 dB below the contribution from the resonant vibration. Therefore, as long as one is interested in vibration transmission and stress levels, one can safely ignore the consideration of forced or nonresonant response. For acoustic noise transmission problems, however, nonresonant response can play a significant role [43].

3.3 Excitation from a Diffuse Sound Field

3.3.1 Introduction. - Much of the detailed calculation involved in estimating the structural response to acoustic noise consists of calculating the modal density and the average radiation efficiency for the structure. This we have already accomplished in Section 2. Here, we describe a general procedure for estimating the structural response in terms of the modal density and the radiation efficiency. The method is applicable to an isotropic or orthotropic cylinder or plate, whether fluid-loaded or not.

Note that, for the case of structural excitation from a turbulent boundary-layer pressure field, for frequencies below the hydrodynamic critical frequency ω_h, there was always some resonant vibration pattern on the structure which found a perfect "spatial match" or coincidence with the excitation field. This was essentially a "surface" interaction, which generally dominates over the "edge" interaction, and which can easily be estimated from the corresponding infinite or "edgeless" structure. For the present case of structural excitation from acoustic noise, in a significant frequency range of interest between the ring frequency ω_r and the acoustic critical frequency ω_c, no such "surface" interaction for resonant vibration is possible. Any interaction and response in this frequency range must arise from the effects due to the boundaries and discontinuities on the structure surface. The analysis on the corresponding infinite or "edgeless" structure would give an estimate of zero response in this frequency range.

In the following, we analyze a finite structure with well-defined boundaries. Our approach is to calculate the response of a single mode to a reverberant sound field and then extend the concepts to include groups of structural modes resonating in different frequency bands.

3.3.2 Structural Response to a Diffuse Sound Field. - If a structural mode is excited by noise, it loses energy by internal dissipation and by sound radiation. We subdivide the total power lost Π_s accordingly,

$$\Pi_s = \Pi_{diss} + \Pi_{rad} , \tag{133}$$

$$\Pi_s = \omega\eta_s E_s \tag{134}$$

$$E_s = M \langle v_s^2 \rangle \quad . \tag{135}$$

Here, E_s is the modal energy at resonance, $\langle v_s^2 \rangle$ is the mean-squared modal velocity, M is the modal mass, ω is the natural frequency for the mode, and η_s is the total loss factor for the mode. Consequently, η_{diss}, defined by

$$\Pi_{diss} = \omega \eta_{diss} E_s, \tag{136}$$

is a measure of the internal losses, and η_{rad}, defined by

$$\Pi_{rad} = \omega \eta_{rad} E_s, \tag{137}$$

is a measure of the radiation losses or of the modal coupling to the sound field. Clearly,

$$\eta_s = \eta_{diss} + \eta_{rad} \quad . \tag{138}$$

Previous studies have established that, when the "acoustic modes" in a diffuse sound field are directly excited by external sources and the structural modes are excited by interaction with the sound field, the structural energy will be [35, 42]

$$E_s = E_a \, \eta_{rad}/\eta_s \quad . \tag{139}$$

Here, E_a is the acoustic modal energy, which can be expressed in terms of the mean-squared pressure $\langle p_a^2 \rangle$ of the acoustic mode, the volume V of the space in which the diffuse sound field is contained (this cancels out later), the characteristic acoustic impedance ρc, and the sound speed c [32]:

$$E_a = \langle p_a^2 \rangle \, V/\rho c^2 \quad . \tag{140}$$

Since the sound field is diffuse, we have

$$\Phi_p(\omega) = \langle p_a^2 \rangle \, n_a(\omega), \tag{141}$$

where $n_a(\omega)$ is the acoustic modal density and $\Phi_p(\omega)$ is the power density spectrum for the free-field acoustic pressure. Note that the spectrum is "single-sided," -- that is, the range of the radian frequency variable ω is from zero to infinity. The modal density $n_a(\omega)$ is given by [30]

$$n_a(\omega) = \omega^2 V/2\pi^2 c^3 \quad . \tag{142}$$

We assume the surface of the structure to be large enough so that the spectrum $\Phi_{p_{meas}}(\omega)$ of the pressure measured at the structure surface (which is also the "blocked" pressure) is approximately given by

$$\Phi_{p_{meas}}(\omega) = 2\Phi_p(\omega) \quad . \tag{143}$$

Therefore,

$$E_a = \pi^2 c\ \Phi_{p_{meas}}(\omega)/\rho\omega^2\ . \tag{144}$$

The single-mode response is then given by

$$\langle v_s{}^2\rangle = E_a\eta_{rad}/M\eta_s\ . \tag{145}$$

The total resonant-velocity response for the structure is obtained as the sum of the response for the resonant modes:

$$V(\omega) = (E_a/M)n_s(\omega)\mu(\omega)\ . \tag{146}$$

Here, $V(\omega)$ is the velocity spectrum $(0 < \omega < \infty)$, $n_s(\omega)$ is the modal density for the structure, and $\mu(\omega)$ is η_{rad}/η_s averaged over the resonant modes. For the numerical values of interest, the following approximation is generally found to be quite valid:

$$\mu(\omega) \approx \langle\eta_{rad}\rangle/(\langle\eta_{rad}\rangle + \eta_{diss})\ . \tag{147}$$

Here, $\langle\eta_{rad}\rangle$ is the modal radiation loss factor η_{rad} averaged over the resonant modes. The procedures for calculating $n_s(\omega)$ and $\langle\eta_{rad}\rangle$ were discussed in Section 2. From relations (144), (146), and (147), we finally get

$$V(\omega) = \pi^2 c\ \mu(\omega) n_s(\omega) \Phi_{p_{meas}}(\omega)/\rho M\omega^2 \ . \tag{148}$$

The spectra for the power input, the acceleration response, and the stress level can be related to the velocity spectrum $V(\omega)$ by relations (113) - (116). For the present case, all the spectra are defined for the positive radian frequencies only; therefore, for conversion to third-octave bands, 3 dB should be subtracted from the right-hand sides of relations (117) - (121). The measured SPL, and the surface acceleration AL would be given by

$$\text{SPL dB } \underline{\text{re}}\ 0.0002\ \mu\text{bar} = 129 + 10\ \log f + 10\ \log \langle \Phi_{p_{meas}}(\omega) \rangle \tag{149}$$

and

$$\text{AL dB } \underline{\text{re}}\ 1\ g = -28.5 + \log f + 10\ \log \langle A(\omega) \rangle \ . \tag{150}$$

The above procedure for the estimation of response to acoustic noise is valid for any of the structural elements described in Section 2. Note that, if the structure is loaded by a liquid, the modal mass M is to be interpreted everywhere as the total modal mass M_f[relation (66)], which includes the mass-loading effect due to the liquid also. If the internal dissipation loss factor η_{diss} is based on the structural mass only, the effective total loss factor is given by

$$\eta_s = \eta_{rad} + \eta_{diss} M/M_f \ , \tag{151}$$

where M is the structural mass or the "unloaded" modal mass.

3.4 Excitation by an Oscillating Shock Front

3.4.1 Introduction. - As we saw in Section 1, the fluctuating pressure field associated with an oscillating shock cannot be spatially homogeneous. Therefore, for analysis of structural response to oscillating shock, it is necessary to consider the modal approach for a finite structure. If the shock front over the structure undergoes a random oscillatory motion, the portion of the structure near the mean shock position will experience a fluctuating pressure field. Consequently, energy will flow from the environment into the structure in this localized region, and the resulting vibration will be transmitted to the other parts of the structure. In the following, we characterize the exciting environment in quantitative terms and develop procedures for estimating response of an isotropic or orthotropic flat plate or cylinder.

3.4.2 Response of a Cylinder to an Oscillating Shock Front. - Consider a cylinder of axial length ℓ_1 and circumference $\ell_3 = 2\pi a$. We assume that the shock front moves in the axial direction x_1 and that the mean position of the shock front is along the circumferential section midway between the two ends. We also assume that the shock front is always "perfectly coherent" in the circumferential direction -- that is, the displacement y(t) of the shock front from its mean position is always the same along the circumference of the cylinder. The associated pressure field is assumed to be

$$\begin{aligned} p(\underline{x},t) &= 0 \quad \text{for } -\ell_1/2 < x_1 < y(t) \\ &= \Delta p \quad \text{for } y(t) < x_1 < \ell_1/2 \quad . \end{aligned} \tag{152}$$

The situation is illustrated in Fig. 27.

We assume the displacement $y(t)$ to be a narrow-band random Gaussian process with zero mean, center-band frequency ω_{osc}, and root-mean-square value σ. Statistical properties for such a random process are well known [44, 45]. In particular, the correlation $\phi_y(t)$ for this process is given by

$$\phi_y(t) = \langle y(t')y(t' + t)\rangle_{t'}$$

$$= \sigma^2 e^{-\alpha t}[(\alpha/\beta) \sin\beta t + \cos\beta t)] \qquad (153)$$

$$\beta^2 = \omega_{osc}{}^2 - \alpha^2 \quad . \qquad (154)$$

Here, 2α is the bandwidth of the process $y(t)$.

The modal force $F_{mn}(t)$ exciting the mode (m,n) of the cylinder can be obtained by substituting relation (152) for the pressure field $p(\underline{x},t)$ in relation (60). The modal shapes $\psi_{mn}(\underline{x})$ and the normalizing constants for the cylinder are given by relations (57) and (58). Owing to the circumferential symmetry, $F_{mn}(t) = 0$ for nonzero n. For $n = 0$, the correlation $R_m(t)$ of the fluctuating part of $F_m(t)$ [short for $F_{m0}(t)$] can be related to the correlation $\phi_y(t)$ of $y(t)$ as follows:

$$R_m(t) = G^2 \sinh[\phi_y(t)m^2\pi^2/\ell_1{}^2] \qquad \text{for m odd}$$

$$= G^2[\cosh\{\phi_y(t)m^2\pi^2/\ell_1{}^2\}-1] \quad \text{for m even,}$$

$$G^2 = 2(\Delta_p \ell_1 \ell_3/m\pi)^2 \exp\,[-(m\pi\sigma/\ell_1)^2] \ . \qquad (155)$$

Generally, the shock oscillation frequency is found to be low (80 Hz or lower). In that case, only the lowest-order modes (i.e., $m = 1, 2, 3$, etc.) with resonance frequencies in a similar low range contribute significantly to the response. For such low-order modes, we can reasonably assume that the root-mean-square shock displacement is smaller than the modal wavelength in the axial direction, that is, $m\sigma/\ell_1 < 1$. Under this assumption, the frequency composition of the corresponding modal forces can be described simply. The spectrum $S_m(\omega)$ for a modal force [which is the Fourier transform of $R_m(t)$] in that case is given approximately by

$$S_m(\omega) = \langle F_m^2 \rangle S_{odd}(\omega)/\omega_{osc} \qquad \text{for m odd}$$

$$= \langle F_m^2 \rangle S_{even}(\omega)/\omega_{osc} \qquad \text{for m even}$$

$$\langle F_m^2 \rangle = R_m(0) \tag{156}$$

The normalized and dimensionless spectra $S_{odd}(\omega)$ and $S_{even}(\omega)$ for $2\alpha/\omega_{osc} = 0.2$ are shown in Fig. 28. $S_{odd}(\omega)$ also represents the normalized and dimensionless spectrum for the process $y(t)$. $S_{odd}(\omega)$ peaks at ω_{osc}, whereas $S_{even}(\omega)$ peaks at $2\omega_{osc}$. From a physical point of view, an odd-numbered mode is excited by a force with a dominant frequency of ω_{osc}, and an even-numbered mode is excited by a moment with a dominant frequency of $2\omega_{osc}$ 47/.

Note that the spectrum given by relation (14) pertains to the levels of fluctuating pressure due to the random motion of the shock front. The dashed spectrum shown in Fig. 7 is based on relation (14) and pertains to the maximum value for these fluctuating pressure levels, which is measured at the mean location of the shock front ($\overline{t}_i = \overline{t}_k$). Relation (14) is derived in Ref. 20 on the assumption of Poisson statistics for the motion of the shock front. This assumption does not emphasize the oscillatory nature of the shock-front motion. In contrast, $S_m(\omega)$ given by relation (156) represents the spectrum for the modal forces. This is based on the assumption that the displacement of the shock front is represented by Gaussian statistics and has a dominant oscillatory behavior. The two alternate mathematical models are ideally suited to the nature and the goal of the two distinct analyses. Each model provides an approximate but adequate representation of the physical situation.

The procedures for determining the masses and the resonance frequencies for the "modal oscillators" for an isotropic or orthotropic cylinder have already been discussed in Section 2. The resonant velocity response $v_m(t)$ for the modal oscillator corresponding to mode (m,0) can be estimated by assuming the spectrum for the corresponding modal force to be "smooth" compared with the modal admittance function. The mean-squared velocity response for mode is then given by

$$\langle v_m^2(t)\rangle = \pi S_m(\omega_m)/M_m^2\ \omega_m\ \eta_m\ . \qquad (157)$$

Here, M_m is the modal mass, ω_m the natural frequency, and η_m the total loss factor for the modal oscillator (m,0). Note that the spectrum $S_m(\omega)$ is "two-sided." The total surface velocity spectrum for the structure in third-octave bands can be obtained simply by adding up the contributions $\langle v_m^2(t)\rangle$ from the modes with resonance frequencies in the same frequency bands. The remaining output spectra (for power input, acceleration, or stress level) can be related to the velocity spectrum by the relations given in Section 3.2.2.

Note that, since the shock oscillation frequency is quite low and since the excitation is quite sharply oscillatory, only the first few modes contribute most of the response. Therefore, it is wise in this case to abandon the statistical concept of modal density and to estimate the individual modal response for the first 5 or 10 modes.

Also note that, if the shock oscillation frequency is greater than one-half the fundamental frequency of the structure, some low-order modes will be excited at "coincidence and resonance." The resulting response in that case can be quite high.

3.4.3 Response of A Rectangular Plate to an Oscillating Shock Front.- Consider a flat rectangular plate of size (ℓ_1,ℓ_3). The geometry of the situation can be inferred from Fig.27,by interpreting the projected view of the cylinder in Fig. 27(a) as a flat plate of size (ℓ_1,ℓ_3).Thus the shock front once again is assumed to move in the x_1 direction, with its mean position at $x_1 = 0$. Furthermore, the shock front is assumed to be perfectly coherent over the width ℓ_3 of the plate. The associated pressure field $p(\underline{x},t)$ and the properties of the random shock displacement $y(t)$ are also assumed to be the same as in Section 3.4.2 [relations (152 - (154)].

The modal shapes $\psi_{mn}(\underline{x})$ and the normalizing constants c_{mn}, however, change [see relation (67)]. Owing to the assumed coherence of the shock front over the width ℓ_3 of the plate, only the modes with odd n (that is, n = 1, 3, 5...) are excited. For numerical values of interest, the modes with n greater than 1 have considerably higher resonance frequencies than the modes with n = 1. Furthermore, since the shock oscillation frequency is low (generally even lower than the fundamental resonance frequency for the structure), only n = 1 modes contribute significantly to the response.

The correlation $R_{mn}(t)$ of the fluctuating part of the modal force $F_{mn}(t)$ is still given by relation (155) for $R_m(t)$, except that the variable G^2(and, therefore, the mean-squared modal force) now decreases by a factor of $8/\pi^2 n^2$. Once again, for low-order modes ($n = 1$ and $m = 1, 2, 3, 4 \ldots .$), one can assume that $m\sigma/\ell_1 < 1$. Then the power density spectra for the modal forces are given by relation (156), with the mean-squared values $\langle F_{mn}^2 \rangle = R_{mn}(0)$. The discussion following relation (156) in Section 3.4.2 applies equally well for the present case of a rectangular flat plate.

3.4.4 Influence of Clamped Edges, and of Additional Membrane and Buckling Stresses, on Structural Response to an Oscillating Shock Front. - For excitation from a shock front oscillating at a relatively low frequency, only a few low-order modes of the structure contribute significantly to response. At the same time, any deviations from the idealized conditions (for example, clamped boundaries instead of simply supported boundaries for the structure) show maximum effect for the lowest-order modes. An approximate but simple way to account for such deviations is to assume that the modal shapes are still the same as those in the idealized situation. This may not be too serious an approximation if the interaction between the oscillating shock and the structure is restricted to a portion of the structure surface well inside the structure boundaries. With this approximation, the deviations from the idealized situation would change only the resonance frequencies for the low-order modes. The few lowest resonance frequencies can be determined either experimentally or by separate analyses. For example, it is well known that the fundamental frequency for a clamped rectangular plate is approximately twice the fundamental frequency for a similar plate with simply supported edges. Once the actual resonance frequencies for the low-order modes are known, the structural response can be estimated approximately by using the results of Sections 3.4.2 and 3.4.3.

NOTES AND REFERENCES

1. Lighthill, M. J.: On Sound Generated Aerodynamically, Part I, General Theory. Proc. Roy. Soc. (London), Vol. A221, 1952, pp. 564-587.

2. Lighthill, M. J.: On Sound Generated Aerodynamically, Part II, Turbulence as a Source of Sound. Proc. Roy. Soc. (London), Vol. A222, 1954, pp. 1-32.

3. Curle, N.: The Influence of Solid Boundaries upon Aerodynamic Sound. Proc. Roy. Soc. (London), Vol. A231, 1955, pp. 505-514.

4. Ffowcs Williams, J. E.: The Noise of High Speed Missiles. Vol. II, of Random Vibration, ch. 6, S. H. Crandall, ed., M. I. T. Press., 1963.

5. Dyer, I.; Franken, P. A.; and Ungar, E. E.: Noise Environments of Flight Vehicles. Noise Control, Vol. 6, No. 1, 1960, pp.31-40.

6. Franken, P. A.; and Wiener, F. M.: Estimation of Noise-Levels at the Surface of a Rocket-Powered Vehicle. SUAE Bull. no. 31, Pt. III April 1963, pp 27-31.

7. Bies, D. A.; and Franken, P.A.: Notes on Scaling Jet and Exhaust Noise. J. Acoust. Soc. Am. Vol. 33, 1961, pp. 1171-1173.

8. Dyer, I.: Estimation of Sound-Induced Missile Vibration . in Random Vibration, ch. 9, S. H. Crandall, ed., John Wiley + Sons, Inc., 1958.

9. Sutherland, L. C.; and Morgan, W. V.: Use of Model Jets for Studying Acoustic Fields Near Jet and Rocket Engines. Noise Control, Vol. 6, no. 3, 1960, pp. 6-12.

10. Kistler, A. L.: Surface Pressure Fluctuations Produced by Attached and Separated Supersonic Boundary Layers. AGARD Rep. 458, North Atlantic Treaty Organization, 1963.

11. Schlighting, H.: Boundary Layer Theory. McGraw-Hill Book Company, Inc., 1960, ch. 21.

NOTES AND REFERENCES (cont'd)

12. Clauser, F. H.: The Turbulent Boundary Layer. Advan. App. Mech., Vol. 4, 1956, pp. 1-51.

13. Willmarth, W. W.; and Wooldridge, C. E.: Measurements of the Fluctuating Pressure at the Wall Beneath a Thick Turbulent Boundary Layer. Fluid Mech., Vol. 14, no. 2, 1962, pp. 187-210.

14. Bies, D. A.: A Review of Flight and Wind Tunnel Measurements of Boundary Layer Pressure Fluctuations and Induced Structural Response. Bolt Beranek and Newman Inc., Los Angeles, Calif.,Rep. no. 1269, 1966.

15. Goldburg, A.; Washburn, W. K.; and Florsheim, B. H.: Strouhal Numbers for the Hypersonic Wakes of Spheres and Cones. AIAA J. Vol. 3, no. 7, 1965, pp. 1332-1333

16. Goldburg, A.; and Florsheim, B.H.: Transition and Strouhal Number for the Incompressible Wake of Various Bodies. Phys. Fluids, Vol. 9, no. 1, 1966, pp. 45-50.

17. Cometta, C.: An Investigation of the Unsteady Flow Pattern in the Wake of Cylinders and Spheres Using a Hot-Wire Probe. AFOSR-TN-57-760, Brown Univ. Div. Eng., 1958.

18. Jones, G. W.; and Foughner, J. T.: Investigation of Buffet Pressures on Models of Large Manned Launch Vehicle Configurations. NASA TN-D-1633, 1963.

19. Shelton, J. D.: Collation of Fluctuating Buffet Pressures for the Mercury/Atlas and Apollo/Saturn Configurations. NASA CR-66059, 1966.

20. Wiley, D. R.; and Seidl, M. G.: Aerodynamic Noise Tests on X-20 Scale Models. The Boeing Co., Tech. Rept. AFFDL-TR-65-192, Vols. I and II, 1965.

21. Coe, C. F.: The Effects of Some Variations in Launch-Vehicle Nose Shape on Steady and Fluctuating Pressures at Transonic Speeds. NASA TMX-646, 1964.

22. Kuehn, D. M.: Experimental Investigation of the Pressure Rise Required for the Incipient Separation of Turbulent Boundary Layers in Two-Dimensional Supersonic Flow. Memo. 1-21-59A, NASA, 1959.

NOTES AND REFERENCES (cont'd)

23. Kuehn, D. M.: Turbulent Boundary-Layer Separation Induced by Flares on Cylinders at Zero Angle of Attack. NASA TR-R-117, 1961,

24. Williams, III, J. C.: On the Upstream Length of Turbulent Boundary-Layer Separation. AIAA J., Vol. 3, no. 12, 1965, pp. 2347-2348.

25. Speaker, W. V.; and Ailman, C.M.: Spectra and Space-Time Correlations of the Fluctuating Pressures at a Wall Beneath a Supersonic Turbulent Boundary Layer Perturbed by Steps and Shock Waves. Douglas Aircraft Co., Inc., Rept. SM-49806, 1965.

26. The value of $2\delta^*$ for the extent of spatial correlation in the direction transverse to the main flow is well within the experimentally measured range. For example, see Ref. 25. Additional sources of experimental data are listed in Ref. 27.

27. For details regarding the modeling of convecting and decaying pressure fields, see:
Chandiramani, K. L.: Interpretation of Wall Pressure Measurements under a Turbulent Boundary Layer. Bolt Beranek and Newman Inc., Rept. No. 1310, 25 August 1965.

28. Heckl, M.: Vibrations of Point-Driven Cylindrical Shells. J. Acoust. Soc. Am. Vol. 32, no. 10, October 1962. pp. 1553-1557. In this paper, various degrees of approximations in shell theory are discussed and further references are provided.

29. Wang, C. T.: Applied Elasticity McGraw-Hill Book Co., Inc., 1953. Equation (3.3)can be derived by starting with differential equations using the simple static equations described in Sections 11.1 and 12.4 of this reference. The extension to the orthotropic case is then quite straightforward. Of course, the detailed analyses for both of these cases must be carried out for a conservative system (which, by the way, also allows elegant derivations from variational or energy methods). Any Dissipation must be introduced heuristically at the stage where final response estimates are to be made.

30. For a discussion of flexural vibration of a corrugated plate, see:
    Heckl, M.: Untersuchungen an Orthotropen Platten. Acustica, Vol. 10, 1960, pp. 109-115.

31. The radial variation of these pressure fields can be expressed in terms of the Bessel function of the first kind J(r), the modified Bessel function I(r), or the simple power law r^m. For the first of these solutions, see:
    Morse, P. M.: Vibration and Sound. Second ed. McGraw-Hill Book Co., Inc., 1948, ch. 5, pp. 187-188, ch. 7, p. 298.

32. For a more detailed and general discussion, refer to:
    Smith, P. W. Jr.; and Lyon, R. H.: Sound and Structural Vibration, NASA CR-160, 1965.

33. Manning, J. E.; Lyon, R. H.; Scharton, T. D.: Analytical Procedure for Determining Random Load Acting on a Spacecraft due to Primary Random Load Acting on an Exterior Structure. First Quart. Progr. Rept. Project OGO, Bolt Beranek and Newman Inc., June-August 1965. See Sections 3.3 and Figs. 7 and 8.

34. For a detailed discussion of radiation resistance, coupling parameter, etc., see Ref. 32, Chapter 5.

35. Smith, P. W. Jr.: Response and Radiation of Structural Modes Excited by Sound. J. Acoust. Soc. Am., Vol. 34, 1962 pp. 640-647. In this reference, the relation between the radiation resistance and the coupling parameter is derived from the reciprocity principle.

36. Maidanik, G.: Response of Ribbed Panels to Reverberant Acoustic Fields. J. Acoust. Soc. Am., Vol. 34, 1962, pp. 809-862. In this reference, expressions for the radiation resistance of single modes, and the radiation resistance of a reverberant vibration field are derived for a rectangular flat plate. Interpretation of the Acoustically fast and slow modes in terms of the net volume velocities at the surface, edges, or corners of the panel is also provided in detail.

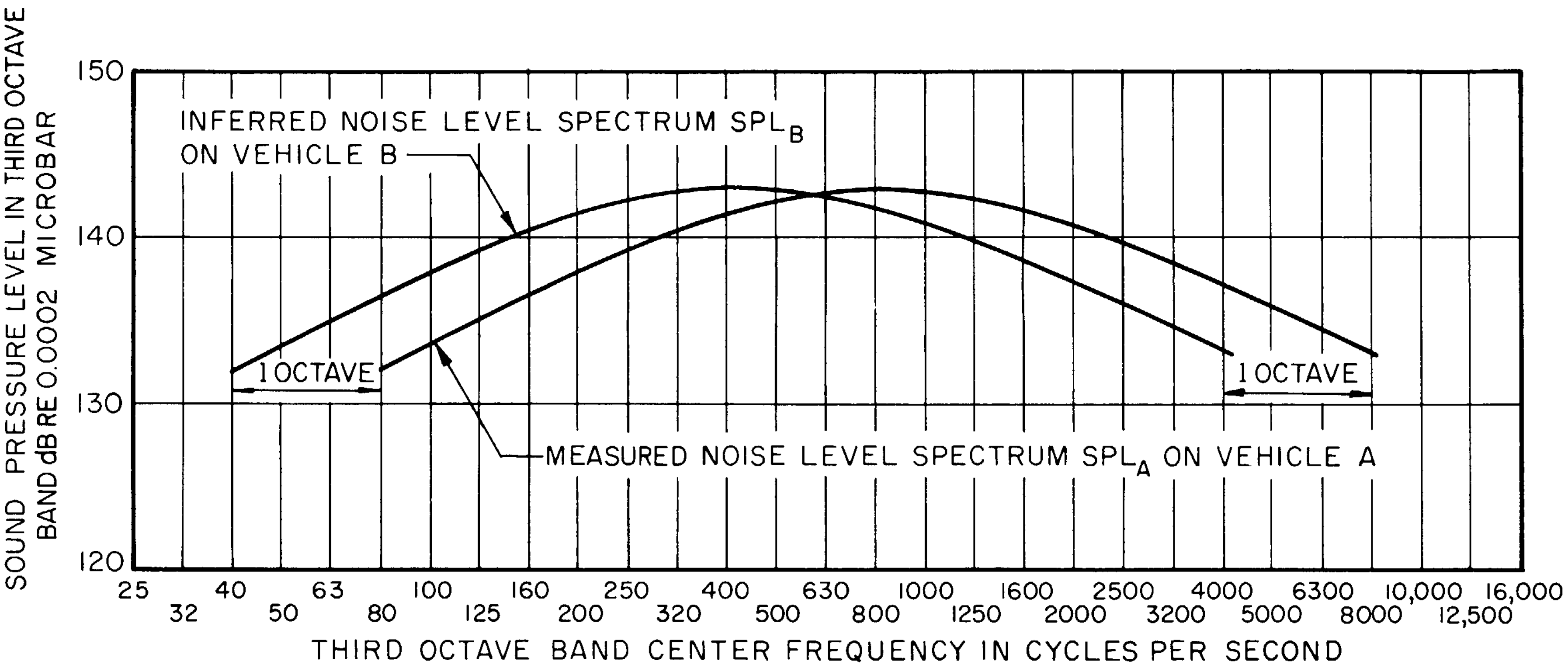

FIG. 1 ESTIMATE OF LIFT-OFF NOISE LEVELS ON VEHICLE B, BASED ON SCALING OF DATA ON VEHICLE A

37. Manning, J. E.; and Maidanik, G.: Radiation Properties of Cylindrical Shells. J. Acoust. Soc. Am., Vol. 36, 1964, pp. 1691-1698.

38. A detailed and thorough analysis for response of a rectangular flat plate to TBL excitation is performed in reference 39. The approach here is modal. In reference 40, the equivalence between the modal approach for the finite structure and the"wavenumber"approach for the corresponding infinite structure is demonstrated.

39. Dyer, I.: Response of Plates to a Decaying and Convecting Random Pressure Field. J. Acoust. Soc. Am., Vol. 31, no. 7, July 1959, pp. 922-928.

40. Ffowcs Williams, J. E.; and Lyon, R. H.: The Sound Radiated From Turbulent Flows Near Flexible Boundaries. Bolt Beranek and Newman Inc., Rept. no. 1054, Contract Nonr 2321(00), 15 August 1963.

41. For some details regarding the calculation of $\Pi_b(\omega)$, see: Lyon, R. H.: Aerodynamic Noise Simulation in Sonic Fatigue Facility, Phase I, Part II: Studies on Structural Response. Bolt Beranek and Newman Inc., Rept. 1171, 24 December 1964.

42. Lyon, R. H.; and Maidanik, G.: Power Flow Between Linearly Coupled Oscillators. J. Acoust. Soc. Am., Vol. 34, no. 5, May 1962, pp. 623-639.

43. Manning, J. E.: Noise Reduction by a Cylindrical Shell. Paper presented at the 71st Meeting, Acoust. Soc. Am. (Boston, Mass.), June 1966.

44. Wang, M. C.; and Uhlenbeck, G. E.: On the Theory of the Brownian Motion II. Rev. Mod. Phys. Vol. 17, nos 2 and 3, April-July 1945, pp. 323-342.

45. Chandiramani, K. L.: First Passage Probabilities for a Linear Harmonic Oscillator. Sc. D. Thesis, Mass. Inst. Technol. 1964.

46. For a detailed discussion of the relation between velocity and stress levels, see: Hunt, F. V.: Stress and Strain Limits on the Attainable Velocity in Mechanical Vibration. J. Acoust. Soc. Am., Vol. 32, no. 9, September 1960, pp. 1123-1128.

47. Ungar, E. E.: Response of Plates to Moving Shocks. Bolt Beranek and Newman Inc., Rept. no. 743, WADD Tech. Rept. 60-445, May 1960.

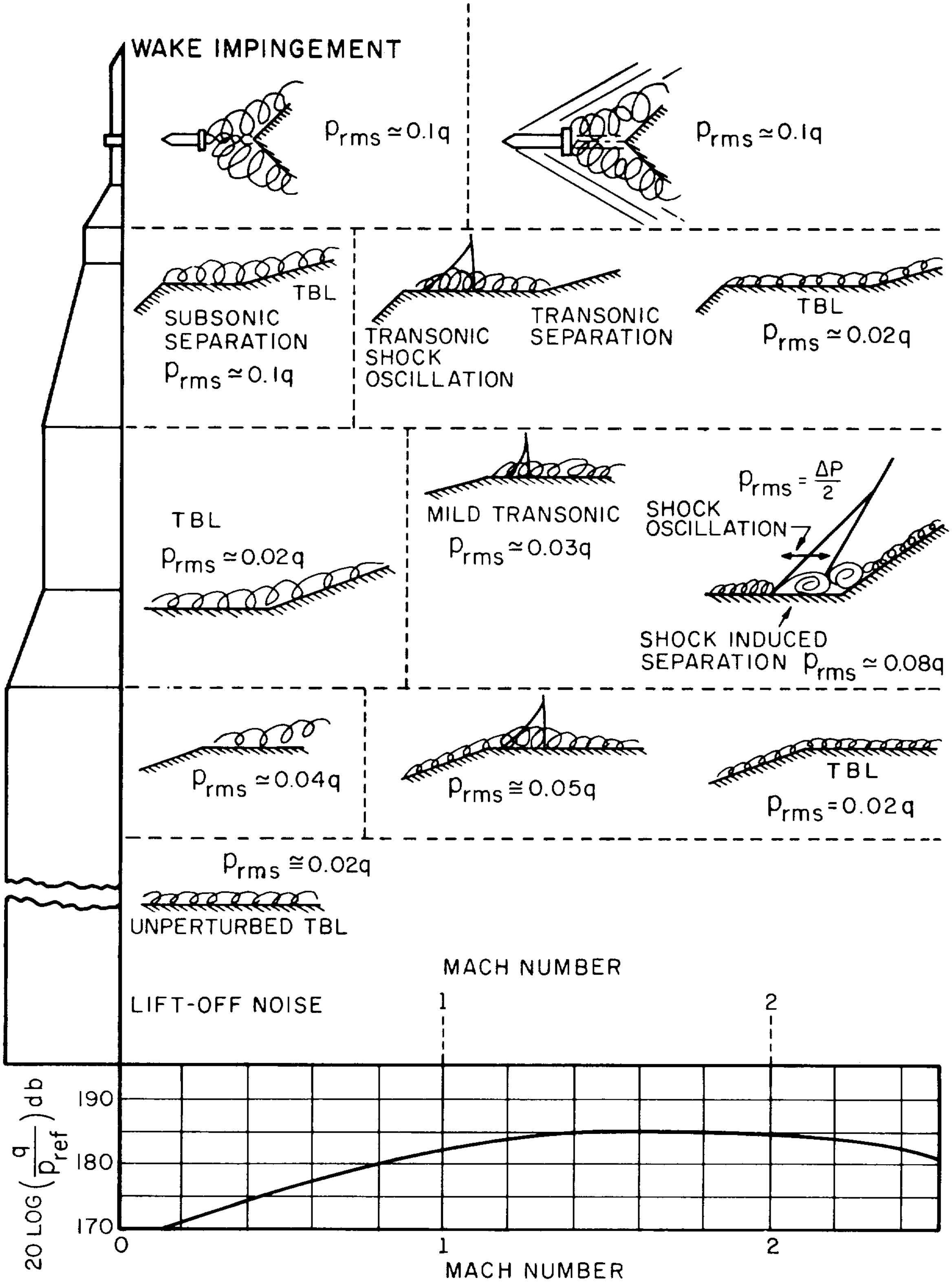
WAKE IMPINGEMENT
$p_{rms} \simeq 0.1q$
$p_{rms} \simeq 0.1q$
TBL
SUBSONIC SEPARATION
$p_{rms} \simeq 0.1q$
TRANSONIC SHOCK OSCILLATION
TRANSONIC SEPARATION
TBL
$p_{rms} \simeq 0.02q$
TBL
$p_{rms} \simeq 0.02q$
MILD TRANSONIC
$p_{rms} \simeq 0.03q$
$p_{rms} = \frac{\Delta P}{2}$
SHOCK OSCILLATION
SHOCK INDUCED SEPARATION $p_{rms} \simeq 0.08q$
$p_{rms} \simeq 0.04q$
$p_{rms} \cong 0.05q$
TBL
$p_{rms} = 0.02q$
$p_{rms} \cong 0.02q$
UNPERTURBED TBL
MACH NUMBER
LIFT-OFF NOISE
1
2
$20 \log \left(\frac{q}{p_{ref}}\right) db$
190
180
170
0
1
2
MACH NUMBER

FIG. 2 SUMMARY OF AERODYNAMIC NOISE SOURCES AS A FUNCTION OF VEHICLE GEOMETRY AND MACH NUMBER

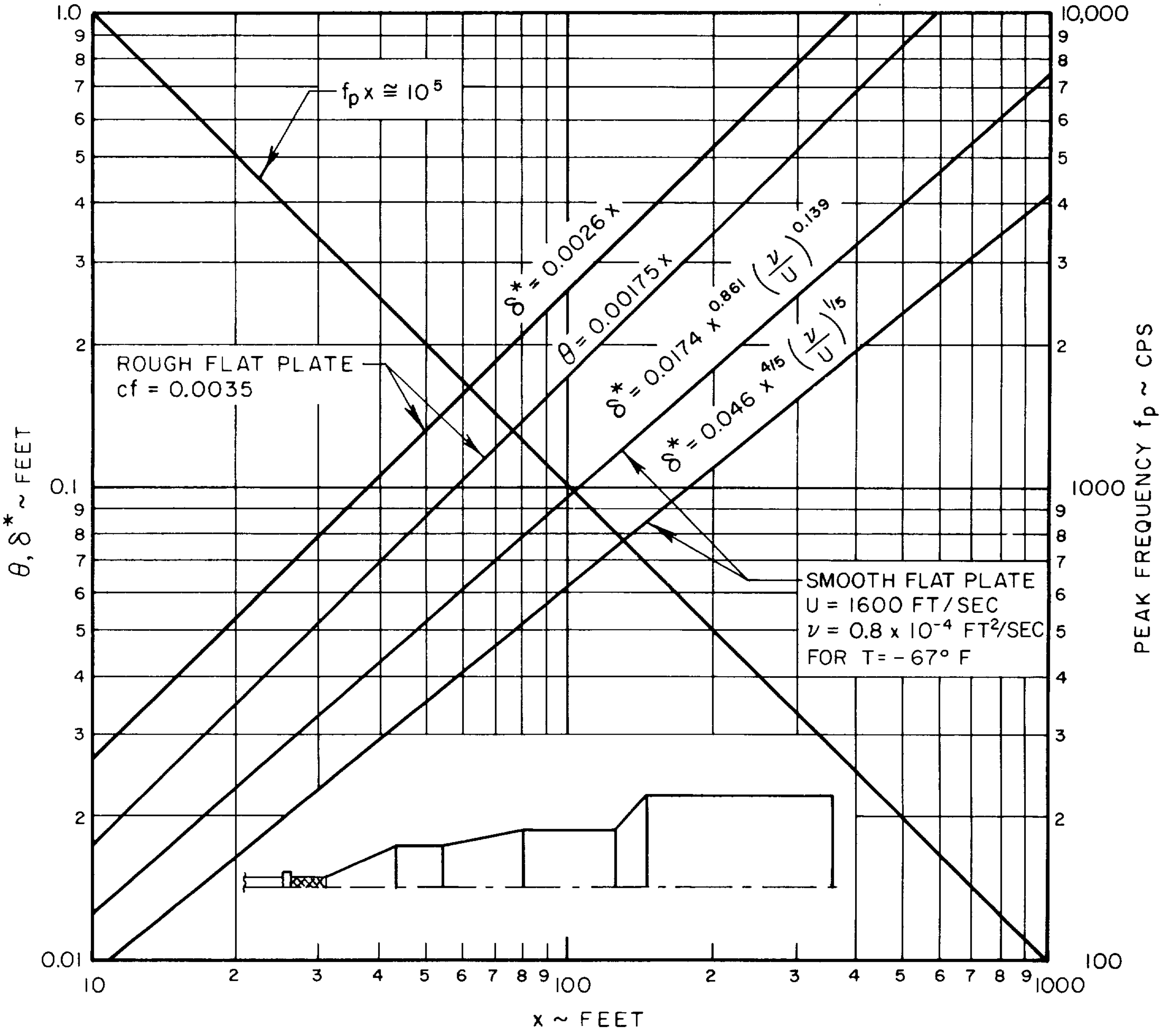

FIG. 3 TURBULENT BOUNDARY LAYER DEVELOPMENT ON A FLAT PLATE

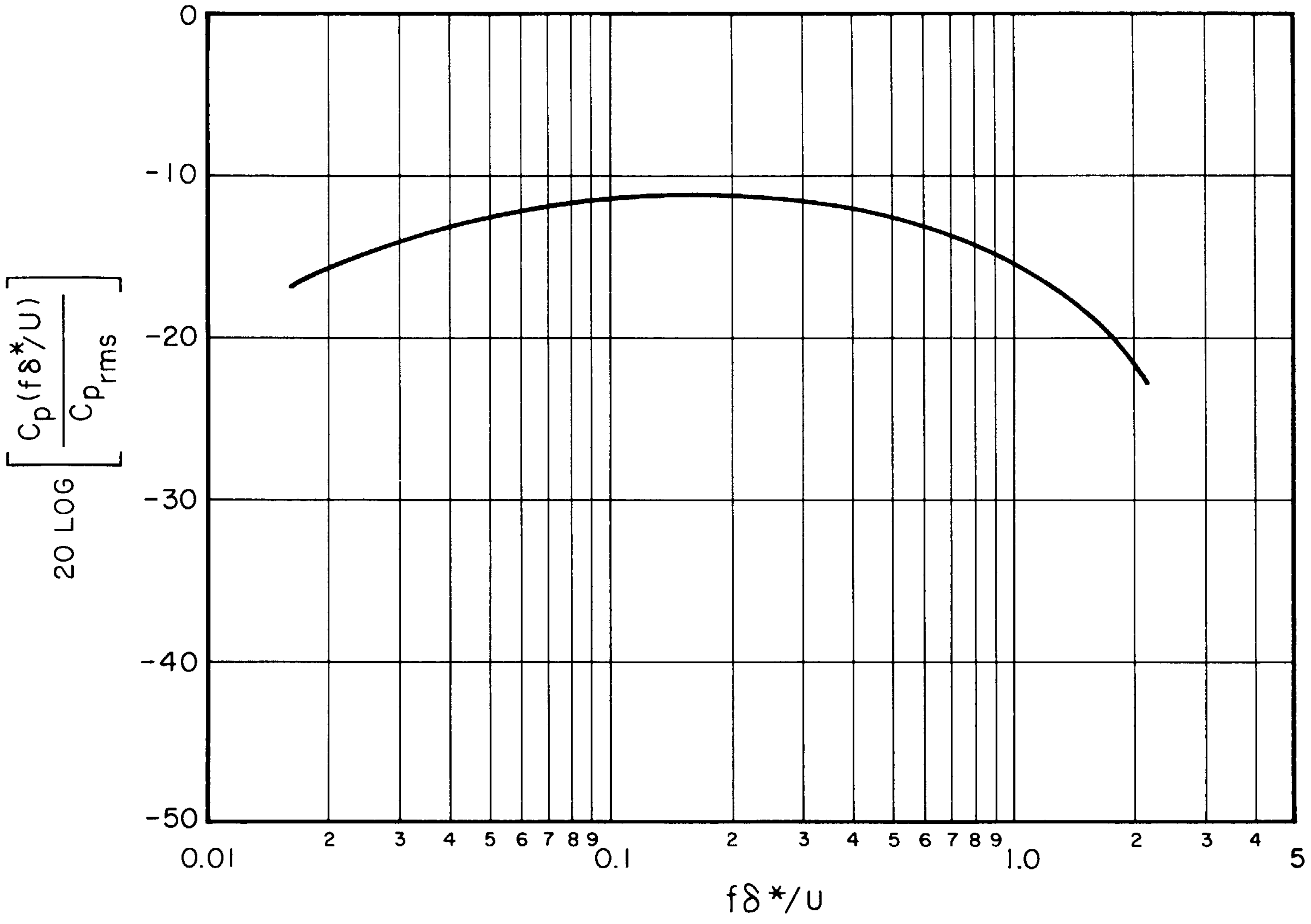

FIG. 4 NONDIMENSIONAL SPECTRUM OF BOUNDARY LAYER PRESSURE FLUCTUATIONS IN THIRD OCTAVE BANDS

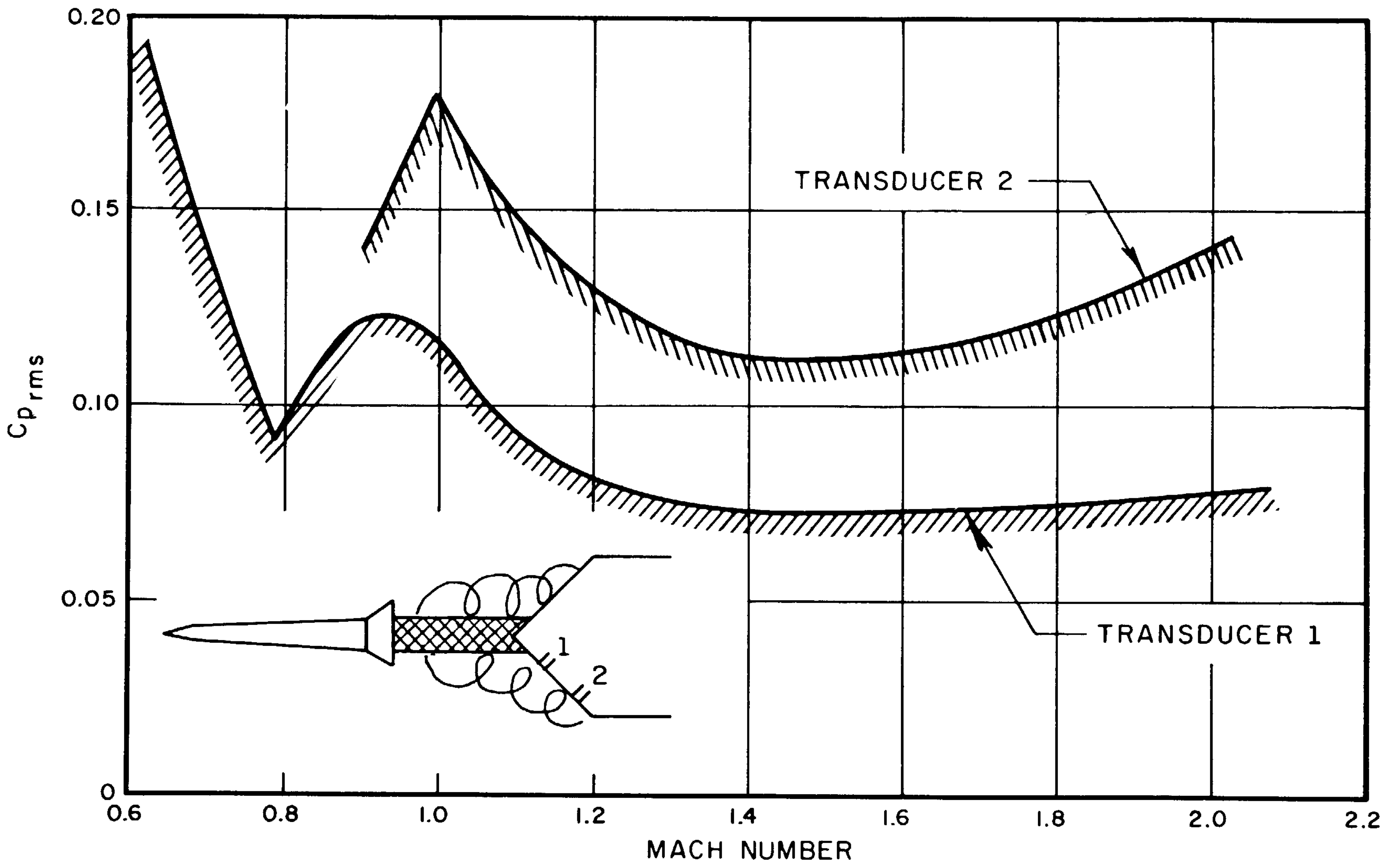

FIG. 6 BOUNDARY OF $C_{p_{rms}}$ FOR WAKE IMPINGEMENT

Subsonic flow

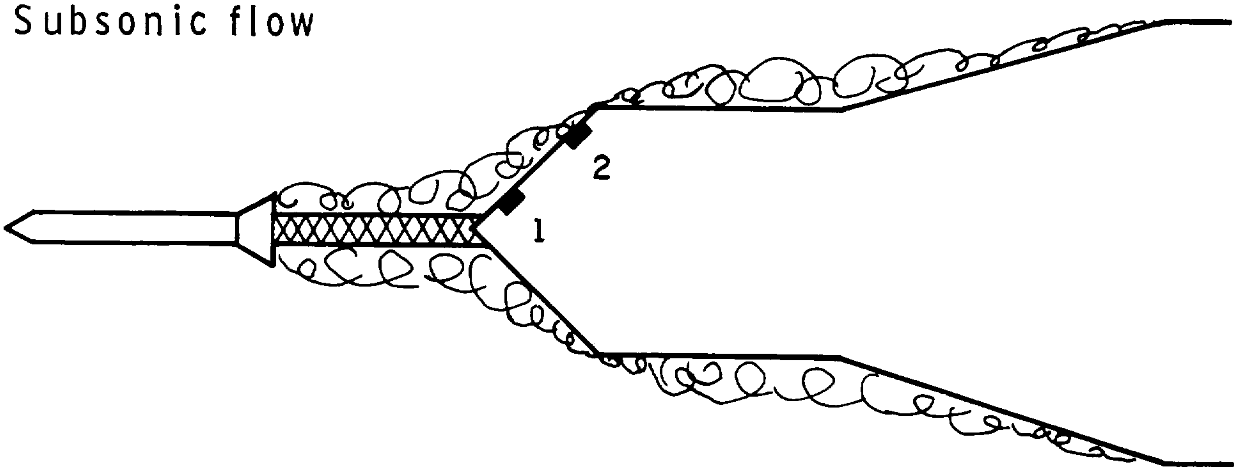

Supersonic flow

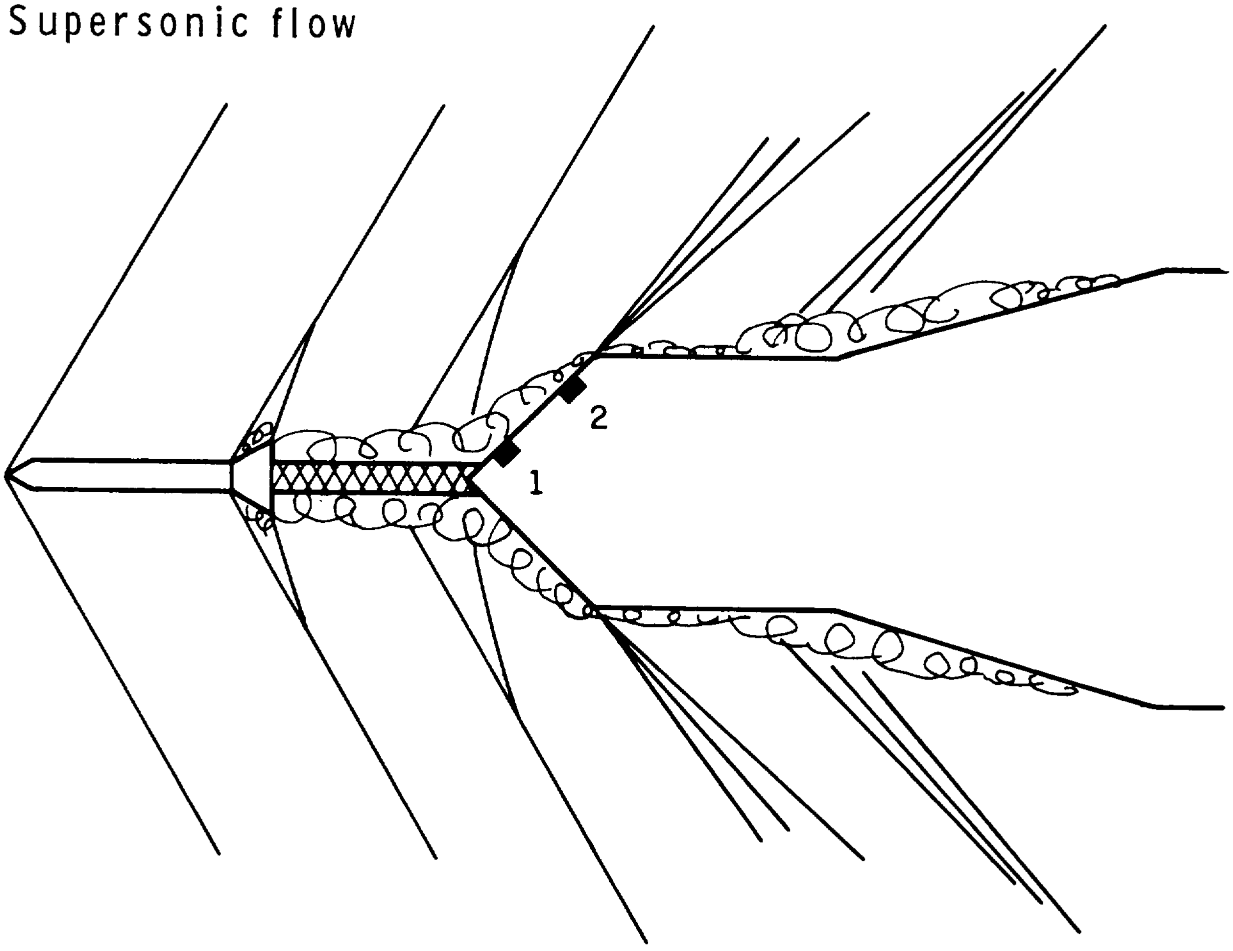

FIG. 5 GROSS FEATURES OF THE FLOW AROUND A LAUNCH VEHICLE DURING SUBSONIC AND SUPERSONIC FLIGHTS

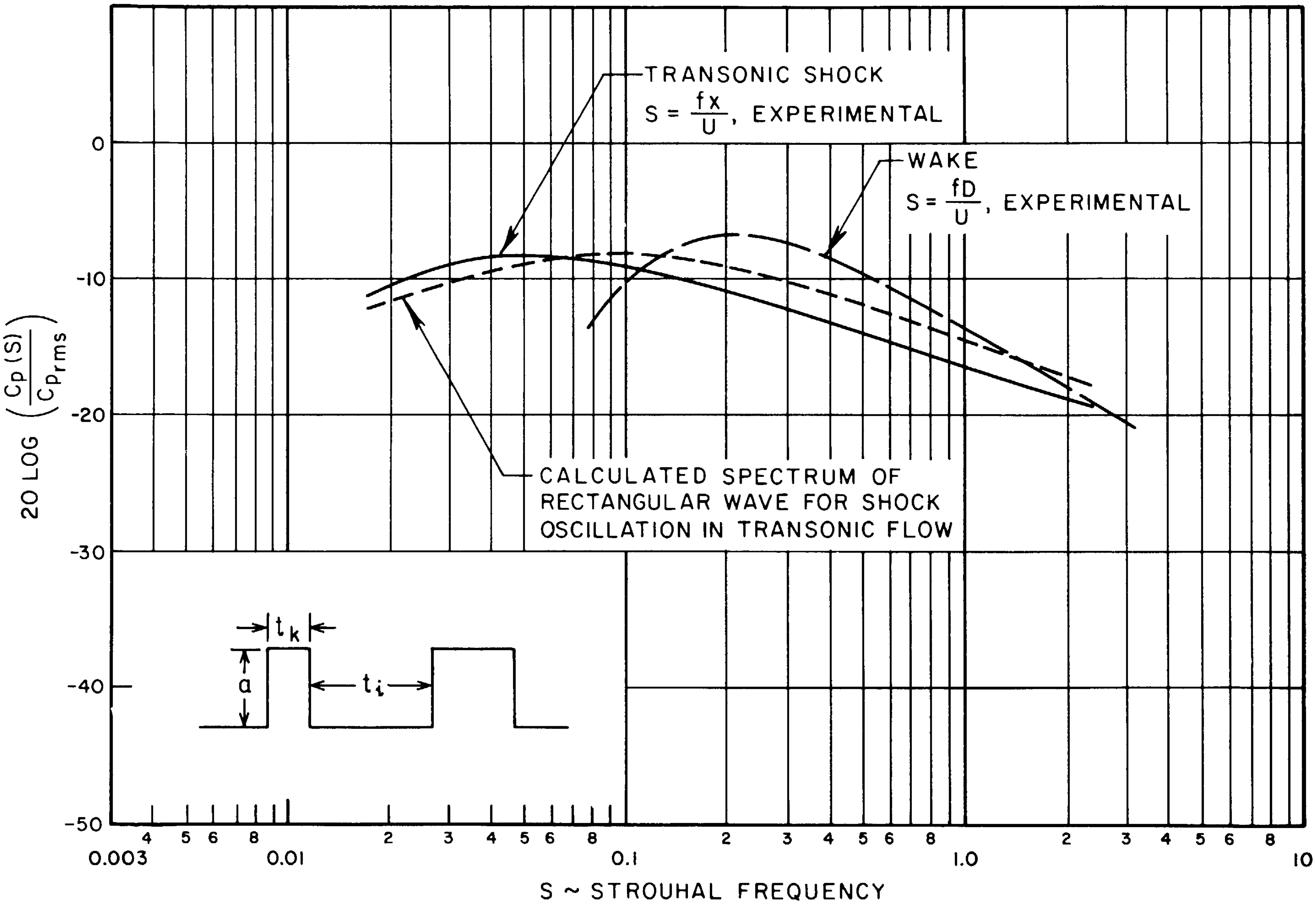

FIG. 7 NONDIMENSIONAL THIRD OCTAVE BAND SPECTRA FOR WAKE IMPINGEMENT AND TRANSONIC SHOCK-BOUNDARY INTERACTION

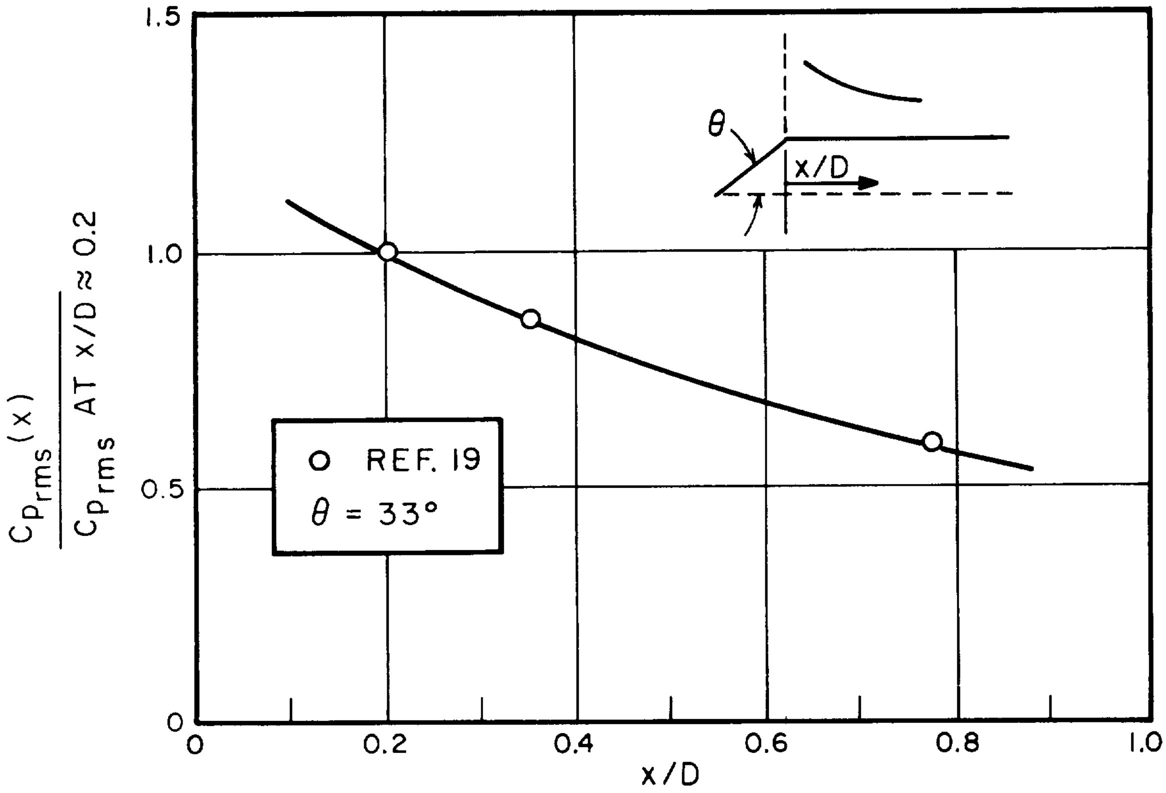

FIG. 8 NORMALIZED DOWNSTREAM DECAY OF $C_{p_{rms}}$ FOR SUBSONIC SEPARATION

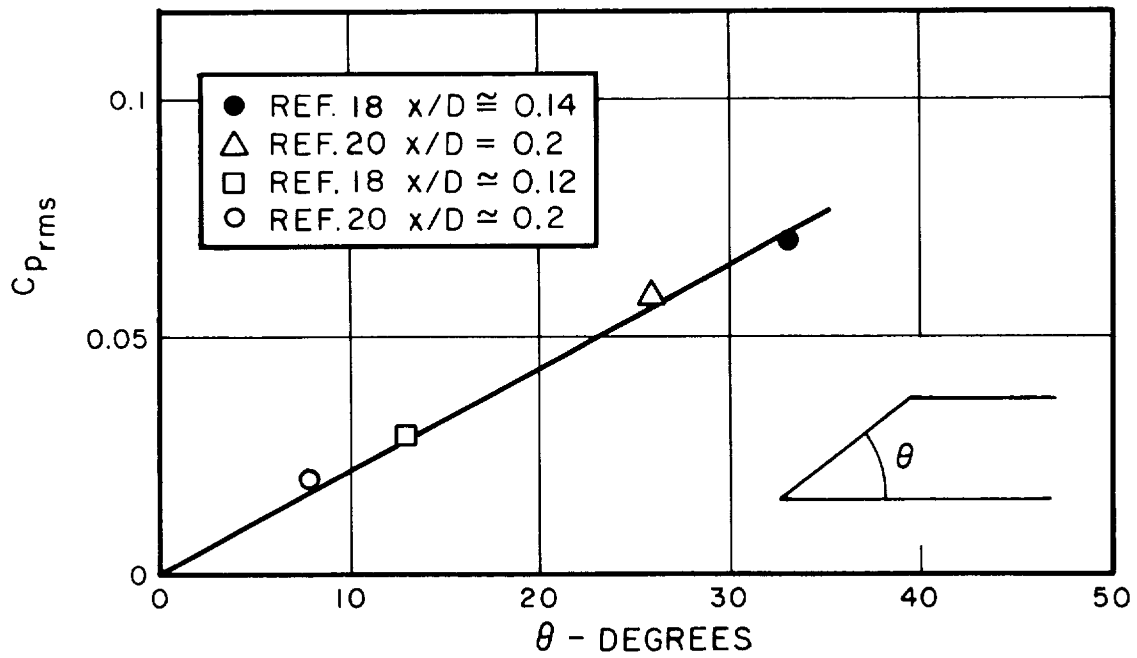

FIG. 9 MAGNITUDE OF $\overline{C}_{p_{rms}}$ AS A FUNCTION OF TURNING ANGLE IN SUBSONIC FLOW

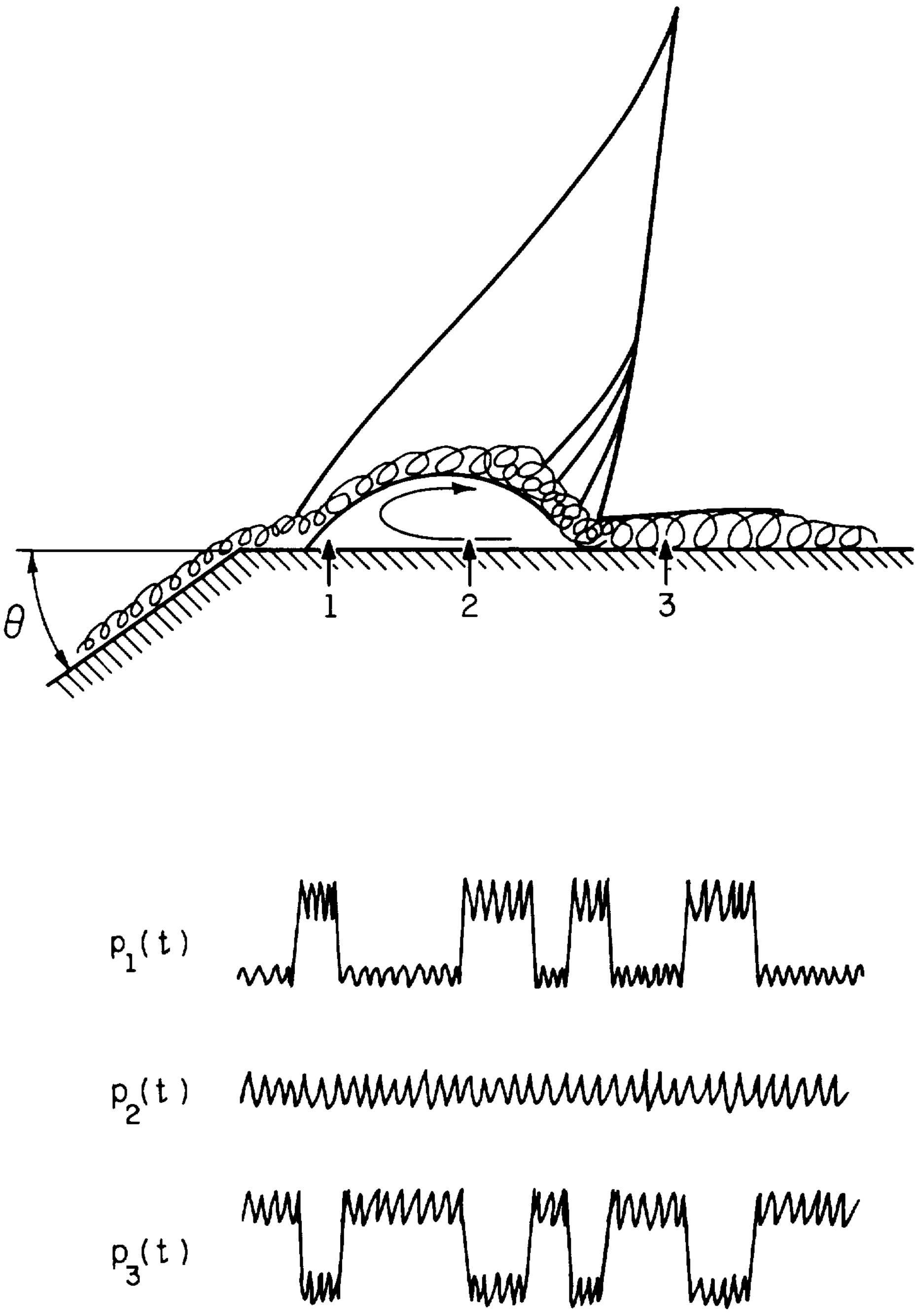
θ
1
2
3
p1(t)
p2(t)
p3(t)

FIG. 10 SKETCH OF TRANSONIC SHOCK-BOUNDARY LAYER INTERACTION AND RESULTING PRESSURE TIME PATTERNS

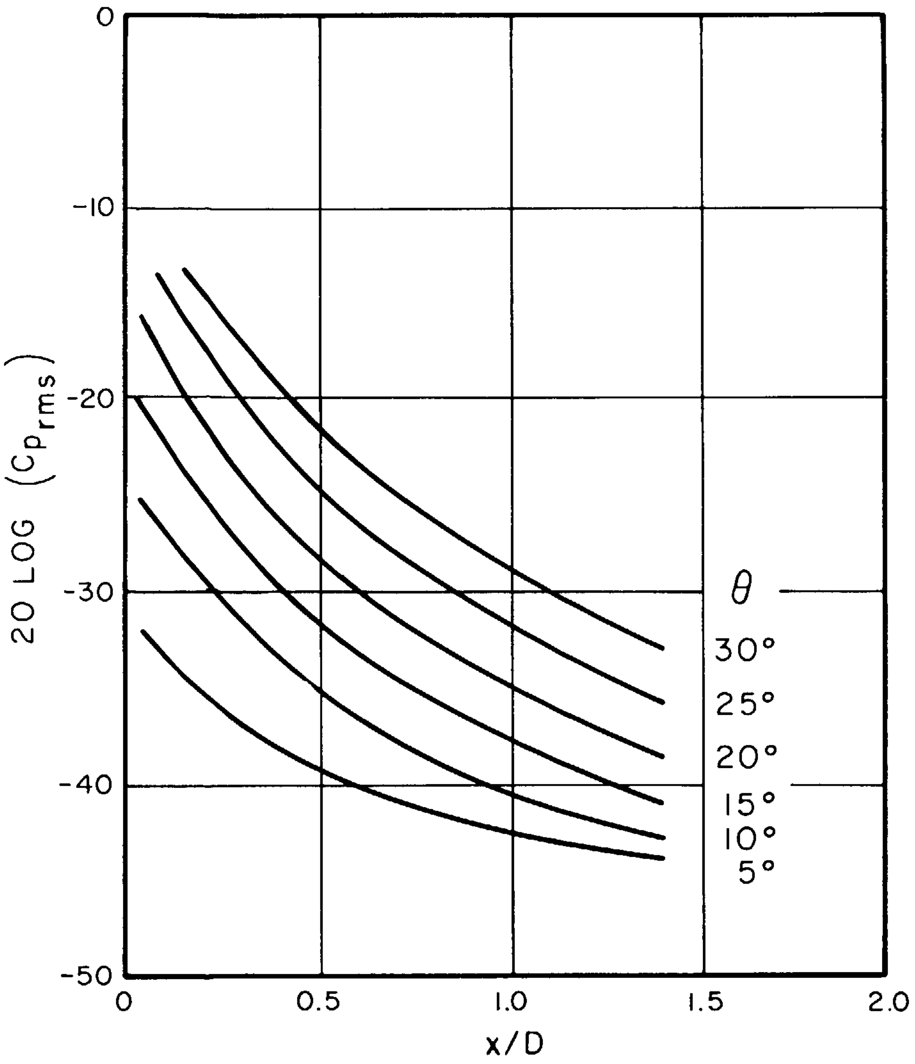

FIG. 11 MAXIMUM $C_{p_{rms}}$ IN TRANSONIC FLOW AS A FUNCTION OF θ AND x/D

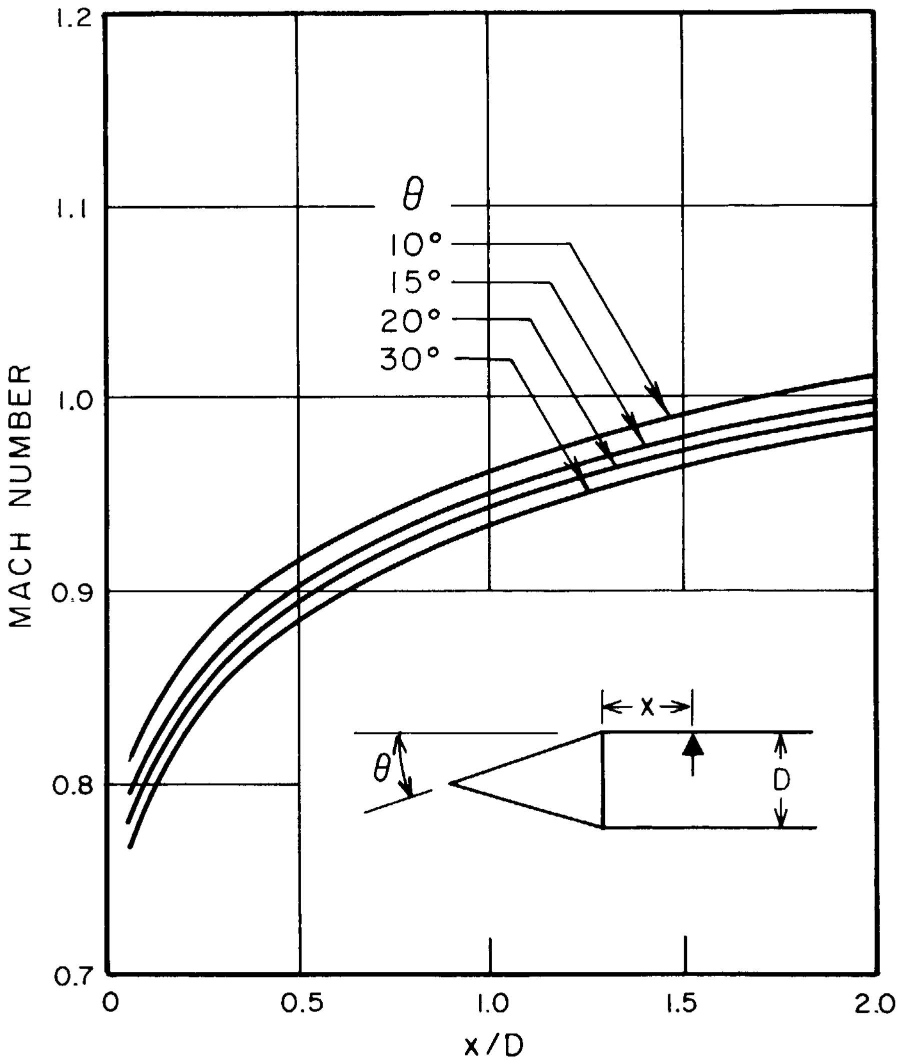

FIG. 12 MACH NUMBER FOR MAXIMUM $C_{p_{rms}}$ AS A FUNCTION OF θ AND x/D

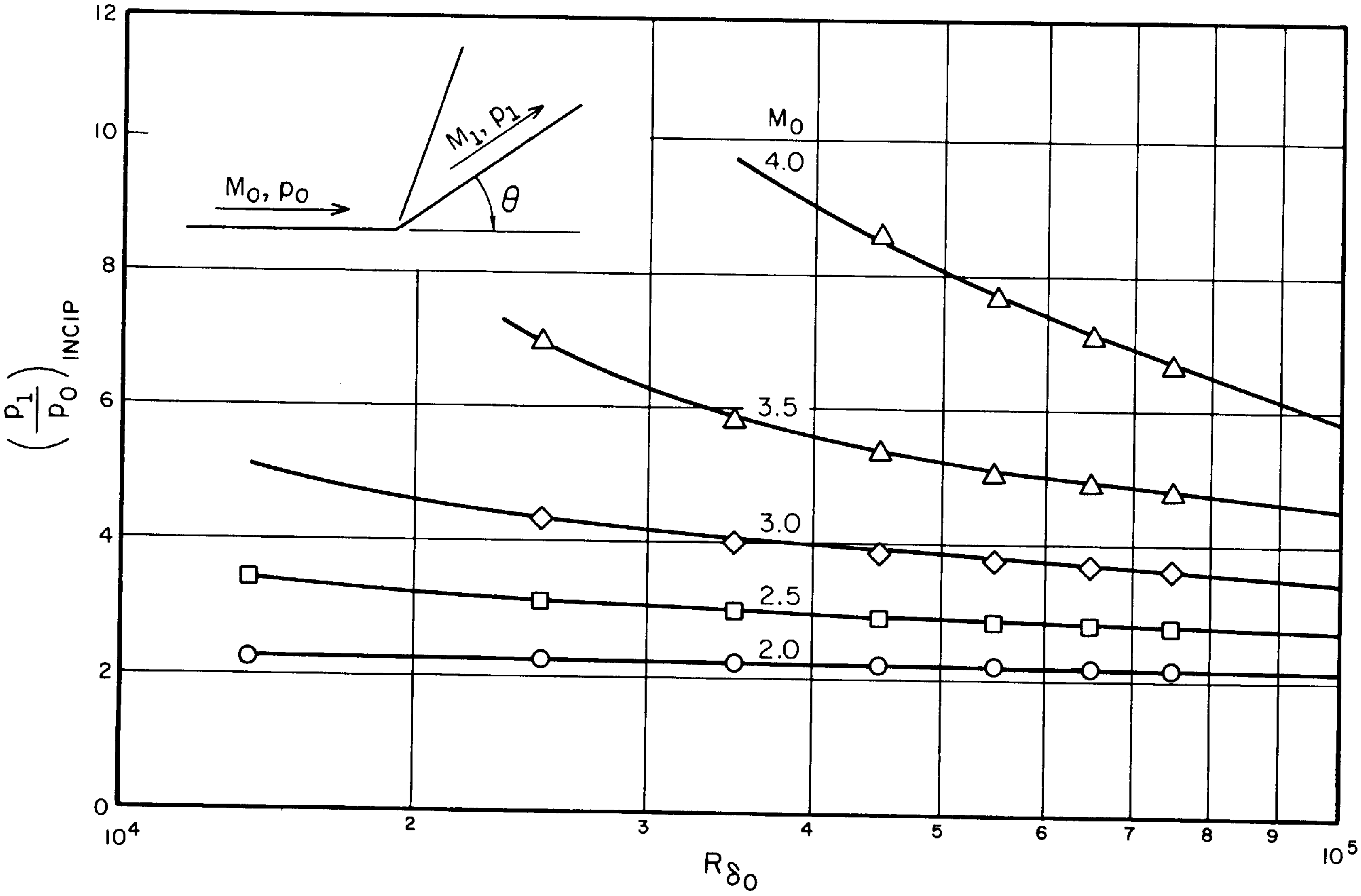

FIG.13 EFFECT OF REYNOLDS NUMBER ON THE PRESSURE RISE FOR SEPARATION AT INTERSTAGE FLARES

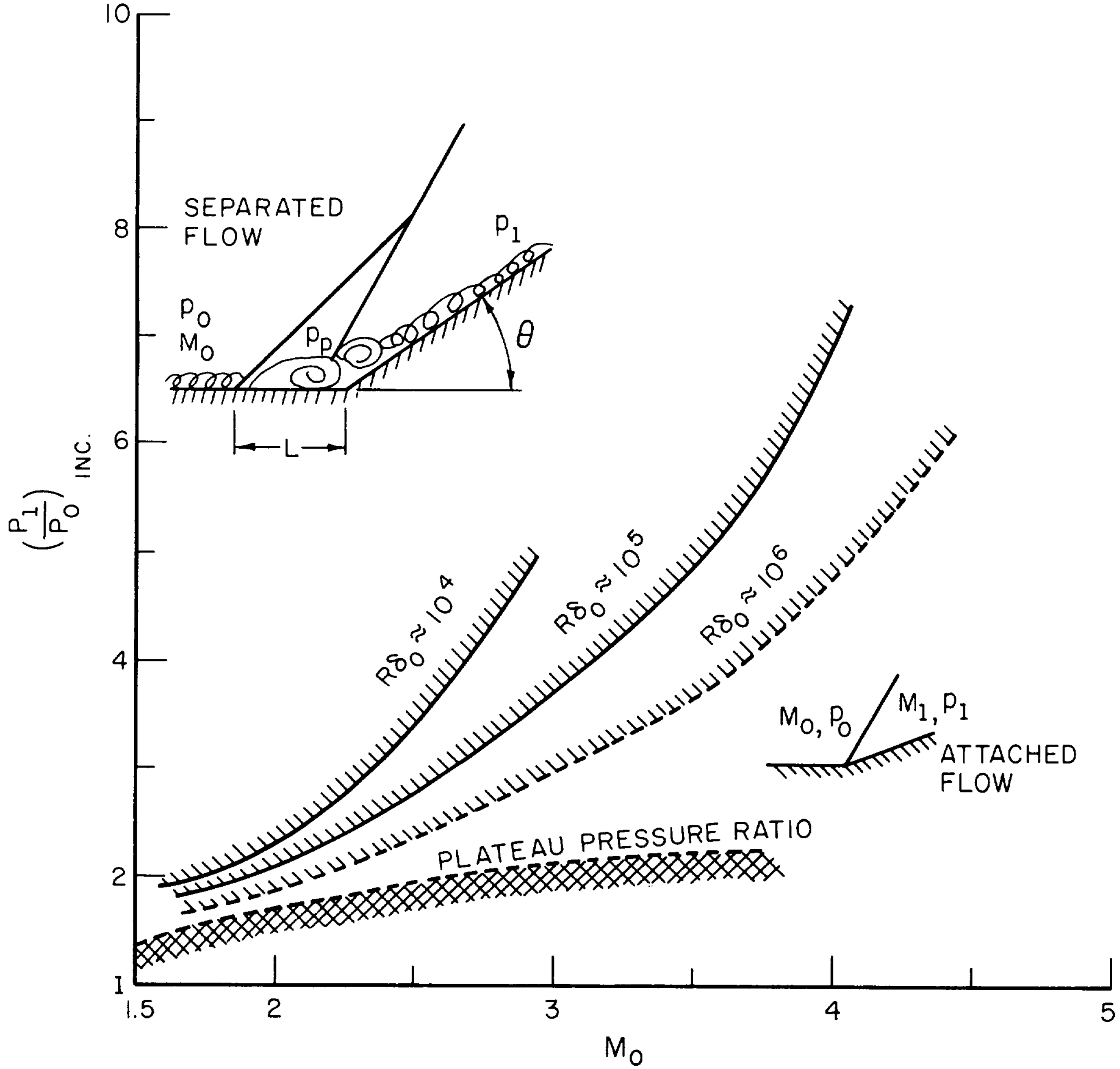

FIG. 14 EFFECT OF MACH NUMBER ON THE PRESSURE RISE FOR SEPARATION AT INTERSTAGE FLARES

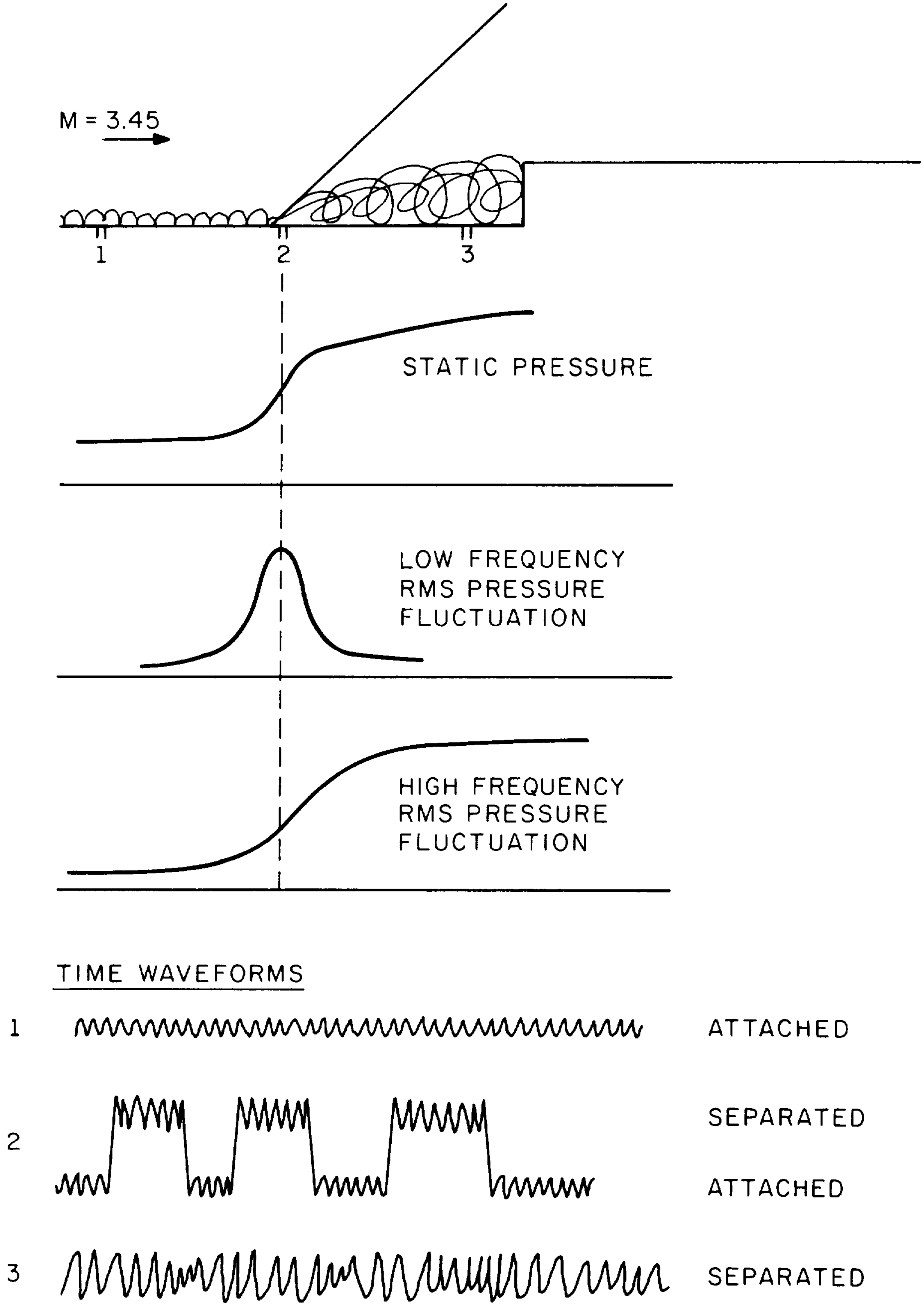
M = 3.45
1
2
3
STATIC PRESSURE
LOW FREQUENCY RMS PRESSURE FLUCTUATION
HIGH FREQUENCY RMS PRESSURE FLUCTUATION
TIME WAVEFORMS
1
ATTACHED
2
SEPARATED
ATTACHED
3
SEPARATED

FIG. 15 SUMMARY OF KISTLERS EXPERIMENT

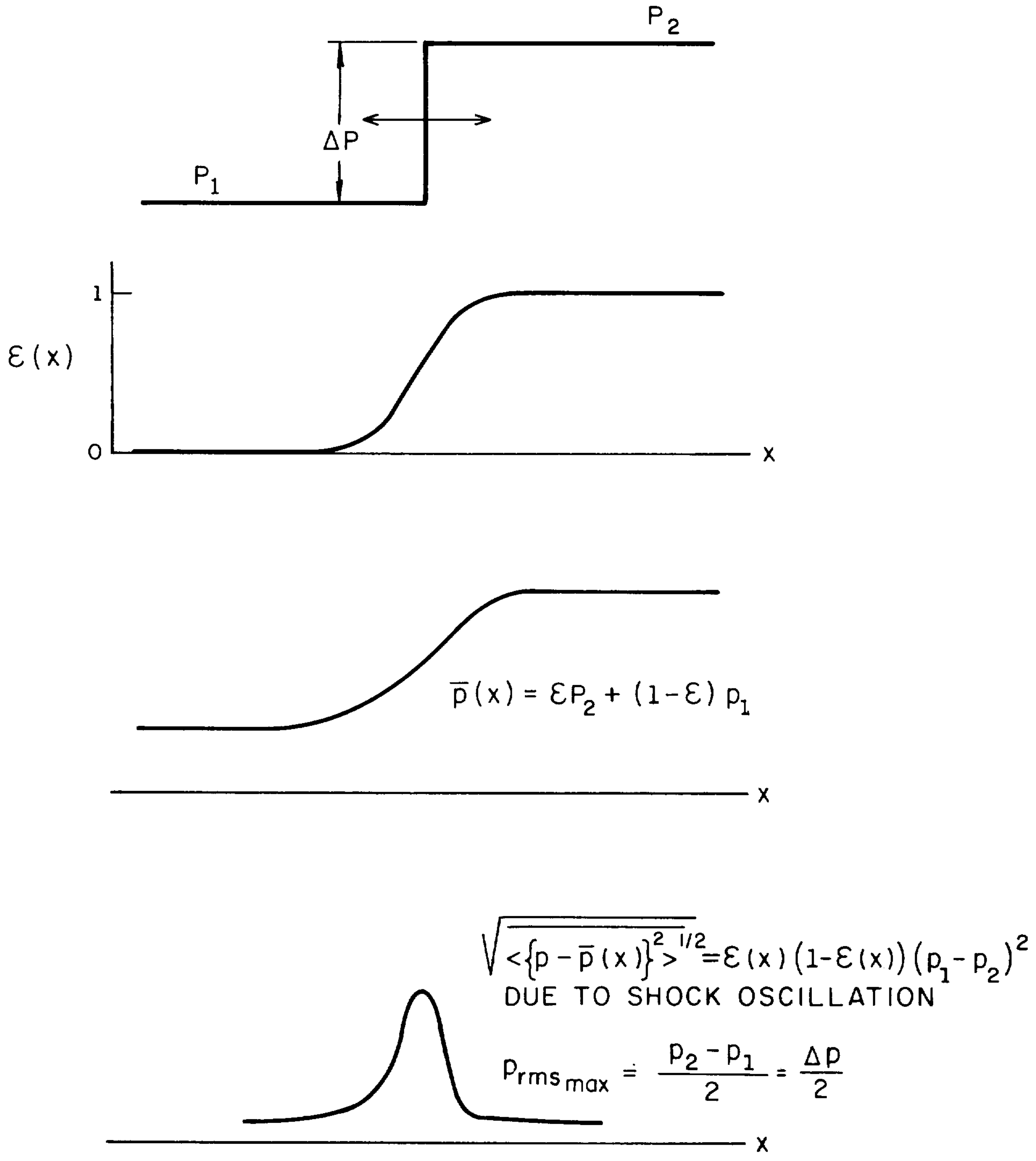
P_2
ΔP
P_1
1
$\varepsilon(x)$
0
x
$\overline{p}(x) = \varepsilon P_2 + (1-\varepsilon)\, p_1$
x
$\sqrt{<\{p-\overline{p}(x)\}^2>^{1/2}} = \varepsilon(x)\,(1-\varepsilon(x))\,(p_1-p_2)^2$
DUE TO SHOCK OSCILLATION
$p_{rms_{max}} \doteq \frac{p_2-p_1}{2} = \frac{\Delta p}{2}$
x

FIG. 16 SKETCH OF $\overline{p}(x)$ AND $p_{rms}(x)$ DUE TO SHOCK OSCILLATION

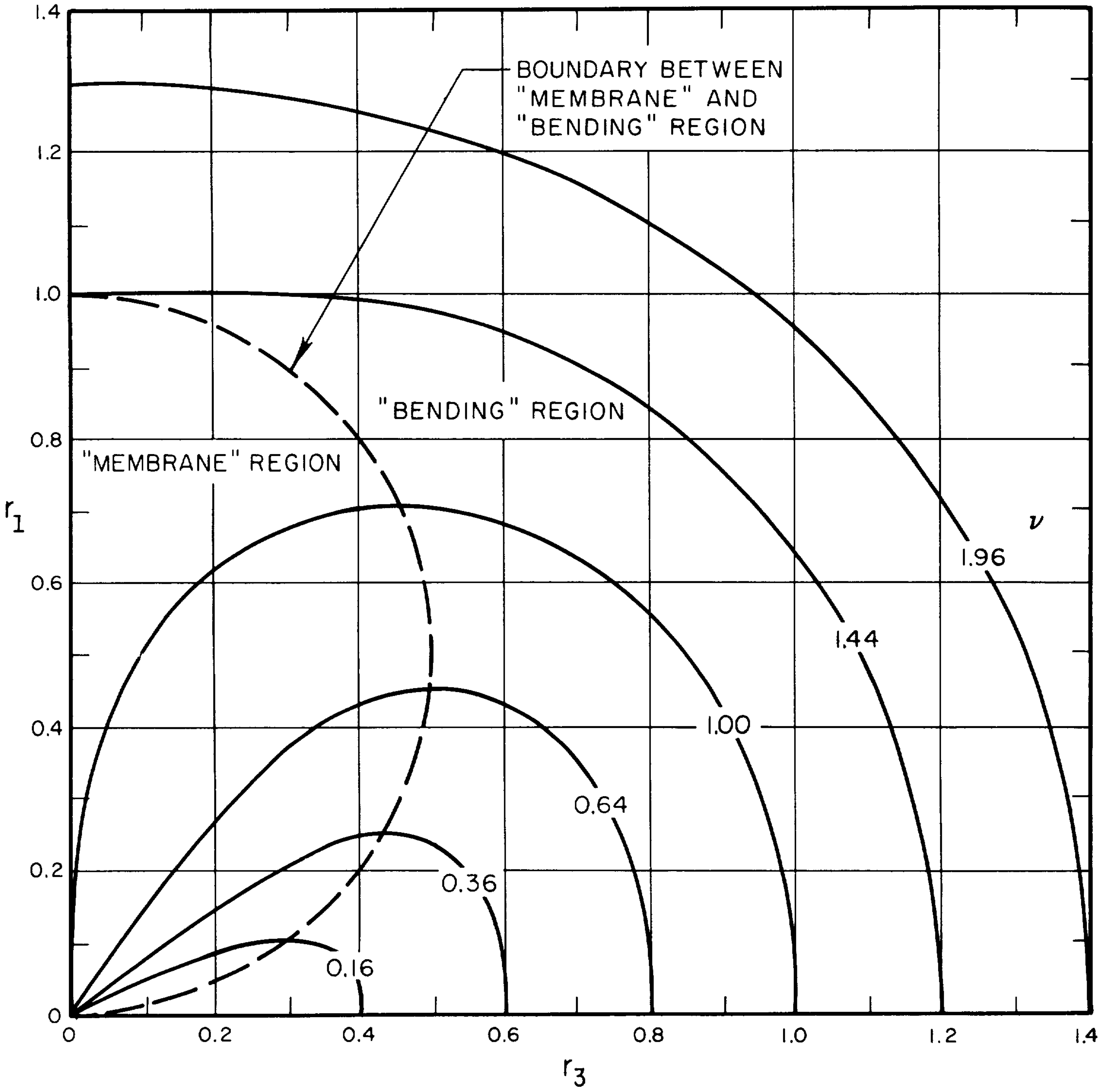

FIG. 17 LOCI OF CONSTANT RESONANCE FREQUENCY IN THE DIMENSIONLESS WAVE NUMBER PLANE (r, θ), ISOTROPIC CYLINDER

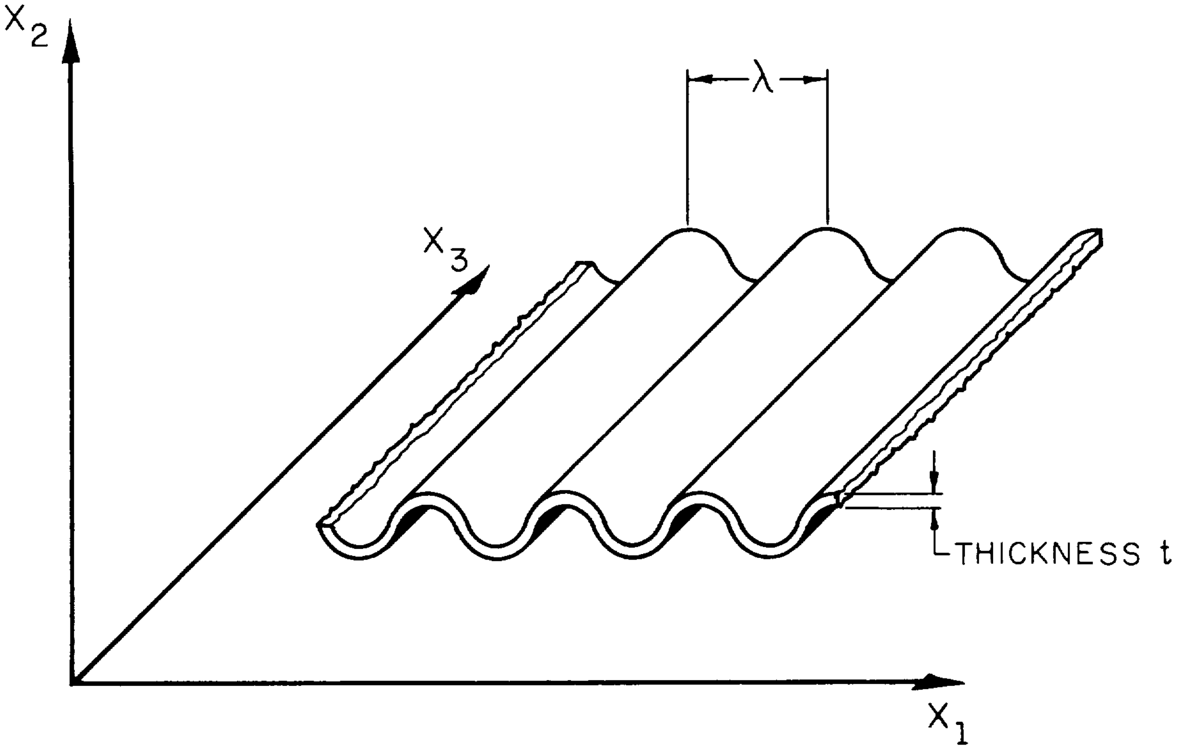
X_2
λ
X_3
THICKNESS t
X_1

FIG.18 SKETCH OF A CORRUGATED STRUCTURE

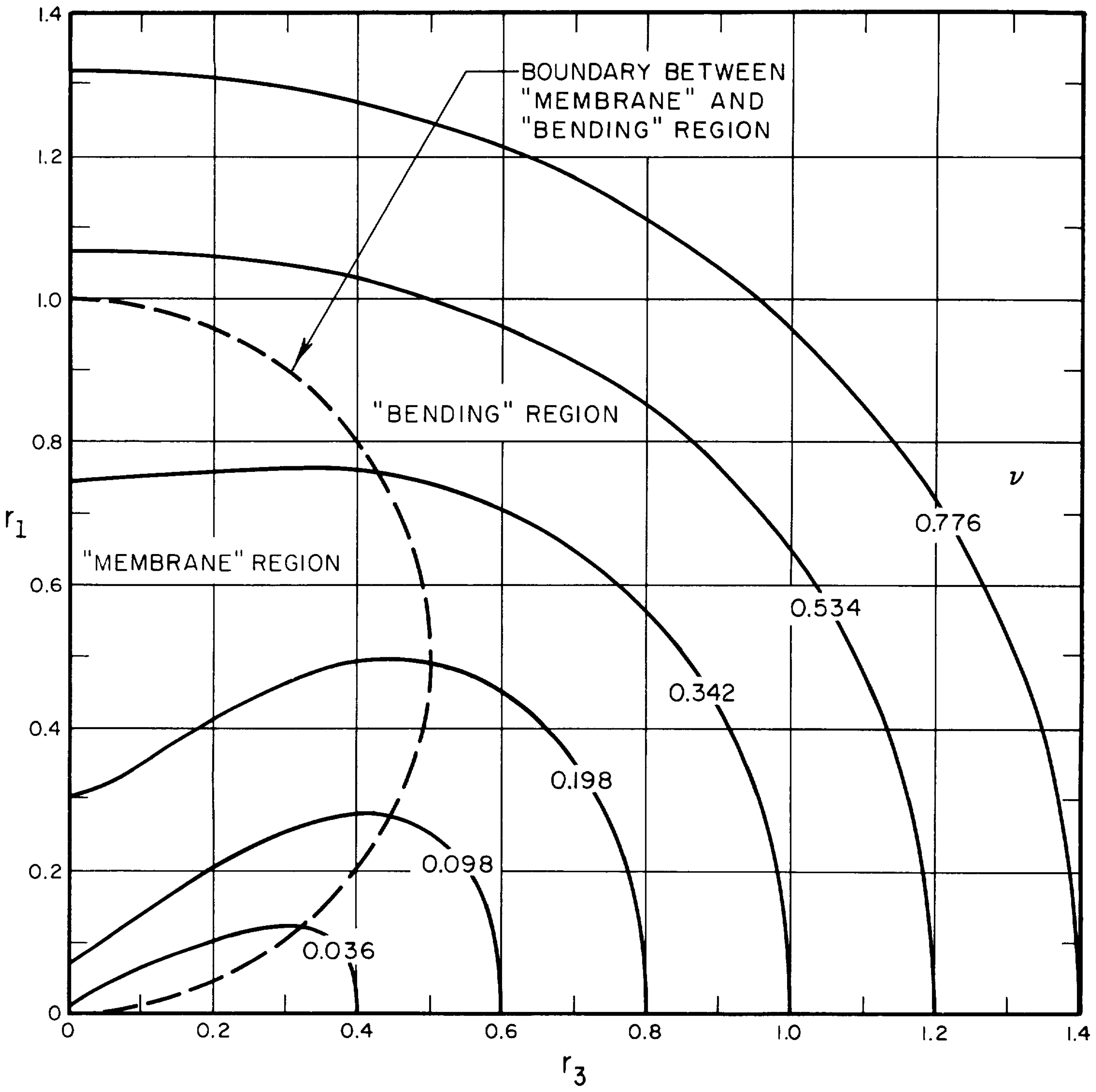

FIG. 19 LOCI OF CONSTANT RESONANCE FREQUENCY IN THE DIMENSIONLESS WAVE NUMBER PLANE (r, θ), LIQUID LOADED ISOTROPIC CYLINDER, $\beta = 7.54$

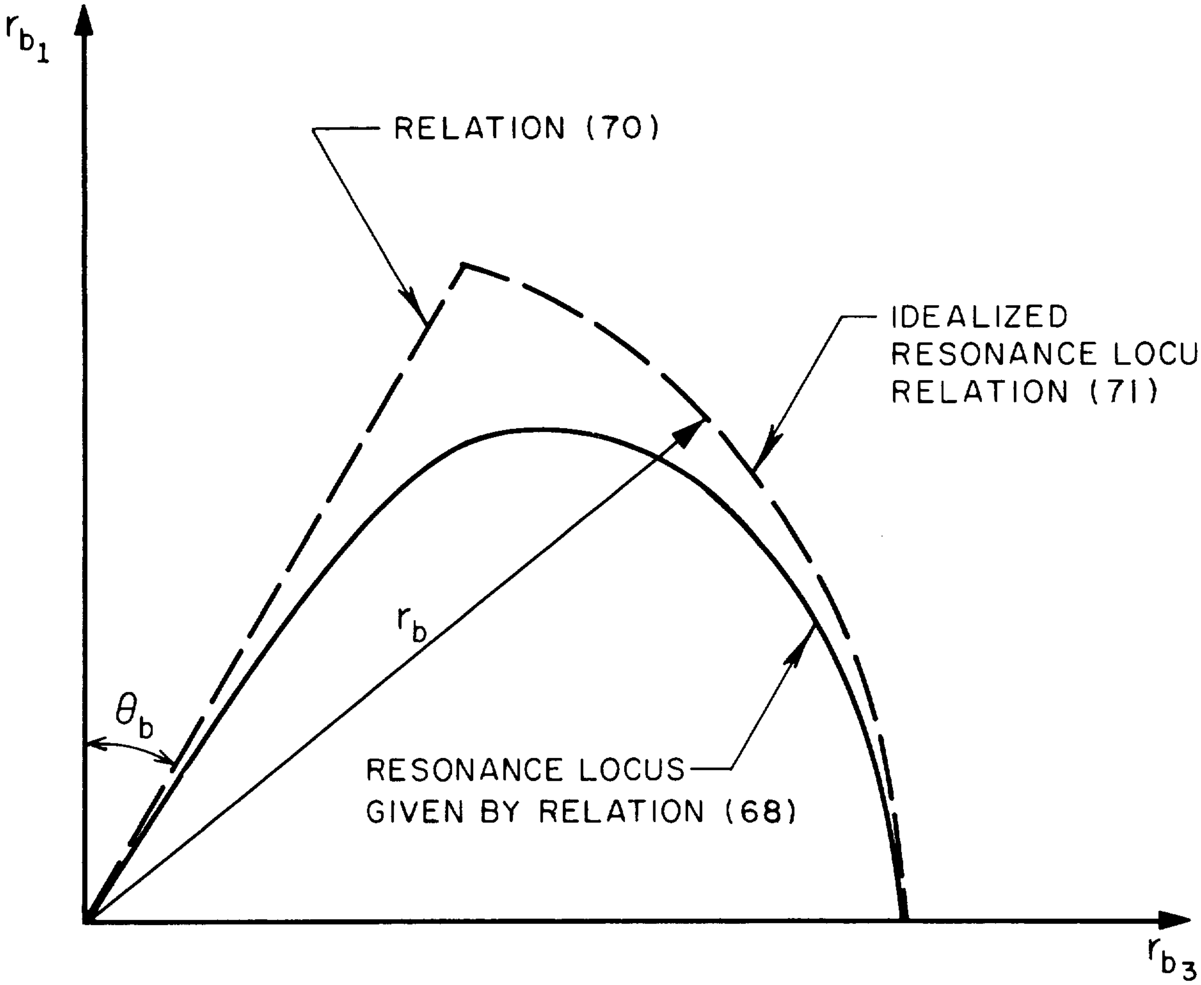

r_{b_1}
RELATION (70)
IDEALIZED RESONANCE LOCUS RELATION (71)
r_b
θ_b
RESONANCE LOCUS GIVEN BY RELATION (68)
r_{b_3}

FIG. 20 IDEALIZATION OF RESONANCE LOCUS FOR AN ORTHOTROPIC CYLINDER BELOW RING FREQUENCY

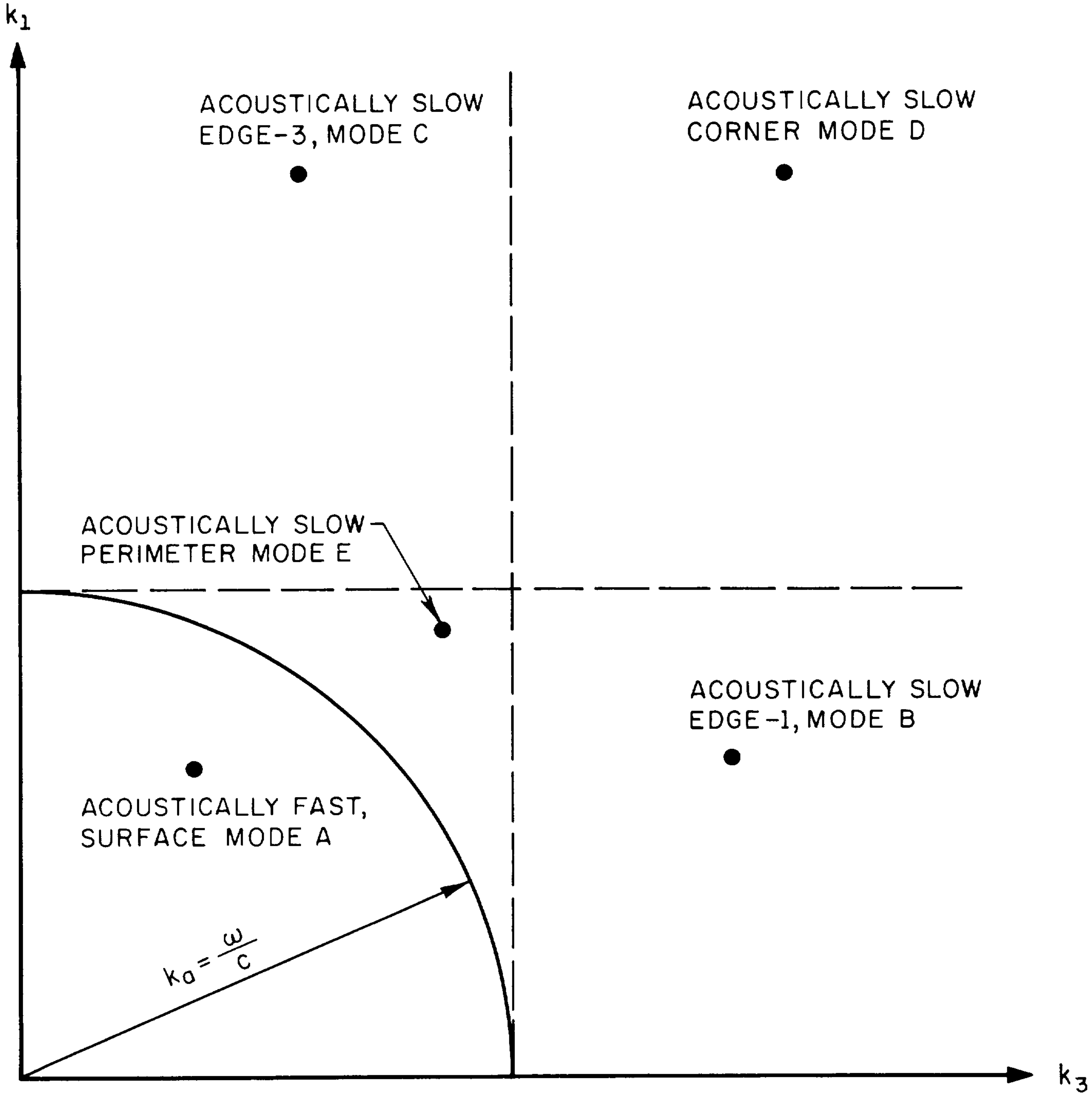
k_1
ACOUSTICALLY SLOW EDGE-3, MODE C
ACOUSTICALLY SLOW CORNER MODE D
ACOUSTICALLY SLOW PERIMETER MODE E
ACOUSTICALLY SLOW EDGE-1, MODE B
ACOUSTICALLY FAST, SURFACE MODE A
$k_a = \frac{\omega}{c}$
k_3

FIG. 21 CLASSIFICATION OF STRUCTURAL MODES IN k-SPACE AT FREQUENCY ω

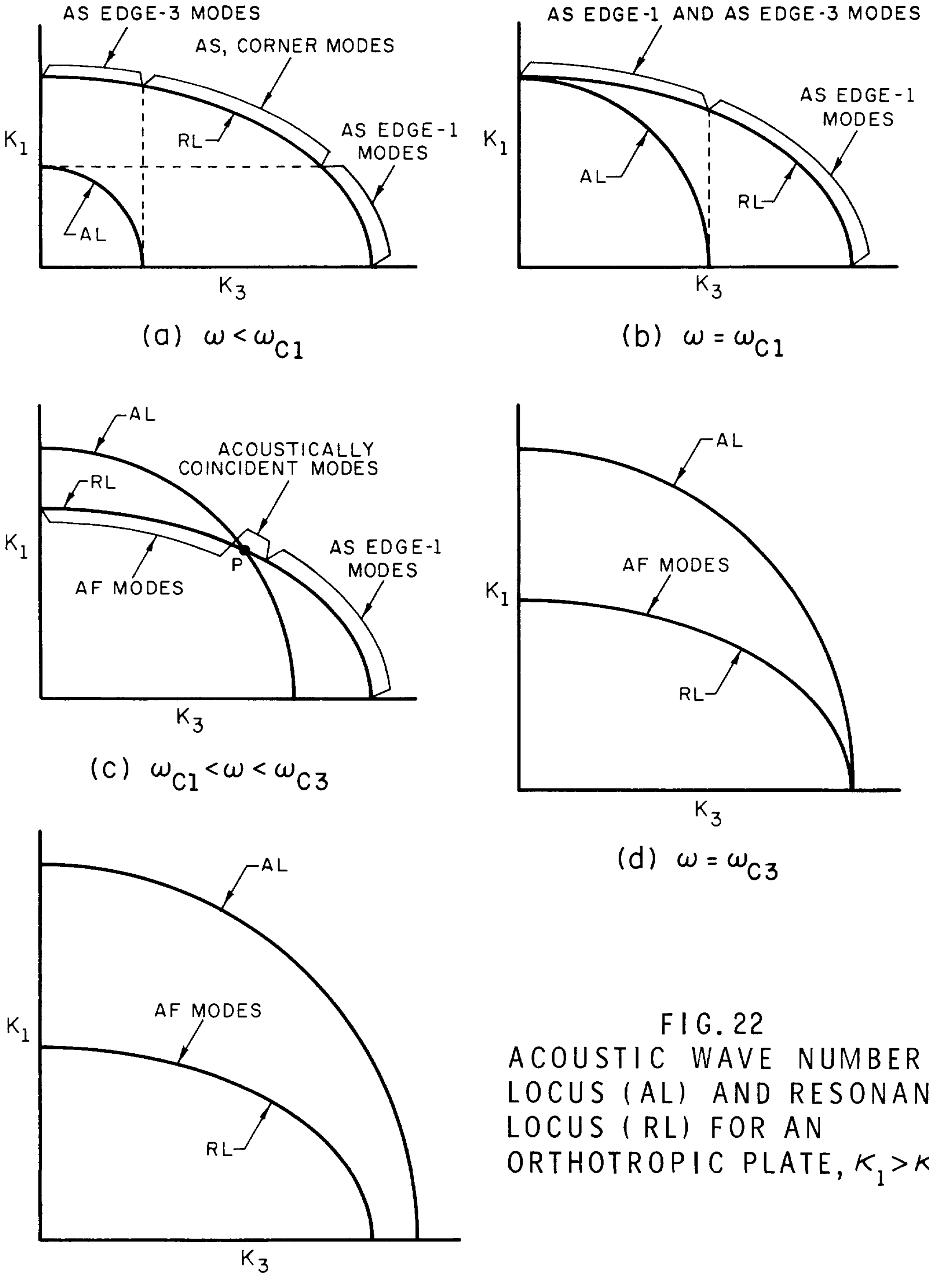
AS EDGE-3 MODES
AS, CORNER MODES
RL
AS EDGE-1 MODES
AL
K_1
K_3
AS EDGE-1 AND AS EDGE-3 MODES
AS EDGE-1 MODES
AL
RL
K_1
K_3
AL
RL
ACOUSTICALLY COINCIDENT MODES
AS EDGE-1 MODES
AF MODES
P
K_1
K_3
AL
AF MODES
RL
K_1
K_3
AL
AF MODES
RL
K_1
K_3

(a) $\omega < \omega_{C1}$

(b) $\omega = \omega_{C1}$

(c) $\omega_{C1} < \omega < \omega_{C3}$

(d) $\omega = \omega_{C3}$

(e) $\omega > \omega_{C3}$

FIG. 22
ACOUSTIC WAVE NUMBER LOCUS (AL) AND RESONANCE LOCUS (RL) FOR AN ORTHOTROPIC PLATE, $\kappa_1 > \kappa_3$

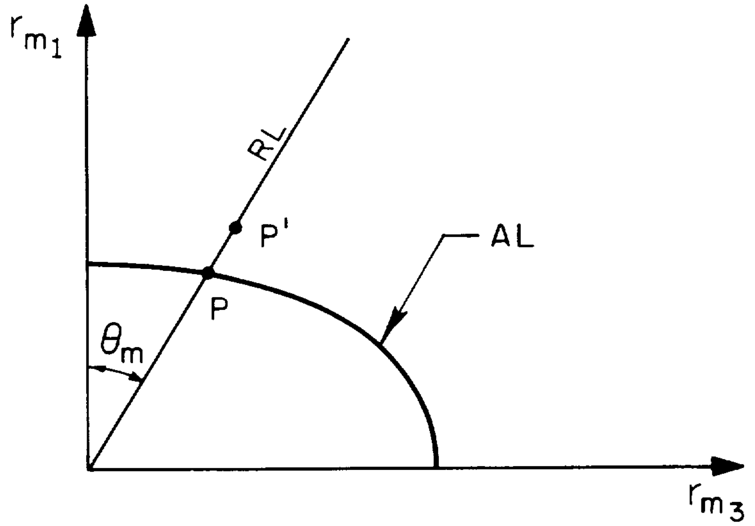
r_{m_1}
RL
P'
AL
P
θ_m
r_{m_3}

FIG. 23

(a) ACOUSTIC WAVE NUMBER LOCUS (AL) AND RESONANCE LOCUS (RL) FOR AN ORTHOTROPIC CYLINDER BELOW RING FREQUENCY, $\alpha_3 > \alpha_1$

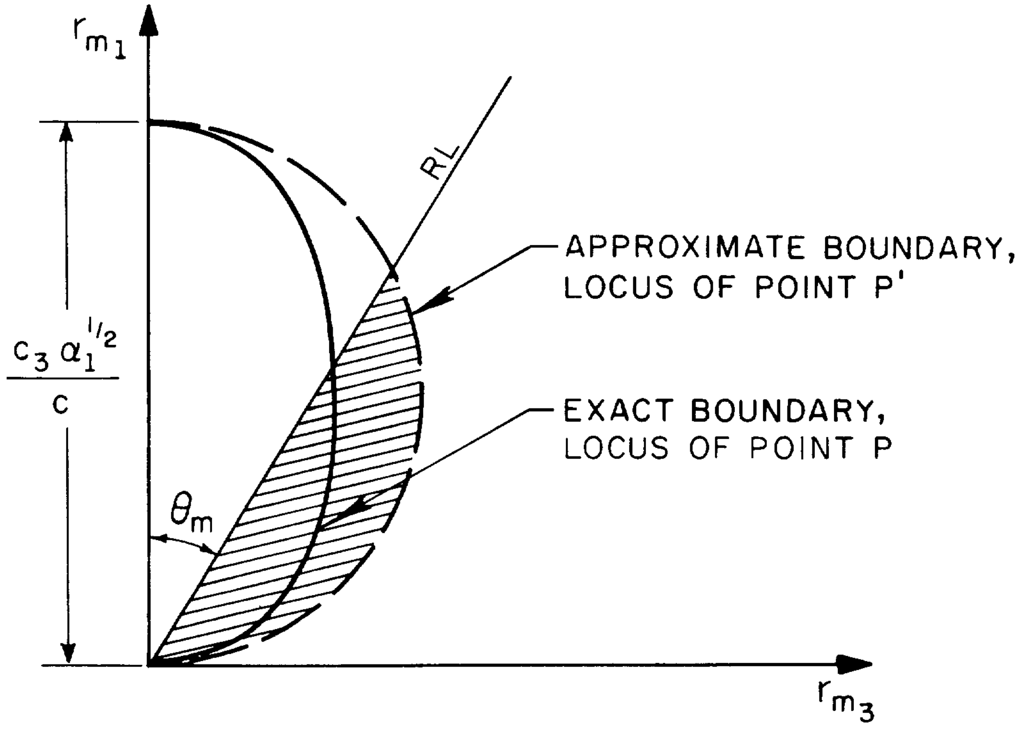
r_{m_1}
RL
APPROXIMATE BOUNDARY, LOCUS OF POINT P'
$\frac{c_3 \alpha_1^{1/2}}{c}$
EXACT BOUNDARY, LOCUS OF POINT P
θ_m
r_{m_3}

FIG. 23

(b) EXACT AND APPROXIMATE BOUNDARIES OF THE REGION OF THE AF MODES FOR AN ORTHOTROPIC CYLINDER

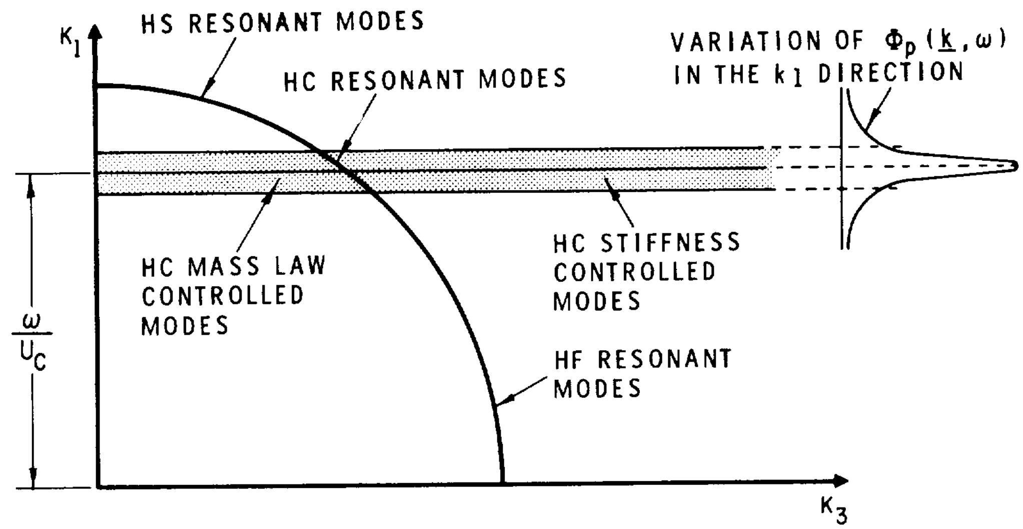
K_1
HS RESONANT MODES
HC RESONANT MODES
VARIATION OF $\Phi_p(\underline{k},\omega)$
IN THE k_1 DIRECTION
HC MASS LAW
CONTROLLED
MODES
HC STIFFNESS
CONTROLLED
MODES
$\frac{\omega}{U_C}$
HF RESONANT
MODES
K_3

(a) THE "BENDING REGION" OF THE WAVE NUMBER PLANE, $\omega_r < \omega < \omega_h$

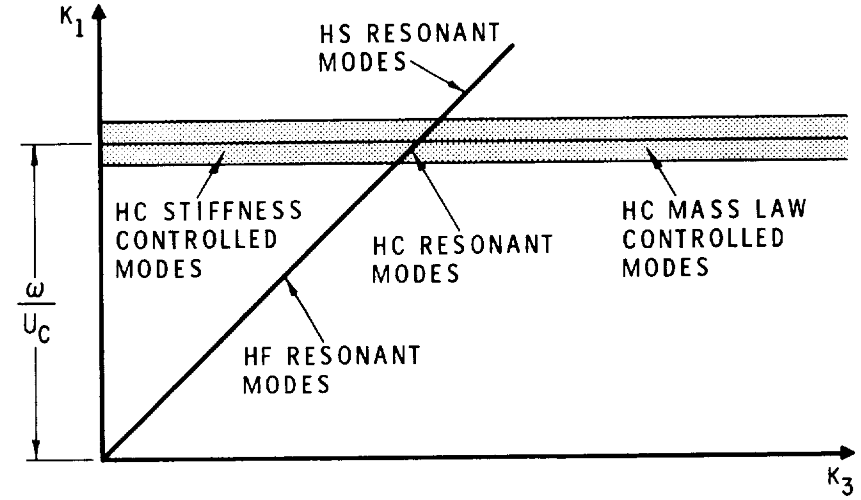
K_1
HS RESONANT
MODES
HC STIFFNESS
CONTROLLED
MODES
HC RESONANT
MODES
HC MASS LAW
CONTROLLED
MODES
$\frac{\omega}{U_C}$
HF RESONANT
MODES
K_3

(b) THE "MEMBRANE REGION" OF THE WAVE NUMBER PLANE, $\omega < \omega_r$

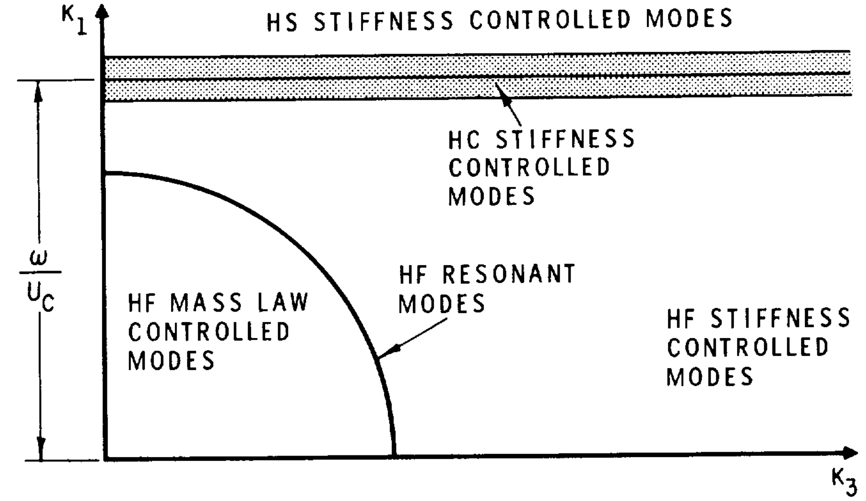
K_1
HS STIFFNESS CONTROLLED MODES
HC STIFFNESS
CONTROLLED
MODES
$\frac{\omega}{U_C}$
HF RESONANT
MODES
HF MASS LAW
CONTROLLED
MODES
HF STIFFNESS
CONTROLLED
MODES
K_3

(c) THE "BENDING REGION" OF THE NUMBER PLANE, $\omega > \omega_h$

FIG. 24 THE RANGE OF EXCITATION AND THE CLASSIFICATION OF MODES IN THE WAVE NUMBER PLANE. ISOTROPIC CYLINDER

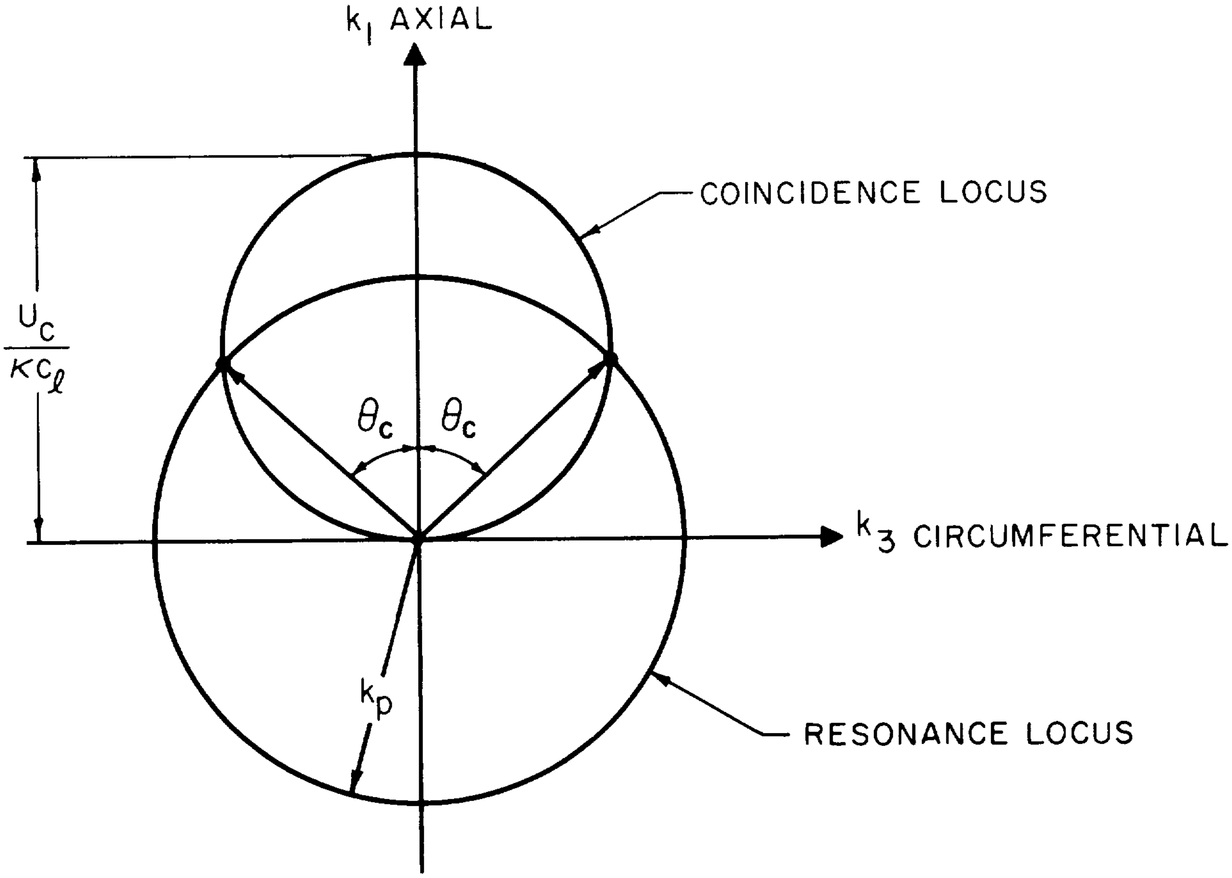
k_1 AXIAL
COINCIDENCE LOCUS
$\frac{U_c}{\kappa c_\ell}$
θ_c
θ_c
k_3 CIRCUMFERENTIAL
k_p
RESONANCE LOCUS

FIG. 25 LOCI OF RESONANCE AND HYDRODYNAMIC COINCIDENCE IN k PLANE

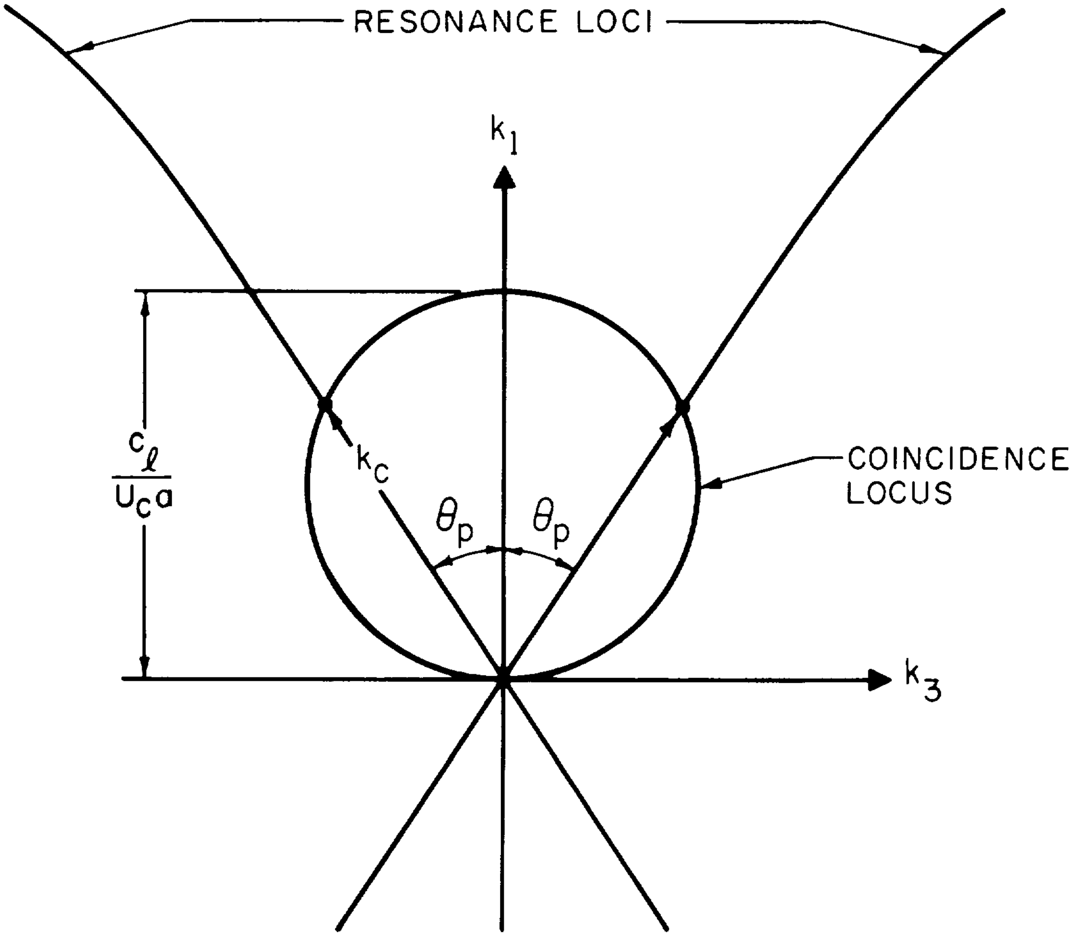
RESONANCE LOCI
k_1
$\frac{c_\ell}{U_c a}$
k_c
θ_p
θ_p
COINCIDENCE LOCUS
k_3

FIG.26 LOCI OF RESONANCE AND HYDRODYNAMIC COINCIDENCE IN k PLANE BELOW RING FREQUENCY

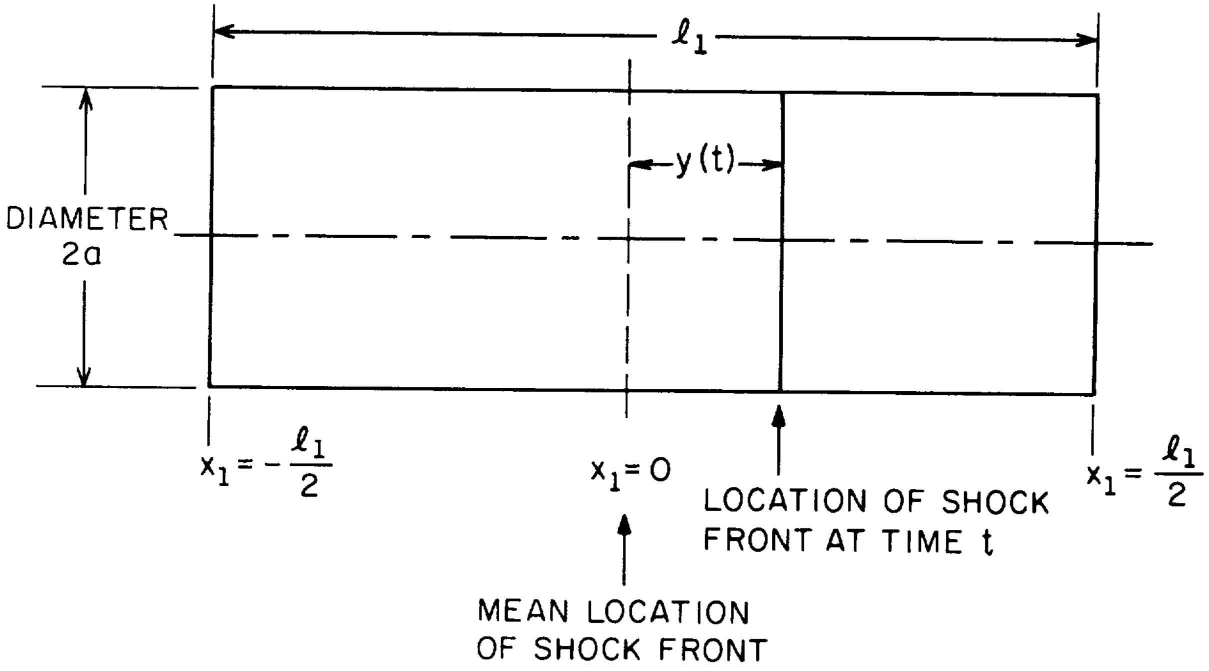
ℓ_1
DIAMETER 2a
y(t)
$x_1 = -\frac{\ell_1}{2}$
$x_1 = 0$
LOCATION OF SHOCK FRONT AT TIME t
$x_1 = \frac{\ell_1}{2}$
MEAN LOCATION OF SHOCK FRONT

(a) PROJECTED VIEW OF THE CYLINDER

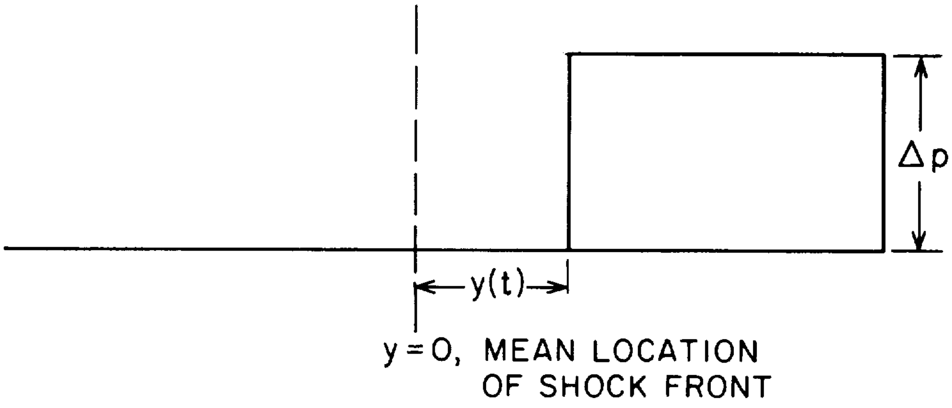
Δp
y(t)
y = 0, MEAN LOCATION OF SHOCK FRONT

(b) VARIATION OF PRESSURE P(x, t) IN THE AXIAL DIRECTION

FIG.27 SCHEMATIC REPRESENTATION OF A CYLINDER, AND VARIATION OF PRESSURE FIELD ASSOCIATED WITH AN OSCILLATING SHOCK

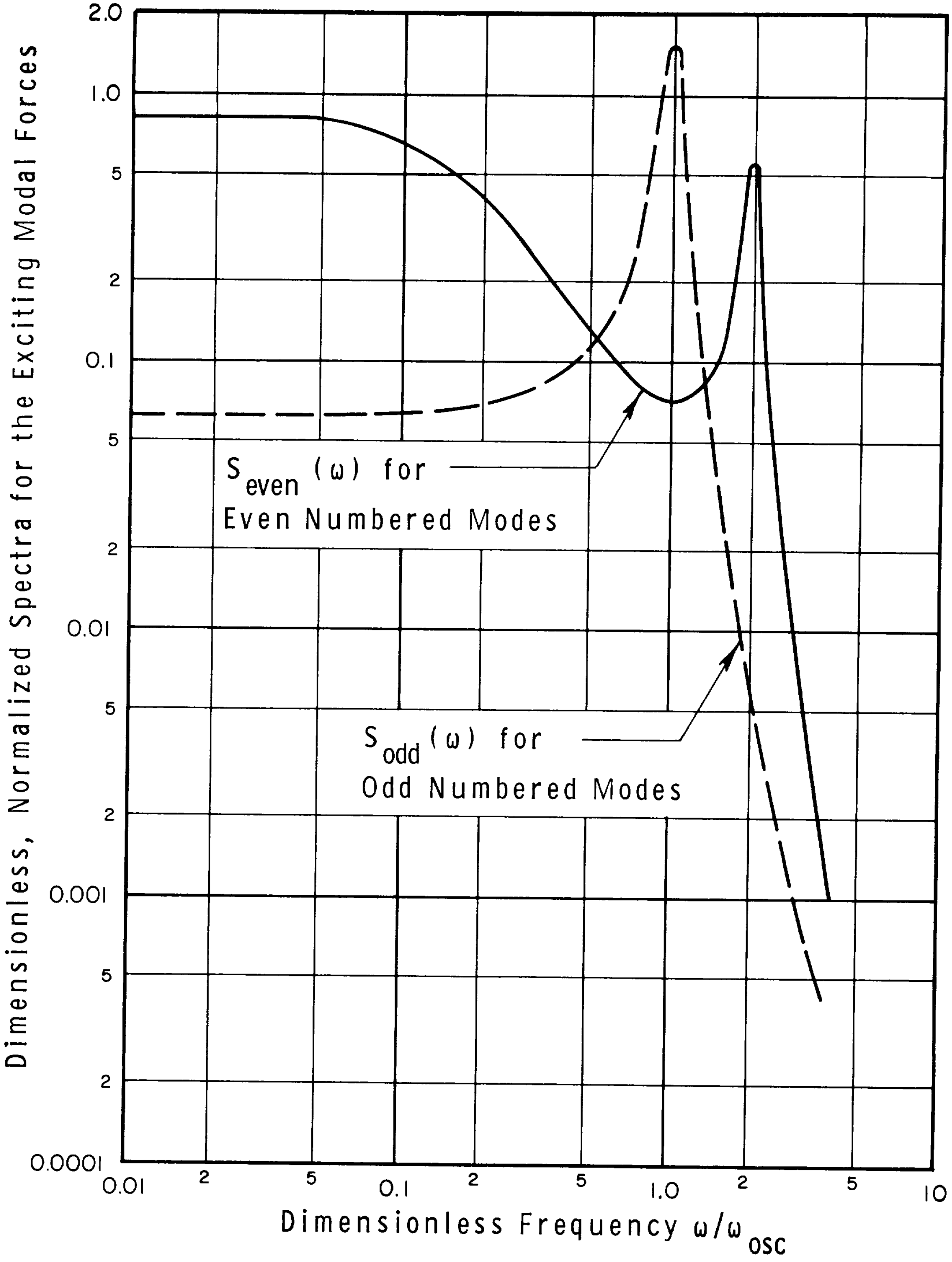

FIG. 28 DIMENSIONLESS SPECTRA FOR THE EXCITING MODAL FORCES. EXCITATION FROM AN OSCILLATING SHOCK